

INVESTIGATION OF GLACIAL DYNAMICS IN THE LAMBERT GLACIER-
AMERY ICE SHELF SYSTEM (LAS) USING REMOTE SENSING

A Dissertation

by

ZHAOHUI CHI

Submitted to the Office of Graduate Studies of
Texas A&M University
in partial fulfillment of the requirements for the degree of

DOCTOR OF PHILOSOPHY

Approved by:

Chair of Committee,	Andrew G. Klein
Committee Members,	Mahlon C. Kennicutt II
	Hongxing Liu
	Sorin C. Popescu
Head of Department,	Vatche P. Tchakerian

December 2012

Major Subject: Geography

Copyright 2012 Zhaohui Chi

ABSTRACT

Numerous recent studies have documented dynamic changes in the behaviors of large marine-terminating outlet glaciers and ice streams in Greenland, the Antarctic Peninsula, and West Antarctica. However, fewer observations of outlet glaciers and ice shelves exist for the East Antarctic Ice Sheet. In addition, most recent surface velocity mappings of the Lambert Glacier-Amery Ice Shelf system (LAS) are derived for the time period of 1997-2000. From this research, surface velocity measurements provide a more extended view of the behavior and stability of the LAS over the past two decades than can be gleaned from a single observational period.

This study uses remote sensing to investigate whether significant changes in velocities have occurred from the late 1980's through the late 2010's and assesses the magnitude of mass balance changes observed at the grounding line. To accomplish this goal, surface velocities of the LAS from late 1980's to late 2010's for three separate time periods are measured. The observed surface velocities of the LAS ranged from 0 to 1300 m yr⁻¹ during 1988-1990. A slight slowing down is detected in the central Amery Ice Shelf front by analyzing the surface velocity measurements made along the centerlines.

The mass balance is the difference between snow accumulation and the outflux of the grounded LAS and is calculated for individual sub-basin during the three time intervals of 1988-1990, 1999-2004, and 2007-2011 to illustrate the mass balance variation under sub-basin level. The flux gates of the Lambert Glacial sub-basin combined with the Mellor Glacial and the Fisher Glacial sub-basin appear to be the

largest outlet of the grounded ice of the LAS. The ice mass transported from the interior region through the three flux gates in total is 43.58 Gt yr^{-1} , 36.72 Gt yr^{-1} , and 38.61 Gt yr^{-1} respectively for the three time intervals above. The sub-basins in the eastern side appear differently than the western side. The outfluxes of the eastern sub-basins vary from 15.85 to 18.64 Gt yr^{-1} , while the western outfluxes vary from 15.85 to 18.64 Gt yr^{-1} .

The grounded LAS has discharged ice from 84.55 to 81.60 Gt yr^{-1} and to 79.20 Gt yr^{-1} during 1980s-1990s and 1990s-2000s. Assuming the snow accumulation distribution is stable, the grounded LAS mass loss has increased 2.95 Gt yr^{-1} from 1980s to 1990s and 2.40 Gt yr^{-1} from 1990s to 2000s. These results indicate insight into the stability of the Amery Ice Shelf over the last few decades.

DEDICATION

“With aged men is wisdom, and in length of days understanding.”

- Job 12:12

ACKNOWLEDGEMENTS

This research cannot be possible without helps from many people. I would like to acknowledge my committee members, Dr. Mahlon C. Kennicutt, Dr. Hongxing Liu, and Dr. Sorin C. Popescu for their guidance and supports throughout my research career journey at Texas A&M University as a graduate student. I would also like to express my sincere thanks to Dr. Anthony M. Filippi for substituting Dr. Hongxing Liu in my dissertation defense. I especially would like to thank the departmental faculty and staff for making my time at Texas A&M University and all my colleagues in the Cryosphere cluster group for their companionship and cheers.

My deepest gratitude goes toward my advisor, Dr. Andrew G. Klein, for his advices and supports. Without Dr. Klein's guide, this study could never have been completed. It was a great experience and my great honor to collaborate with him.

Furthermore, I would like to thank my friends who encourage me when I feel lost and disappointed over the years. I am blessed to know each and every of them.

Finally, I am deeply indebted to my family. I am grateful to my mother and father who through their encouragement and love to support me unconditionally. I also would like to thank my husband for his patience and acceptance while I was working on campus late. Thank you all. May the Lord bless you and keep you.

NOMENCLATURE

AADC	Australian Antarctic Data Center
AIS	Antarctic Ice Sheet
AISDS	Amery Ice Shelf Drainage System
AMM-1	Antarctic Mapping Mission
ANARE	Australian National Antarctic Research Expedition
ASAR	Advanced Synthetic Aperture Radar
ASF	Alaska Satellite Facility
CalTech	California Institute of Technology
CHINARE	Chinese National Arctic/Antarctic Research Expeditions
Cosi-corr	Co-registration of Optically Sensed Images and Correlation
DEM	Digital Elevation Model
D-InSAR	Differential Synthetic Aperture Radar Interferometry
Dome	A Dome Argus
ERS	Earth Remote Sensing Satellite
ESA	European Space Agency
ESRIN	European Space Research Institute
ETM+	Enhanced Thematic Mapper Plus
GIS	Geographic Information System
GPS	Global Positioning System
HJ	HuanJing (Environment)

ICESat	Ice, Cloud, and Land Elevation Satellite
IDL	Interactive Data Language
InSAR	Interferometric SAR
IPCC	Intergovernmental Panel on Climate Change
JPL	Jet Propulsion Laboratory
LAS	Lambert glacier-Amery ice shelf System
LGB	Lambert Glacier Basin
LGDB	Lambert Glacier Drainage Basin
LOS	Look-of-Sight
MAMM	Modified Antarctic Mapping Mission
MEaSURES	Making Earth Science Data Records for Use in Research Environments
MODIS	Moderate Resolution Imaging Spectrometer
NCC	Normalized Cross Correlation
NSIDC	National Snow and Ice Data Center
PCA	Principle Component Analysis
PDD	Positive Degree Day Model
PPP	Precise Point Position
RAMM	RADARSAT Antarctic Mapping Mission
RAMP	Radarsat Antarctic Mapping Project
ROI_PAC	Repeat Orbit Interferometry PACkage
SAR	Synthetic Aperture Radar
SLC	Single Look Complex

SLR	Sea Level Rise
SNR	Signal Noise Ratio
TM	Thematic Mapper
USGS	United States Geological Survey

TABLE OF CONTENTS

	Page
ABSTRACT	ii
DEDICATION	iiv
ACKNOWLEDGEMENTS	v
NOMENCLATURE	vi
TABLE OF CONTENTS	iix
LIST OF FIGURES	xi
LIST OF TABLES	xvi
CHAPTER I INTRODUCTION	1
1.1 Background	1
1.2 Lambert Glacier-Amery Ice Shelf System	7
1.3 Importance of the Study under Broader Scientific Frame	9
1.4 Research Objectives	10
1.5 Study Approach	12
1.6 Structure of the Research and Dissertation	14
CHAPTER II SURFACE VELOCITY DERIVATION OF THE LAS USING FEATURE TRACKING, OFFSET TRACKING, AND INSAR FROM MULTIPLE SATELLITE DATA	15
2.1 Overview	15
2.2 Introduction	16
2.3 Surface Velocity Retrieval	23
2.3.1 Surface Motion Retrieval by Optical Feature Tracking	24
2.3.2 Surface Motion Retrieval by SAR Feature Tracking	41
2.3.3 Surface Motion Retrieval by Offset Tracking	47
2.3.4 Surface Motion Retrieval by SAR Interferometry (InSAR)	52
2.4 Discussion	61
CHAPTER III SURFACE VELOCITY VARIATIONS ANALYSIS OF THE LAMBERT GLACIER-AMERY ICE SHELF SYSTEM (LAS)	65

3.1 Background	65
3.2 Data Acquisition.....	68
3.3 Surface Velocity Mappings	72
3.3.1 Surface Velocity Observations (1988-1990)	72
3.3.2 Surface Velocity Observations (1999-2004)	74
3.3.3 Surface Velocity Observations (2007-2011)	76
3.3.4 Combined Surface Velocity Observations of Three Time Intervals	77
3.4 Comparisons of Feature Tracking and the Published Velocities	79
3.4.1 Comparison of Feature Tracking and the RAMP InSAR Velocities	79
3.4.2 Comparison of Feature Tracking and the Field Measurements.....	84
3.5 Advanced Analyses	88
3.5.1 Congruency Test.....	89
3.5.2 Delineation of Fast-moving Areas, Flowlines, and Imaginary Flux gates	90
3.5.3 Variation Analysis of Surface Velocity.....	96
3.5.4 Motion Analysis of the Amery Ice Shelf Front	106
3.6 Discussions.....	111
 CHAPTER IV ESTIMATES OF MASS BALANCE OF THE LAMBERT GLACIER-AMERY ICE SHELF SYSTEM (LAS)	 115
4.1 Mass Balance of the LAS.....	115
4.2 Concept of Balance Velocity.....	121
4.3 Methods	123
4.4 Data Acquisition.....	127
4.5 Computation Outcomes.....	134
4.5.1 Estimates of Ice Discharge through Flux Gates	134
4.5.2 Mass Balance and Its Variation Computation	136
4.6 Discussions.....	138
 CHAPTER V CONCLUSIONS.....	 141
5.1 Conclusions	141
5.2 Summary of Findings	142
5.3 Future Work	143
 REFERENCES	 145

LIST OF FIGURES

	Page
Figure 1.1 The Lambert Glacier-Amery Ice Shelf System, LAS overlaid on a Radarsat-1 mosaic of Antarctica. The light blue dashed line represents the southern boundary of the LAS. The cyan dashed line is the grounding line of the Amery Ice Shelf. The brown solid line represents the boundary of sub-basins feeding into the LAS.	8
Figure 1.2 Timeline of existing velocity observations over the LAS as well as the study periods for this research.....	11
Figure 2.1 A sketch map of feature tracking (Huang and Li, 2009, p.575).....	25
Figure 2.2 Examples of SLC off-correction of ETM+ images using Frame and Fill software.....	29
Figure 2.3 Partial color-coded point velocities of the LAS determined from cross correlation of ETM+ image pair of 2011/11/14 and 2002/12/19 in the confluence zone of the Mellor, Fisher, and Lambert glaciers. The inset map shows the location of the velocity study	30
Figure 2.4 Predicted magnitudes of velocities obtained from the analysis of the velocity fields illustrated in Fig 3 (units m yr ⁻¹) using ordinary Kriging.....	31
Figure 2.5 Histograms of five datasets used for congruency tests. The inset map shows the location of the five datasets	32
Figure 2.6 (a) Color-coded point velocities of the LAS determined from cross correlation of a TM image pair consisting of images acquired on 1988/03/06 and 1989/03/18; (b) Color-coded point velocities from cross correlation of an ETM+ image pair consisting of images acquired on 2001/11/14 and 2002/12/19 for the similar region as Figure 2.6(a)	34
Figure 2.7 (a-d) Surface velocity profiles for the Fisher Glacier, Mellor Glacier, Lambert Glacier, and Amery Ice Shelf; (e) Comparisons between feature tracking and InSAR measurements along four velocity profiles.....	38

Figure 2.8	(a) Preprocessed ENVISAT ASAR pair for SAR feature tracking; (b) Color-coded SAR feature tracking-derived surface velocity fields	44
Figure 2.9	Comparisons between SAR feature tracking and InSAR measurements (MEaSURES project) along one individual velocity profile.	46
Figure 2.10	9-look Intensity ENVISAT ASAR images of (a) 2009/08/08 and (b) 2010/07/24 for offset tracking based on radar geometry.....	50
Figure 2.11	Offset fields under Radar geometry in (a) slant-range and (b) azimuth direction; the intensity of the displacement is shown in (c).	51
Figure 2.12	Error analysis for the offset tracking method using sixteen measurements.	52
Figure 2.13	Schematic map of the geometry for the measurement of ice surface velocity from InSAR (Kwok and Fahnestock, 1996).....	55
Figure 2.14	(a) Intensity image; (b) Wrapped Interferogram derived from the ERS-1/2 InSAR pair. The topographic contribution to the phase has been removed using topography generated by the RAMP DEM; (c) Coherence image. (d) Slant-range component displacement; (e) Azimuth component displacement; (f) Horizontal displacement map; (g) Geocoded velocity map	59
Figure 3.1	Surface velocity map (1988-1990) interpolated with the velocity fields derived by this study using the Ordinary Kriging method. The map is overlaid with Radarsat-1 image mosaic.....	74
Figure 3.2	Surface velocity map (1999-2003) determined using feature tracking and interpolated with the derived velocity fields using the Ordinary Kriging method. The map is overlaid with the Radarsat-1 image mosaic.....	75
Figure 3.3	Surface velocity map (2007-2011) determined using feature tracking and interpolated with the derived velocity fields using the Ordinary Kriging method. The map is overlaid with Radarsat-1 image mosaic .	77
Figure 3.4	Surface velocity map of (a) 1988-1990, (b) 1999-2004, and (c) 2007-2011 for the LAS. All maps are overlaid over the Radarsat-1 image mosaic. The thick black solid line separates Landsat- and MODIS-derived surface velocities. The hatched areas indicate the missing Landsat/MODIS observations.	78

Figure 3.5	(a) Surface velocity map (1997-2000) created by RAMP using InSAR; (b) Magnitude of velocity difference between InSAR measurements and this study; (c) Velocity difference in percentage between InSAR measurements and this study. The maps are overlaid with Radarsat-1 image mosaic. The purple dashed line is a boundary separating Landsat- and MODIS- derived surface velocity measurements. White color represents the missing InSAR measurements. The inset map shows location of the LAS in Antarctica.	81
Figure 3.6	Frequency distribution of (a) absolute velocity differences and (b) percentage velocity differences between RAMP InSAR measurements and feature tracking with Landsat and MODIS.....	84
Figure 3.7	(a) The feature tracking derived velocity measurements (solid light gray triangle) during 1988-1990 within 2 km of the GPS velocity fields (solid black dots); (b) The absolute differences in m yr ⁻¹ and percentage differences for all the GPS velocity fields collected during 1990-1991; (c) Plot of surface velocity magnitude and absolute differences and percentage differences for the time period of 1988-1990; (d) The feature tracking-derived velocity measurements (solid light gray triangle) during 1999-2004 within 2 km of the GPS velocity fields (solid black dot); (e) The absolute differences in m yr ⁻¹ and percentage differences for all the GPS velocity fields collected in 1999; (f) Plot of surface velocity magnitude and absolute differences and percentage differences for the time period of 1999-2004.....	86
Figure 3.8	The comparisons between the Landsat-derived velocity magnitude and direction and the closest MODIS-derived velocity measurements per 100m within a 1 km radius.....	90
Figure 3.9	(a) Fast-moving areas and (b) highest velocities of the three major glaciers derived by feature tracking for the time intervals of 1988-1990, 1999-2004, and 2009-2011 and derived by InSAR for the time interval of 1997-2000 (RAMP)	92
Figure 3.10	Flow contour features of 1988-1990 for the Lambert Glacier, the Mellor Glacier, the Fisher Glacier, the West Tributary Glacier, the Charybdis Glacier, and the East Tributary Glacier	94
Figure 3.11	Flow contour features of 1999-2004 for the Lambert Glacier, the Mellor Glacier, the Fisher Glacier, the West Tributary Glacier, and the Charybdis Glacier	95

Figure 3.12	Flow contour features of 2007-2011 for the Lambert Glacier, the Mellor Glacier, the Fisher Glacier, the West Tributary Glacier, the East Tributary Glacier, and the Charybdis Glacier	96
Figure 3.13	Location of the centerlines for the Amery Ice Shelf (Black), the Lambert Glacier (Blue), the Mellor Glacier (Green), and the Fisher Glacier (Red)	97
Figure 3.14	Surface velocity profiles for the Amery Ice Shelf in 1988-1990, 1999-2004, and 2007-2011	98
Figure 3.15	Surface velocity profiles for the Lambert Glacier for 1988-1990, 1999-2004, and 2007-2011	99
Figure 3.16	Surface velocity profiles for the Mellor Glacier between 1988-1990, 1999-2004, and 2007-2011	100
Figure 3.17	Surface velocity profiles for the Fisher Glacier during 1988-1990, 1999-2004, and 2007-2011	102
Figure 3.18	Surface velocity profiles of the Amery Ice Shelf, and three major glaciers in 1988-1990, 1999-2004, and 2007-2011	104
Figure 3.19	Surface velocity variations extracted from the four surface velocity profiles between two time intervals of 99/04-88/90 and 07/11-99/04. The dashed line and solid line represent the linear regression trend for 99/04-88/90 and 07/11-99/04 respectively	105
Figure 3.20	The Amery Ice Shelf front positions for seven time intervals from 1988 to 2012. Y axis presents the motion estimation in unit of meter per year	108
Figure 3.21	(a) The geographic locations of the upstream ends of rift A (solid dark blue dots) and rift B (solid dark green dots) as well as the eastern ends of the transverse-to-flow fracture of Rift A (solid light green); (b) The distances between the upstream ends of rift A and rift B and the ice shelf front for the five time periods during 1988-2012. The Y axis is the distance in km; (c) The plot of distances between the eastern end of the transverse-to-flow fracture of Rift A and the upstream end of Rift B with a dashed trend line	110
Figure 4.1	Mass balance velocity field from the Byrd Research Center, Ohio State University (Wu & Jezek, 2004)	116

Figure 4.2	A schematic diagram illustrating dependence of \bar{u} on b_n on an ice sheet (modified based on Figure 5.1, Roger Hooke, 2005).....	121
Figure 4.3	(a) Schematic diagram of flux mass for an individual location along a flux gate; (b) schematic diagram of flux mass for an imaginary flux gate	125
Figure 4.4	(a) Original ice thickness of the LAS region received from the SCAR BEDMAP project; (b) preprocessed ice thickness data by this study..	128
Figure 4.5	(a) Average annual snowfall accumulation map during 1955-2004 (Monaghan et al., 2006); (b) annual snowfall accumulation map (Arthern et al., 2006). The black dots represent the accumulation measurements	130
Figure 4.6	(a) Locations of imaginary flux gate (black solid lines) overlaid on a Radarsat-1 mosaic of Antarctica; (b) zoom to flux gates 1-13; (c) zoom to flux gates 14-40; (d) zoom to flux gates 41-58. The light blue represents the most recently derived grounding line of the Amery Ice Shelf (based on Bindshadler et al., 2011)	133

LIST OF TABLES

	Page
Table 2.1 Summary of previous surface velocity measurements observed in the LAS region.....	18
Table 2.2 Summary of pros and cons of five surface velocity derivation methods.....	21
Table 2.3 List of Landsat data acquired for feature tracking.....	28
Table 2.4 Congruency test on the five datasets.	33
Table 2.5a Magnitudes of velocity vectors over ice-free regions used for error analysis	36
Table 2.5b Magnitudes of velocity vectors over fast-moving regions used for error analysis.....	37
Table 2.6 Acquisition parameters for the image analyzed.....	43
Table 2.7 Two ERS-1/2 tandem SAR SLC images suitable for interferometric processing	58
Table 3.1 Summary of acquired satellite datasets.....	69
Table 3.2 Forty-seven GPS velocity measurements made in the Amery Ice Shelf during 1990-1999 (King, 2002).	70
Table 3.3 Comparison of the spatial extents of the fast-moving areas of the three major glacial basins between this study and the RAMP measurements.	93
Table 4.1 Summary of previous estimation of net mass balance and SLR contribution of the LAS.....	120
Table 4.2 Summary of snowfall accumulation data (Accu. is the abbreviation of accumulation).	131
Table 4.3 Summary of ice discharge fluxes for the sub-basins during three time periods of 1988-1990, 1999-2004, and 2007-2011 in Gt yr ⁻¹	135

Table 4.4	Summary of mass balance of the LAS grounded ice surface during the three time intervals of 1988-1990, 1999-2004, and 2007-2011. ...	137
-----------	---	-----

CHAPTER I

INTRODUCTION

1.1 Background

The Antarctic Ice Sheet (AIS) plays a critical role in Earth's climate system due to its contribution to oceanic and atmospheric circulation. The AIS covers a total area of $\sim 12.4 \times 10^6 \text{ km}^2$, averaging $\sim 2.4 \text{ km}$ in thickness with a volume of $\sim 25.7 \times 10^6 \text{ km}^3$ (Houghton *et al.*, 2001). More than 90% of the Earth's surface ice and 70% of freshwater is stored in the AIS (Meier, 1993). Its dynamics and mass balance are intricately linked to changes in global climate and sea level (Shepherd & Wingham, 2007). Of particular importance is the possibility of a significant rise in global sea level brought on by a change in the mass balance of the AIS under the influence of global warming (Alley *et al.*, 2005). Outlet glaciers and ice streams transport ice from the interior AIS towards its coastal margins and discharge ice into the surrounding oceans. The vast majority of mass loss from the AIS flows through a relatively small number of outlet glaciers and ice streams (Bamber *et al.*, 2000). To determine whether the AIS is growing has been a longstanding unsolved scientific problem. The AIS's contribution to sea level rise was $0.135 \pm 0.415 \text{ mm yr}^{-1}$ during the 1961 to 2003 period, while $0.205 \pm 0.345 \text{ mm yr}^{-1}$ from 1993 to 2003, reported by the Intergovernmental Panel on Climate Change Report (IPCC, 2007). Later, a large amount of research have been compiled and indicate the AIS mass balance lies between approximately +50 to -250 Gt yr^{-1} for 1992 to 2009 (Zwally & Giovinetto, 2011). Recent studies found there are

increased mass losses for some Antarctic outlet glaciers resulting from increased flow speed but independent of changes in surface accumulation rates (Thomas *et al.*, 2004; Payne *et al.*, 2004; Shepherd *et al.*, 2004). Hence, ice discharge in Antarctica might be expected to be more dynamic than it was considered and is likely to contribute to sea-level rise over decades (Solomon *et al.*, 2007).

One of the vital controls controlling the ice discharge rate and mass balance state of the AIS are the velocity fields of outlet glaciers and ice streams (Howat *et al.*, 2007; Rignot & Thomas, 2002). Accelerated or decreasing surface motion indicate an alteration in the state of mass balance, hence monitoring of glacier surface velocities is of importance to climate change studies (Strozzi *et al.*, 2007). If ice velocities increase, outlet glaciers and ice streams will deliver more ice to the ocean, which increasing the outward ice flux and reducing the ice volume stored in the AIS. An understanding of the long-term dynamic behavior of these outlet glaciers and ice streams is therefore critical for estimating the mass balance of the AIS.

Ice shelves are the floating extensions of a grounded glacier over the ocean (Thomas, 1979). They are the source of new icebergs. Ice shelves and glaciers are viewed as sensitive indicators and modulators for long-term global climate variability and change (Payne & Bamber, 2004). As the continent's fourth largest drainage system in Antarctica (Giovinetto, 1964; McIntyre, 1985), the Lambert Glacier-Amery Ice Shelf System (LAS) drains approximately 12.5% of the entire AIS (Drewry, 1983), second only to the Byrd Glacier (McIntyre, 1985). Due to its large size and dynamic nature, the LAS plays a fundamental role in the study of mass budget of the AIS in response to

present and future climate changes. Zwally *et al.* (2005) estimated the LAS's contribution to sea level rise ranging from $+2 \times 10^{-4}$ to $+5 \times 10^{-4}$ mm yr⁻¹. Quantifying the changes of such a highly dynamic glacier-ice shelf system is a fundamental in developing an understanding of the AIS's response to future climate change (Fink *et al.*, 2006). Furthermore, any significant variation of the LAS mass balance directly influences the estimate of the AIS mass balance and thus impacts global sea level.

Globally observed mass losses include increased ice discharge, due to enhanced ice velocity (Rignot *et al.*, 2003). An accurate assessment of this balance is severely challenged because of the vastness of the AIS and *in situ* measurements are sparse. Insufficient knowledge of the ice flow changes contributes to the complexity of achieving the task (IPCC, 2007). Even with the advent of Global Positioning System (GPS), making *in situ* measurements remains an expensive, and sometimes dangerous, task that yields a limited number of measurements over isolated sites. Meanwhile, Antarctica's remote location and its physical surrounding limits access to the study area to carry out the *in situ* measurements.

Despite these difficulties, there has been considerable pioneering research carried out on estimating the mass balance status of the LAS. The traditional velocity measurements of the LAS during 1960s to 1980s were mainly made by measuring and resurveying the established ice-movement stations (Budd, 1966; Allison, 1979; Budd *et al.*, 1982). Allison (1979) estimated a mass budget of the Lambert Glacier Drainage Basin (LGDB) of $+42 \pm 47$ Gt yr⁻¹ using those field survey data acquired during 1968-1974 and ice thickness data (Morgan & Budd, 1975). Budd and McInnes (1979) applied

a model that suggested a high potential for surging of the AIS. Due to insufficient knowledge of ice thickness and snow accumulation rates and surface velocities that were mainly confined to the transverse routes, previous analysis and estimates have been seriously limited and have varied widely. Recent work indicates that those historic surface velocity measurements are erroneous and yield velocity residual errors of up to 150 m yr^{-1} (King *et al.*, 2007).

Satellite remote sensing, which is well-suited for studies in remote areas, has made it attainable to derive surface velocity fields without the expense of *in situ* measurements. It provides a more convenient and comprehensive way to map ice surface morphological features and systematically monitor ice dynamic changes over time, compared with the conventional methods (Bindshadler *et al.*, 2001). Hence, remote sensing aids estimating the mass balance and identifying surface characteristics for glaciological studies. The studies in Antarctica particularly benefit from Antarctic Synthetic Aperture Radar (SAR) image mapping projects and another extensive Landsat acquisition program. With the advent of Synthetic Aperture Radar Interferometry (InSAR), several SAR image processing methods have been employed to increase the estimation accuracy and a positive mass balance has been concluded for the LAS (e.g. Rignot, 2002; Zwally *et al.*, 2005; Yu, 2005; Yu *et al.*, 2010). High-quality topographic data (such as satellite-radar altimeters) has also been utilized to compute the spatial distribution of the theoretical ice flux (Budd & Warner, 1996). However, the contributions to sea level rise from the LAS are estimated to vary widely (e.g., Zwally *et*

al., 2005) due to the large uncertainty remaining in the overall mass balance estimations (Allison, 1979; Rignot *et al.*, 2008; Yu *et al.*, 2010).

Long-term accurate velocity measurements are fundamental to refining the uncertainties remaining in the estimates of mass balance of the LAS. Most previous surface velocity estimates were studied either by expensive field survey measurements or using Earth Remote Sensing (ERS)-1/2 and Radarsat-1 SAR images. Field survey techniques, including GPS, are still used today, but remain logistically difficult and time-consuming. In recent decades, remote sensing technology has significantly enhanced our ability to observe and measure surface velocities over vast areas with high spatial resolutions, and has provided the comprehensive observations needed for modern scientific investigations of ice dynamics and mass balance.

To better understand the unexpected variations in ice surface velocities and the stability of the LAS, the dynamics of the entire system shall be considered and a long history of observations should be made. Long-term accurate velocity changes over the LAS are an important indicator not only to estimate mass balance change (Bindshadler *et al.*, 1993; Fricker *et al.*, 2000), but also to provide evidences for the stability of the Amery Ice Shelf (King *et al.*, 2009). King *et al.* (2007) have utilized the velocity values derived from *in situ* measurements to detect a small velocity slowdown ($\sim 0.6\%$) in the LAS. Most recent surface velocity field of the LAS (e.g., Rignot *et al.*, 2011b) have been compiled from multi-source satellite SAR imagery during the time period 2007-2009 using InSAR technique.

Consequently, satellite images can be a useful data source for long-term monitoring of the LAS. Beginning in mid-1990s and continuing through the present, remote sensing techniques have been used to carry out surface velocity observations on the LAS. Imaging radars (e.g. Radarsat and ERS Satellites) are more suitable than optical satellites to research on the glaciers due to their all-weather capabilities. Changes of a surface topography based on interferometric analysis of coherent SAR image pairs were conducted (Goldstein *et al.*, 1993; Rosen *et al.*, 2000; Joughin, 2002; Young & Hyland, 2002; Yu, 2005; Tang, 2007). However, accurate velocity measurements via traditional InSAR are limited by multiple factors such as the coherence of SAR image pairs as well as temporal and perpendicular baselines in certain ranges.

Feature tracking is another widely used image-based technique which tracks the motion of distinctive surface features moving with the ice and persistent in image pairs acquired by space-borne optical instruments over time (e.g., Gray *et al.*, 1998; Berthier *et al.*, 2003). Even so, surface features are not visible via optical images during the polar night and they are also limited by frequent cloud cover. The quality and distribution of surface features suitable for tracking significantly impacts the distribution and density of velocity observations derived from the feature tracking method. Similar to feature tracking, offset tracking is SAR image-based method which can compute sub-pixel offsets in the spatial domain using a cross-correlation algorithm (Strozzi *et al.*, 2002; Werner *et al.*, 2005; Strozzi *et al.*, 2007). The offset tracking method is particularly useful when traditional InSAR and feature tracking are limited by the problems, such as decorrelation.

1.2 Lambert Glacier-Amery Ice Shelf System

The LAS (Figure 1.1) is geographically located in East Antarctica and spanning approximately 68.5°S to 81°S latitude and 40°E to 95°E longitude (Fricker *et al.*, 2000). It occupies a large embayment northward of Prydz Bay. Allison (1979) was the first to call the area of ice streams converging into the Amery Ice Shelf the ‘Lambert Glacier System’. The total area of the LAS is $1.55 \times 10^6 \text{ km}^2$, most of which is composited by the floating ice of the Amery Ice Shelf (Fricker *et al.*, 2002a). Mass discharge of the system is mainly through this wide and freely floating ice (Philips, 1999).

Lambert Glacier channels the ice flows into the Amery Ice Shelf through the rift between the Prince Charles Mountains and the Mawson Escarpment (Hambrey, 1991; Yu, 2005) along with its major tributaries, Mellor and Fisher Glaciers. Along with these three flowlines, other tributary ice streams feed the ice shelf, most notably the Charybdis Glacier from the west and the Mawson Escarpment ice stream from the east (Yu, 2005). The LAS buttresses the Lambert Glacier Basin and is confined on three sides by a series of sub-basins which include the West Down Stream Glacial Basin, the Charybdis Glacial Basin, the West Tributary Glacial Basin, the Fisher Glacial Basin, the Mellor Glacial Basin, the Lambert Glacial Basin, the East Tributary Glacial Basin, and the East Down Stream Glacial Basin. The protection provided by these sub-basins may minimize destructive interactions with the ocean (King, 2002).

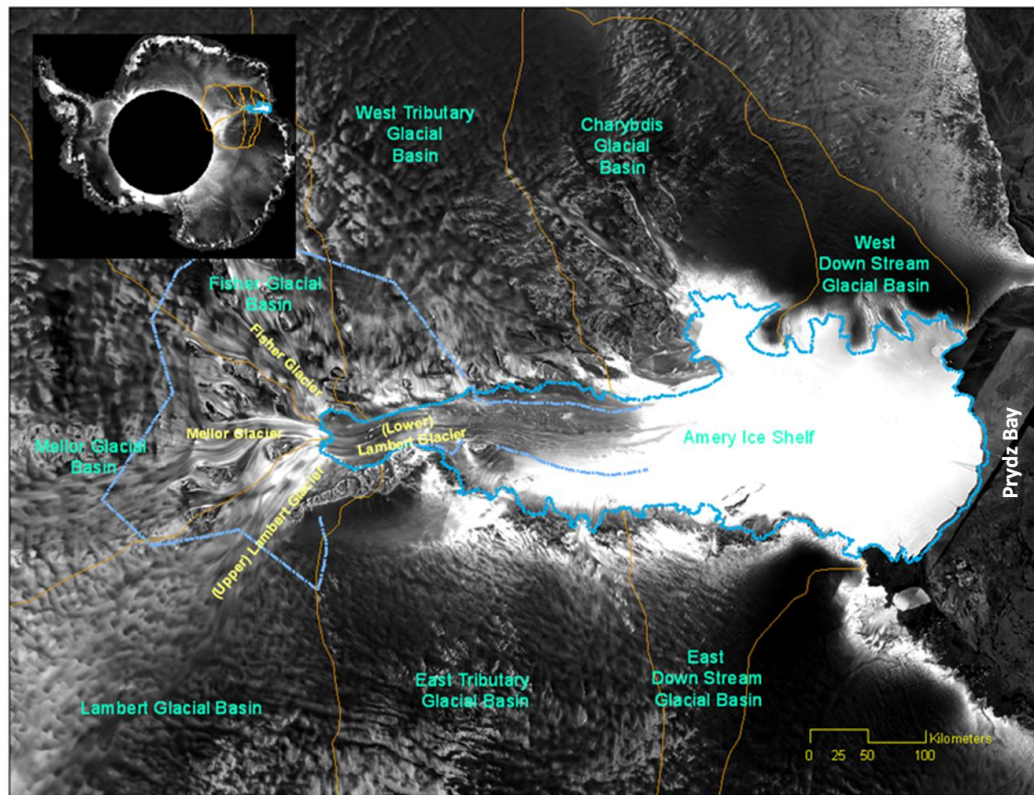


Figure 1.1 The Lambert Glacier-Amery Ice Shelf System, LAS overlaid on a Radarsat-1 mosaic of Antarctica. The light blue dashed line represents the southern boundary of the LAS. The cyan dashed line is the grounding line of the Amery Ice Shelf. The brown solid line represents the boundary of sub-basins feeding into the LAS.

The southern end of the Amery Ice Shelf is defined by a number of movement markers near the Prince Charles Mountains (light blue dashed line in Figure 1.1). The northern terminus of the LAS is near 69°S, where is 9° farther north than the ice front of the Ross Ice Shelf (Fricker *et al.*, 2009) which is larger than the Amery Ice Shelf. The southern grounding zone of the Amery Ice Shelf has been widely considered to be

located around 71.5°S latitude (Budd *et al.*, 1982). Phillips (1999) and Fricker *et al.* (2002a) updated the grounding zone approximately 250 km south from its previous position. The positional accuracy of the grounded ice boundary was improved to ± 0.5 km by combining Landsat-7 imagery and ICESat/GLAS laser altimetry data (Bindenschadler *et al.*, 2011).

1.3 Importance of the Study under Broader Scientific Frame

Thought to be in existence for more than 33 Ma, the East AIS has been considered as one of the most considerable driving forces of global sea level (Bloemendal *et al.*, 2003). It encompasses about 90% of the ice in Antarctica (Bamber *et al.*, 2000), but the view of ice-sheet dynamics it has been extremely poorly sampled temporally as it is thought to be much less dynamic than the West AIS. Recent studies provide evidence manifests an unevenly speed-up of mass loss in Antarctica (Rignot *et al.*, 2008) with much greater ice loss from the West AIS, much of which is grounded below sea level. Pritchard *et al.* (2009) indicated that the dynamic thinning has dominated the mass loss of the West AIS.

The East AIS is found relatively stable and it would be affected by the global warming in long term. With the growing of the ice shelf, if the terminus ice cannot be supported and calved, large icebergs are produced. According to the remote sensing records, it is believed that the most recent iceberg calving event in the LAS occurred between late 1963 and early 1964 with the calving of a large iceberg of approximately 10,000 km² (Fricker *et al.*, 2002b). Since then, monitoring the dynamic changes of the

LAS has generated interests among scientists who are not only interested in understanding the previous dynamic changes which have occurred in the LAS, but also in deducing the calving pattern and cycle of the LAS (Fricker *et al.*, 2002b).

As an important glaciological process, ice shelf rift propagation is usually driven by some short-term environmental forcings, such as wind speeds, tidal amplitudes, and sea-ice fraction (Bassis *et al.*, 2008). Nevertheless, the Amery Ice Shelf rifting was deduced to be triggered by internal glaciological stress (Bassis *et al.*, 2008). According to the satellite data (Fricker *et al.*, 2002b), it was suggested that the two longitudinal-to-flow rifts in the northern terminus of the Amery Ice Shelf started to open in 1988 or earlier, which is substantial to monitor the dynamic changes of the LAS as a system in long-term.

1.4 Research Objectives

This study aims to measure the surface velocities of the LAS to investigate whether significant changes in velocities have occurred over the period extending from the late 1980s to the 2000s, and to determine the mass balance changes due to velocity dynamic variations among separate time periods. Figure 1.2 represents the milestone and indicates the research gaps left by the previous studies. This dissertation is to bridge these previous findings by mapping the surface velocities during 1988-1990 and 1999-2004, and extend the timeline to 2007-2011. This study assesses the long-term spatio-temporal variability of the LAS. Detailed research objectives are as follows.

- Derive accurate and dense surface velocity measurements for the LAS during the time periods of 1988-1990, 1999-2003, and 2010-2011 using archived sequential satellite images acquired by multiple satellite sensors (e.g. Landsat and MODIS).
- Document the spatio-temporal variability of the surface velocities of the LAS derived from satellite images pairs (e.g. Landsat and MODIS) between late 1980s, 1990s, and 2000s (Liu *et al.*, 2006).
- Estimate mass balance changes and evaluate the stability of the LAS during the three time periods. Identify possible acceleration and deceleration.

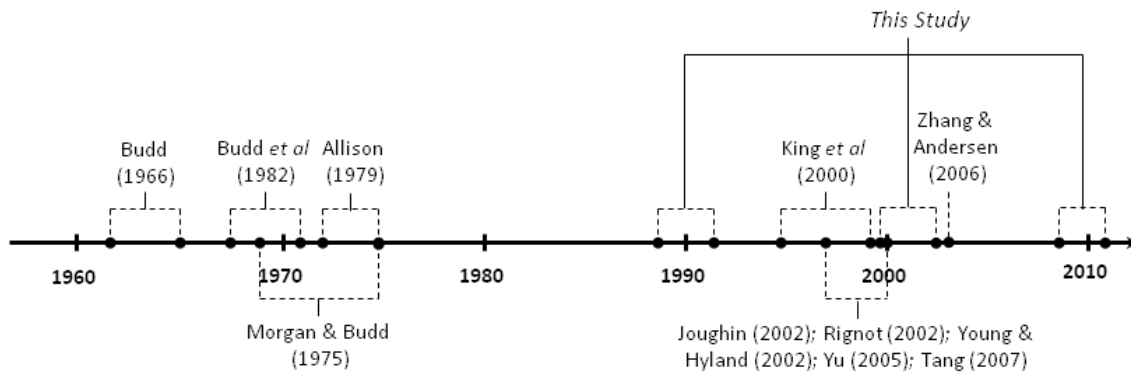


Figure 1.2 Timeline of existing velocity observations over the LAS as well as the study periods for this research.

The previous surface velocity measurements of the LAS can be summarized into two categories: (1) historic field measurements and (2) remote sensing measurements derived from SAR imagery. These conditions obstruct updates of surface velocity mapping in long term; thus, there is a need for better understanding of dynamics and the unexpected variations of the LAS. This study presents an easily applicable approach employing freely distributed optical images and utilizing a feature tracking method, which uses an open source software package. Additionally, this research extends the surface velocity measurements of the LAS spatially and temporally.

In this research, surface velocity measurements of the LAS will be derived using high spatial resolution sequential optical satellite images (e.g., Landsat). These observations will provide a view of the up-to-date behavior and stability of the LAS over the past two decades. For surface velocity mapping of the LAS, this study fills two major gaps for the time periods of 1988-1990 and 2007-2011. As an effort, this study not only improves insight into the stability of the Amery Ice Shelf over the last few decades but provides necessary validation for previous surface velocity estimates using remote sensing. This study also contributes to the effort to achieve better and full understanding of the long-term dynamics of the AIS and its effects on the future global climate changes and sea level rise.

1.5 Study Approach

The execution of this research took place at two major stages. The first stage encompassed the derivation of surface velocities. Feature tracking (Bindschadler *et al.*,

1996; Leprince *et al.*, 2007) was used to extract velocity information from satellite data. Besides, offset-tracking (Strozzi *et al.*, 2002) and InSAR (Gray *et al.*, 1998) were also applied to compare the surface velocity measurement accuracy. The second stage addressed the estimations of mass balance variations using the observed velocity measurements. Following the flux gate approach (Wen *et al.*, 2008), snapshots of mass balance differences of the LAS were determined over the same time frames as the surface velocity measurements.

This study applied feature tracking method to Thematic Mapper (TM) and Enhanced Thematic Mapper Plus (ETM+) images to extract the remotely sensed observations of surface velocity fields of the LAS. In addition, offset tracking and InSAR were used in this study to develop the most recent surface velocity map of the LAS. Therefore, this study provides a better understanding of the stability of the LAS through estimating and analyzing the changes of glaciological characteristics, e.g. surface velocity, mass balance, and surface temperature, in time series.

Inclusive of Landsat-4 TM of 1988-1990, Landsat-7 ETM+ of 1999-2003, Aqua/Terra Moderate Resolution Imaging Spectrometer (MODIS) of 2000-2001 and 2007-2009, all of the datasets are attainable from the U.S. Geological Survey (USGS). To meet the research objectives, other image products such as Digital Elevation Model (DEM) and grounding line have been provided by National Snow and Ice Data Center (NSIDC). Additional geographic information datasets, such as ice thickness data, have been provided by British Antarctic Survey. An effort led by Ohio State University (Jezek, 2002) has been made to compile surface velocity product of the AIS using the

InSAR data acquired during 1997-2000 as part of the MAMM (Modified Antarctic Mapping Mission) and distributed by the NSIDC.

1.6 Structure of the Research and Dissertation

This investigation employed feature tracking to study the dynamic changes of the LAS in three time periods of late 1980s, 1990s, and 2000s. A review of surface velocity extraction techniques will be outlined in next chapter with a short description of the theoretical background. For convenience, Chapter II is split into sections that present the surface velocity measurements for each individual method. The surface velocity mappings and analysis of temporal variations in these velocities are variation presented in Chapter III. This chapter also presents and compares previous surface velocity estimates of the LAS region. Chapter IV summarizes the estimates of the mass balance and of the LAS during 1988-1990, 1999-2004, and 2007-2011. This next chapter remarks the mass balance and its variation analysis and specific findings and research outcomes of this study. The final chapter summarizes the major points of the research and suggests future directions. A variety of datasets are processed under a GIS environment to calculate the mass balance of the grounded portion of the LAS.

CHAPTER II

SURFACE VELOCITY DERIVATION OF THE LAS USING FEATURE TRACKING, OFFSET TRACKING, AND INSAR FROM MULTIPLE SATELLITE DATA

2.1 Overview

Ice velocity and flow pattern are important glaciological parameters for deriving information on the dynamics of the Lambert Glacier-Amery Ice Shelf system (LAS). Paterson (1994) noted that due to the intimate relationship with ice sheet/glacier mass balance, ice surface velocities represent the state at which ice is transported from upstream (accumulation) regions to downstream regions; hence, knowledge of ice velocity is essential to assess flow dynamics and mass balance variations. Measurements of ice motion are also important to some mass budget estimation models and regional climate models (Wen *et al.*, 2008; Rignot *et al.*, 2008). The spatial variability of ice velocity can be used to interpret basal resistance related changes (Scambos *et al.*, 2004).

The *in situ* measurements are expensive and limited in both temporal and spatial scale. The advances of satellite remote sensing techniques have dramatically revolutionized our ability to monitor important glaciological parameters, such as ice surface velocity fields and associated flow pattern. Remote sensing is well-suited for ice velocity measurements over vast and remote regions, such as the Antarctic continent. Chapter one includes a detailed review of introductory principles for deriving ice surface velocities, as well as some previous observations. This chapter illustrates the derivation

of ice surface velocity fields of the LAS using three major surface velocity methods, feature tracking, offset tracking, and InSAR. Detailed instructions on the operating procedure are provided as well as a comparison of the methods.

2.2 Introduction

It could be extended back to 1963 when the first precise velocity *in situ* measurements were made in the LAS. Budd (1966) used electronic distance-measuring equipment and theodolites along terrestrial traverse routes to establish ice-movement markers. Two later expeditions in 1968 and 1969-1971 supplemented these measurements by resurveying the established ice-movement markers (Budd *et al.*, 1982). The highest velocity was found near the northern terminus of the LAS along the flow line and was estimated to be over 1200 m yr^{-1} . Further measurements were implemented by establishing new ice-movement stations. A resurvey of the existing ice-movement stations was completed in the 1990s. A number of additional ice-movement stations were established between 1972 and 1974 around the southern end of the Amery Ice Shelf, where the highest velocity was 230 m yr^{-1} (Allison, 1979). Many techniques have been employed to measure surface velocities in the past decades. However, those previous field measurements are confined to transverse routes leaving large portions of the interior region without *in situ* observations. The previous surface velocity measurements in the LAS region have been summarized in Table 2.1.

Although the historical ground measurements are generally considered more accurate, remote sensing has been instrumental in enhancing our understanding of the

dynamics of the LAS. Remote sensing techniques for deriving ice surface velocities have been applied over the last decade and for the first time have tremendously increased coverage providing surface motion observations over most of the LAS (Hambrey, 1991; Young & Hyland, 2002; Yu, 2005; King *et al.*, 2007).

Ground and aerial echo-sounding data were collected across the LAS region from 1969 to 1974 (Morgan & Budd, 1975). Surface velocities on the LAS were estimated ranging from 231 m yr⁻¹ to 1950 m yr⁻¹ (Swithinbank, 1988). Between 1995 and 2000, King *et al.* (2000) used GPS technology to measure surface velocities on the Amery Ice Shelf. Comparisons on surface velocity measurements at different times suggest that the historic measurements have residual magnitude errors as much as 150 m yr⁻¹ (King *et al.*, 2007). The Precise Point Position (PPP) model proposed by Zhang & Andersen in 2006 is another method applied to determine the displacements of a point on the Amery Ice Shelf. This technique depends on high-quality GPS observations to achieve high accuracy velocity measurements. The point (69°26.27'S, 71°26.18'E) was tracked near the northern terminus of the LAS; the measured surface velocity was 2.25 m d⁻¹ (821 m yr⁻¹).

Table 2.1 Summary of previous surface velocity measurements observed in the LAS region.

Authors	Regions	Methods	Data Sources	Epoch	Observed Velocities (m yr⁻¹)
Budd (1966)	Amery Ice Shelf	Ice-movement markers surveying	Field work	1962-1965	-
Budd <i>et al</i> (1982)	Amery Ice Shelf	Ice-movement markers resurveying	Field work	1968-1969, 1969-1971	12-1228
Allison (1979)	Southern end of Amery Ice Shelf	Ice-movement surveying	Field work	1972-1974	0-230
Morgan & Budd (1975)	LAS	Ground echo-sounding surveying	Field work	1969-1970 , 1971-1972, & 1973-1974	231-1950
King <i>et al</i> (2000)	Amery Ice Shelf	Static GPS measurements	Field work	1995-1996, 1997-1998, 1998-1999 (Summer)	5-807
Fricker <i>et al</i> (2002)	Three imaginary flux gates	Feature tracking	TM imagery & aerial photography	1973-1989 (TM) & 1960-1974 (Aerial photos)	355-572
Joughin (2002)	LAS	InSAR & speckle tracking	Radarsat-1	1997-2000	0-1300
Rignot (2002)	Lambert Glacier	InSAR & speckle tracking	Radarsat-1 & ERS	1997	0-800
Young & Hyland (2002)	Amery Ice Shelf	InSAR	Radarsat-1	1997	0-1350
Yu (2005)	Lambert Glacier Basin	InSAR & Speckle tracking	Radarsat-1	1997-2000	0-1470
Zhang & Andersen (2006)	(69°26.27'S, 71°26.18'E)	Precise Point Position model	Field work	12/22/2003-12/27/2003	821
Tang (2007)	Amery Ice Shelf	Image matching	Radarsat-1	1997-2000	3-1547

The vast spatial distribution of surface velocity fields made it difficult to exploit the complete surface velocity mapping using any individual method discussed above. The most spatially comprehensive assessments of the surface velocities of the LAS were not provided until the mid-1990s (Joughin, 2002; Young & Hyland, 2002). The most spatially comprehensive assessments of the surface velocities of the LAS were not provided until the mid-1990s (Joughin, 2002; Young & Hyland, 2002). As shown in Table 2.1, there are three common methods used to observe remote sensing measurements of surface velocity in the LAS regions: feature tracking using sequential time series of satellite images, SAR interferometry (InSAR), and offset tracking.

Each surface velocity measurement technique has its own advantages and disadvantages (Table 2.2). Feature tracking using optical images can successfully derive surface velocity measurements, but the availability of optical images is usually limited by the long polar nights, the frequent cloud cover, and the featureless ice surfaces. SAR images have cloud penetrating ability and can successfully capture images during long polar nights. Even so, SAR images are riddled with speckle noise, and reduction techniques can reduce the SAR image accuracy. InSAR is very sensitive to slow surface motions, but it requires either high resolution DEM or repeated SAR image acquisitions with short baselines. Its phase unwrapping is also difficult to accomplish sometimes. As with conventional interferometry, offset tracking is also limited by temporal and other decorrelations, which cause the differences existing between the acquired images. The utilization of offset tracking can derive surface velocity estimates in both range and

azimuth directions not requiring phase unwrapping, but the velocity estimation accuracy is two orders worse than InSAR.

Conventional feature tracking is accomplished by manually tracking identical surface features in optical images (Hambrey & Dowdeswell, 1994). This technique is constrained by the presence of nunataks or other persistently existing points to aid image coregistration; but, such morphological features rarely exist in large scale regions, such as on an ice shelf surface. Furthermore, it is tedious and time consuming to manually track optical features and these velocity measurements are limited by the amount of identifiable features suitable for tracking. Hence, a cross-correlation algorithm using sequential optical images was developed to robustly measure surface velocities (Bindshadler & Scambos, 1991; Scambos *et al.*, 1992; Scambos & Bindshadler, 1993; Bindshadler, 1998). Successfully tracking the motion of small surface features through cross-correlation (Berthier *et al.*, 2003) requires that the same feature be detected reliably and consistently across sequential optical images. Because of their penetrating ability and its ability to function during the polar nights, SAR images are used to derive surface velocity fields through identifiable features, which is called SAR feature tracking to differentiate from conventional optical feature tracking method.

Table 2.2 Summary of pros and cons of five surface velocity derivation methods.

Methods	Prerequisite	Pros	Cons
<i>Feature Tracking</i>	Identifiable features	Robustness; Efficient for small ranges of velocity variations and less influenced by temporal decorrelation	Long polar nights, frequent cloud cover, and featurelessness; Suffers from miscorrelation
<i>SAR Interferometry</i>	Co-registered repeat-pass SAR images	High accuracy	Complicated phase unwrapping process
<i>Offset Tracking</i>	Repeat-pass SAR images	Less influenced by correlations; No requirement of phase unwrapping and coregistration	Suffers from image-wide estimation errors; Relatively low accuracy than InSAR

The same as feature tracking in the spirit, image matching is a method involving a multi-scale hierarchical cross-correlation. One major advantage of image matching over other methods is its efficiency of mapping relatively small ranges of surface velocity variations, but this method suffers from the miscorrelation problem. By processing the same Radarsat-1 dataset as the InSAR method, the image matching method has been applied to produce similar surface velocity maps of the LAS as well (Tang, 2007; Heid & Kaab, 2012; Liu *et al.*, 2012).

InSAR is a sensitive means to measure ice displacements (Strozzi *et al.*, 2002) with unprecedented precision (Joughin *et al.*, 2000). Many researchers have processed and analyzed InSAR data acquired by the Antarctic Mapping Mission (AMM-1) and MAMM to derive surface velocity mapping of the entire Antarctic continent. The InSAR method suffers from a complicated procedure for phase unwrapping which easily fails. Young & Hyland (2002) used InSAR to map networks of velocity estimates for the LAS, indicating speeds of nearly 800 m yr^{-1} in the confluence zone of the Lambert Glacier, roughly 350 m yr^{-1} at 200-300 km from the front of the Amery Ice Shelf, and over 1200 m yr^{-1} at the northern end of the LAS.

The offset tracking method investigates the slant-range and azimuth offsets of pixel patterns using statistical correlation computation (Burgess *et al.*, 2012). The offset vector fields derived from co-registered image pair represent the displacements between two images. Unlike InSAR method offset tracking is not influenced by the complicated phase unwrapping procedure and it is easier to use to observe the complete surface

velocity mapping; however, the estimation uncertainty of this method is not as good as InSAR.

Speckle tracking is the same as offset tracking and enables to cross-correlate and track the image speckle patterns between two repeat-pass SAR acquisitions (Gray *et al.*, 1998; Short & Gray, 2005; Kumar *et al.*, 2009). One advantage is that the speckle tracking method works well both in low-correlation and high-correlation regions by utilizing different search window sizes. Larger search window sizes are required in fast moving areas than in slow moving areas. It works well even in the absence of visible features when coherence between two images approaches a certain range; therefore, speckle tracking can be used when conventional interferometry is limited. The unresolved longer-wavelength errors exist as image-wide errors across the images due to the limits of search windows. Using a combined InSAR and speckle tracking approach, similar surface velocity estimates and patterns were observed by Joughin (2002), Rignot (2002), Yu (2005), and Liu *et al.* (2007) using Radarsat interferometric data.

2.3 Surface Velocity Retrieval

In this chapter, three common methods (feature tracking, InSAR, and offset tracking) are employed to estimate surface velocity fields using different satellite sensors: feature tracking using sequential cloud-free Landsat/MODIS images or SAR intensity images, offset tracking SAR intensity images, and InSAR. The error analysis is essential to assess the accuracy of these three surface velocity derivation methods. First, the expected accuracy is assessed by transformation of displacements into velocity fields.

Second, the measurements uncertainty indicated by the non-zero estimations in stable zones (e.g. exposed rocks, massif) is assessed. Finally, a comparison is conducted between the results made by this study and the published InSAR geodetic measurements (e.g. MEaSURES InSAR velocity and RAMP InSAR velocity estimates).

2.3.1 Surface Motion Retrieval by Optical Feature Tracking

2.3.1.1 Principles of Optical Feature Tracking

Feature tracking is based on an image-to-image cross-correlation algorithm (see Figure 2.1) to locate identical surface features from sequential images and measure the displacements in the frequency domain (Bindschadler & Scambos, 1991; Scambos *et al.*, 1992). Surface features are represented by the patterns of a group of individual pixels. By shifting small search windows across each single band image pair (Ayoub *et al.*, 2009), the displacement of the dominant feature within the window is computed through the normalized covariance correlation method (Bernstein, 1983). In the same corresponding central pixel, the north-south (NS) and east-west (EW) components of the correlation are recorded, as well as the signal-to-noise ratio (SNR), which we take as the ratio of peak correlation function to the average value.

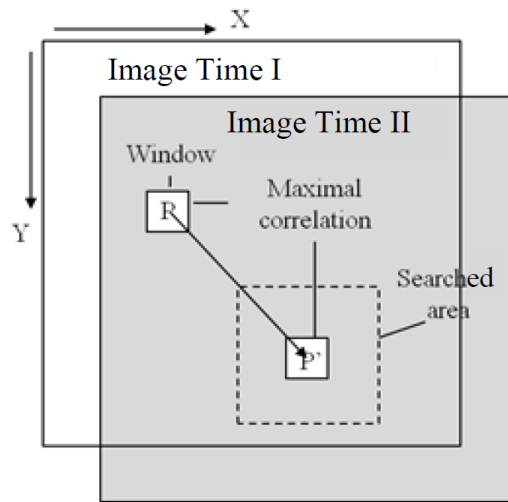


Figure 2.1 A sketch map of feature tracking (Huang and Li, 2009, p.575).

This algorithm is based on sophisticated assumptions: (1) a post-event image (the search image) comprises a pre-event image (the reference image) plus a shift translation; (2) the search image and the reference image share the same ground resolution; and (3) the search image and reference image are registered well.

A software package, Co-registration of Optically Sensed Images and Correlation (COSI-Corr) was implemented to accomplish the above procedures. This software package is a robust feature tracking program to obtain surface velocity measurements and is available from the Caltech Tectonics Observatory website (<http://www.tectonics.caltech.edu/>). Full details of the package can be found in Leprince *et al.* (2007).

2.3.1.2 Basic Processing Steps

Feature tracking can only be accomplished on co-registered single band image pairs. To process these images, three techniques were implemented to convert multiband Landsat images to single band and then co-register them. First, principle component spectral sharpening (after Welch & Ehlers, 1987) is applied to each 30 m Landsat image band using an associated 15 m panchromatic band. Then Principle Component Analysis (PCA; Richards, 1999) is performed, which is able to extract the most valuable component within the imagery. Last, image-to-image co-registration is achieved for the first principle components of both paired images by selecting Ground Control Points (GCPs).

The size in pixels of a maximum and a minimum window are defined by a power of two. By sliding the windows, the images will be correlated spontaneously. Patches with the largest window size are correlated using a peak correlation method (Leprince *et al.*, 2008). If the correlation succeeds, it is re-executed on patches with decreased size (power of two) to account for the displacement previously found (Ayoub *et al.*, 2009). The process iterates until the minimum window size is reached or the correlation fails. At each correlation there is a measure of the offset in column direction, row direction, and a signal-to-noise ratio (SNR, ranging from 0 to 1 and assessing the measure quality). The spacing of the computed grid is adjustable through changing the step parameter in pixels. For this work, vectors are obtained on a 1 km grid using a 256 x 256 pixel search window.

2.3.1.3 Post Processing Steps

Given by two components NS and EW, the displacement magnitude $\sqrt{NS^2+EW^2}$ can be converted to a velocity field by dividing by the time difference, while the direction can be computed following $\tan^{-1}(NS, EW)$. It is assumed that the magnitude or the direction of an individual velocity cannot vary significantly from the surrounding measurements within approximately 1 km distance according to current knowledge of dynamic glacier-ice shelf systems. All the measurements are filtered to exclude miscorrelations and to identify reasonably correlated patches. A simple magnitude filter and an additional direction filter are applied, considering the fact that velocities vary gradually rather than abruptly. Excluding measurements with a low SNR (below 0.95) is an efficient in removing most remaining miscorrelations. We developed a set of Interactive Data Language (IDL) programs to carry out the three filter procedures by assigning unique quality control codes. However, not all miscorrelated point velocities are identifiable, and thus some final manual refinements were required.

2.3.1.4 Data Preparation

The Landsat images used for the feature tracking procedure were provided by USGS. Four images (Table 2.3), path/row 128/112(111), are used to study the surface velocity of the LAS near the confluence zone. They were acquired on 6 March 1988, 18 March 1989, 14 November 2001 and 19 December 2002. The images were processed using Environment for Visualizing Images (ENVI4.8) software package, with an installation of the Cosi-corr program (Leprince *et al.*, 2007).

Table 2.3 List of Landsat data acquired for feature tracking.

Sensor	Path/Row	Acquisition Dates	Pixel Size (m)
TM	128/111	1988/03/06	30
TM	128/112	1989/03/18	30
ETM+	128/112	2001/11/14	15
ETM+	128/112	2002/12/19	15

The Landsat ETM+ Scan Line Corrector (SLC) mechanism failed on May 31st, 2003, which caused wedge-shaped scanning gaps. A gap-filling software called Frame and Fill was designed by NASA to fill gaps in the ETM+ imagery. This gap-filling processing is applied with the Level 1 terrain corrected (L1T) geotiff format images received from the USGS. Alternatively, the Landsat 4 data and Landsat 7 data acquired prior to May 31st, 2003 are free of scan line gaps and able to be processed directly. Figure 2.2 provides two examples of how the Frame and Fill software works.

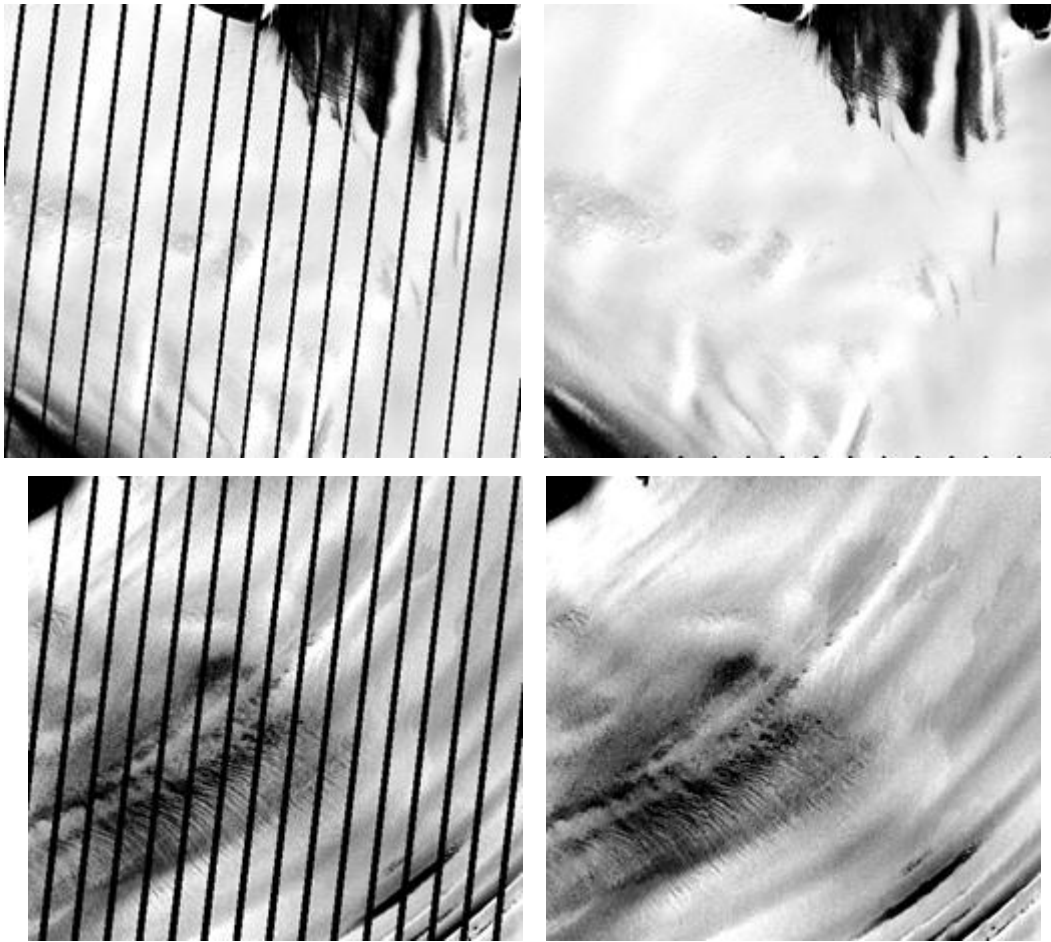


Figure 2.2 Examples of SLC off-correction of ETM+ images using Frame and Fill software.

2.3.1.5 Results of Optical Feature Tracking

After the initial set of velocity fields was obtained, we took several steps to remove those of poor quality using a magnitude filter, a direction filter, and a SNR filter. As the partial displacement map, Figure 2.3 indicates the result is a detailed map with dense surface velocity fields.

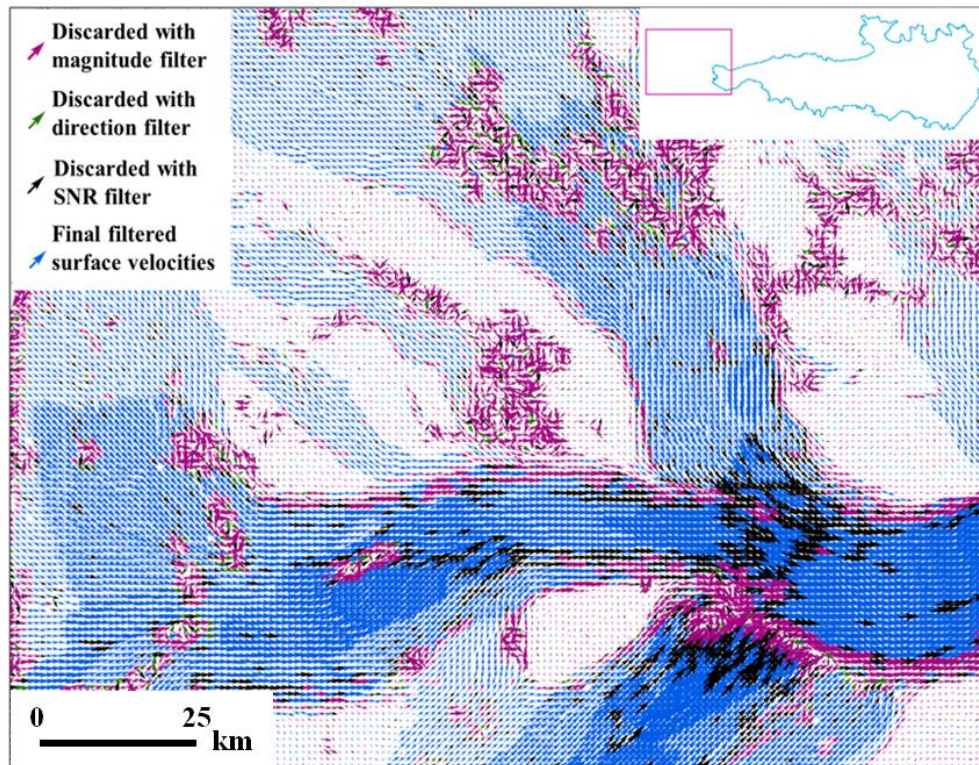


Figure 2.3 Partial color-coded point velocities of the LAS determined from cross correlation of ETM+ image pair of 2011/11/14 and 2002/12/19 in the confluence zone of the Mellor, Fisher, and Lambert glaciers. The inset map shows the location of the velocity study.

Most of the obvious erroneous vectors, which are anomalously high or low, have been discarded using the magnitude filter (magenta arrows). The direction filter (green arrows) discards another group of velocities that are inconsistent with the flow features, defined as ± 10 degrees or higher deviation from the defined direction. The SNR filter

(black arrows) helps to identify those low correlated patches. Fast moving ice surfaces usually decreases correlation and is observed with low SNR values.

Tobler's First Law of Geography, "Everything is related to everything else, but near things are more related than distant things." (Tobler, 1970). The spatial interpolation is explored by fitting a user-defined semi-variogram model. An ordinary Kriging method (Nguyen & Herring, 2005) is performed on the 1 km gridded velocities illustrated in Figure 2.3 to analyze the spatial pattern of the velocities. The interpolation result is illustrated in Figure 2.4. The lag size and number of lags are 2500 m and 20 respectively. All Kriging interpolations are conducted using ArcGIS 10.0 Spatial Analyst Toolset.

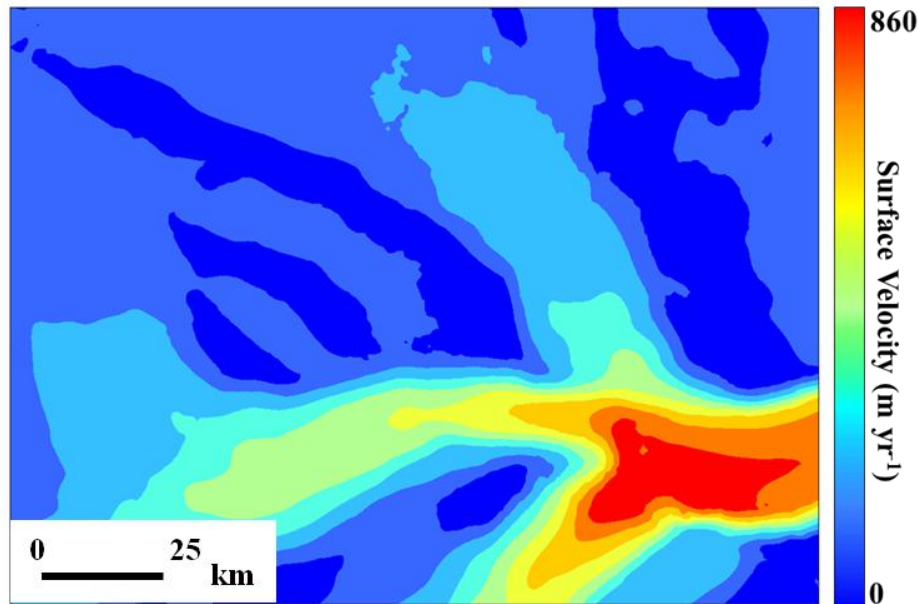


Figure 2.4 Predicted magnitudes of velocities obtained from the analysis of the velocity fields illustrated in Fig 3 (units m yr^{-1}) using ordinary Kriging.

To examine weather temporal differences significantly affect the velocity measurements, we perform two congruency tests for velocity magnitude and direction. Five datasets in the confluence zone are utilized where repeat measurements were observed. The histograms of these datasets are shown in Figure 2.5. Each dataset consists of 285 surface velocity measurements. At the 95% confidence level, the congruency test succeeds for both magnitude and direction of the above five datasets. Table 2.4 indicates that significant temporal differences (*Difftemporal*) have little effect on the feature tracking derived surface velocity measurements. This increases the possibility to pair the images and to obtain repeated measurements.

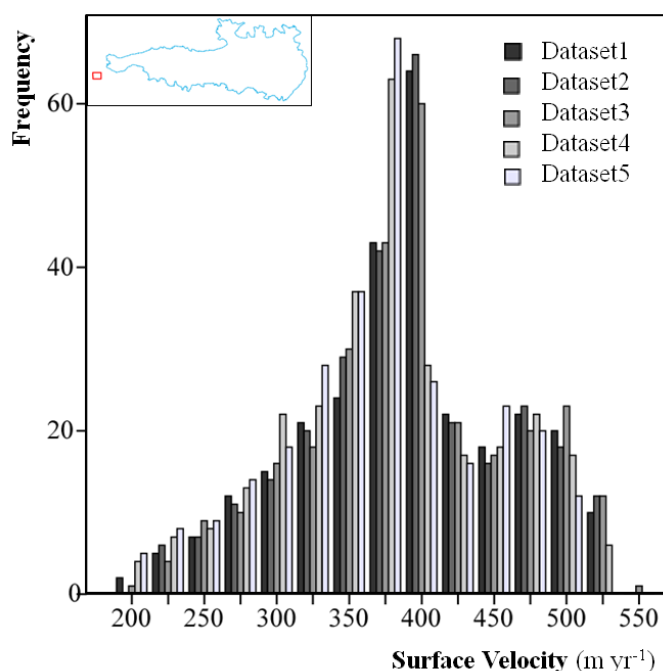


Figure 2.5 Histograms of five datasets used for congruency tests. The inset map shows the location of the five datasets.

Table 2.4 Congruency test on the five datasets.

ID	$M_{\text{magnitude}}$ (m yr ⁻¹)	$\sigma_{\text{magnitude}}$	$M_{\text{direction}}$ (degrees)	$\sigma_{\text{direction}}$	$Diff_{\text{temporal}}$ (days)	Image Pairs (dd/mm/yyyy_dd/mm/yyyy)
1	378.3	70.0	43.4	6.0	384	12/09/2001_12/28/2002
2	380.3	71.5	43.7	6.0	400	11/14/2001_12/19/2002
3	377.3	71.4	44.3	5.9	681	01/14/2000_11/25/2001
4	363.7	72.4	43.5	6.2	681	01/14/2000_11/25/2001
5	356.4	70.8	40.9	6.5	695	01/14/2000_12/09/2001

The displacements of detectable features visible on the Landsat images are tracked and computed in NS and EW directions for each time-adjacent image pair using a normalized cross-correlation procedure (Leprince *et al.*, 2007). From these two components, the velocity magnitude and directional angle are computed and plotted as the length and direction of each velocity vector arrow (Figure 2.6). Obvious velocity gradients are shown in Figure 2.5 by color coded the vector arrows.

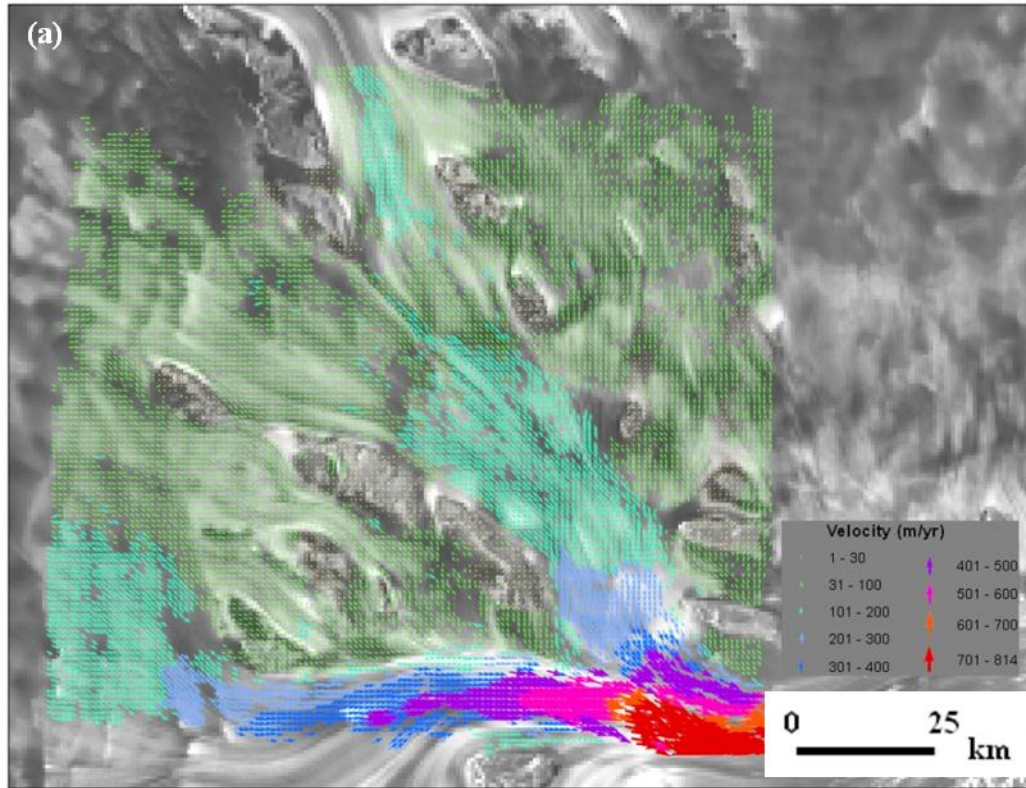


Figure 2.6 (a) Color-coded point velocities of the LAS determined from cross correlation of a TM image pair consisting of images acquired on 1988/03/06 and 1989/03/18; (b) Color-coded point velocities from cross correlation of an ETM+ image pair consisting of images acquired on 2001/11/14 and 2002/12/19 for the similar region as Figure 2.6(a).

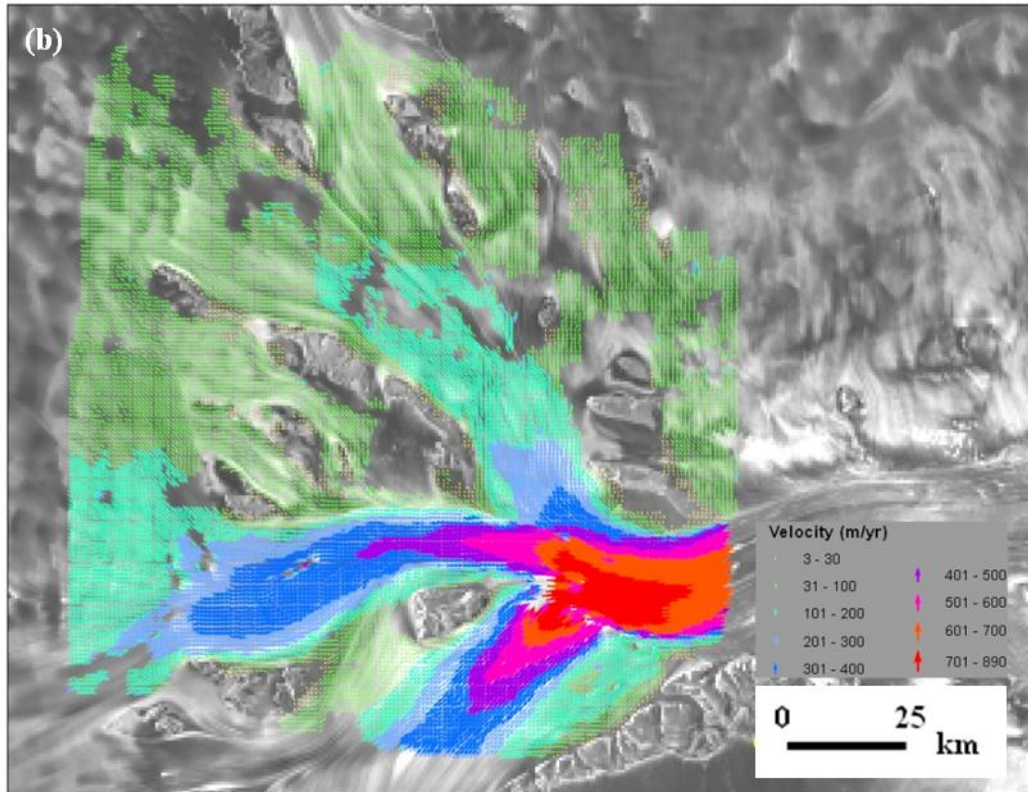


Figure 2.6 continued.

2.3.1.6 Error Analysis

Error analysis is fundamental to estimate the applicability of the feature tracking method to surface motions. The major uncertainty in velocity measurements consists of two components: image correlation ambiguity and co-registration error. These errors somewhat depend upon the amount of GCPs and the geological location of ice-free areas (e.g. exposed rocks). Dietrich *et al* (2007) estimated an uncertainty of 0.1-0.3 pixel due to the rough glacier surface and surface topography changes. Although it is difficult to

quantify, a correlation uncertainty of 0.3-0.5 pixel can be conservatively estimated (Ahn & Howat, 2011, Skvarca *et al.*, 2003). In this research, the surface velocity measurements over the ice-free regions (known as the stable zone) and fast-moving regions are studied.

It is assumed there are no displacements occur over ice-free regions. In this sense, the non-zero measurements result from image correlation ambiguity and co-registration errors. Three datasets of measurements derived from each individual ETM+ pair are analyzed as illustrated in Table 2.5a. The error analysis indicates that the uncertainty of feature tracking is approximately one pixel.

Table 2.5a. Magnitudes of velocity vectors over ice-free regions used for error analysis.

Group No.	Path	Row	No. of Vectors	V_max	V_min	Av.
				m yr⁻¹		
1	126	112	9	22.3	6.2	14.4
2	127	112	59	16.1	9.9	12.8
3	128	112	95	11.2	2.8	6.7

There are usually no GCPs distributed in the fast-moving regions. The uncertainty of surface velocity measurements is estimated by the repeated observations for the same geographic location. Forty-four surface velocity measurements are collected

from three dispersedly distributed locations (Table 2.5b). The uncertainty is computed as the mean percentage difference between the maximum value and the average value of each group. As shown in Table 2.5b, the uncertainty of the feature tracking derived surface velocities of the fast-moving regions vary between -7.4% and 15.6%.

Table 2.5b. Magnitudes of velocity vectors over fast-moving regions used for error analysis.

Group No.	No. of Vectors	V_max	V_min	Av.	Diff_vmax	Diff_vmin
		m yr⁻¹			%	
1	12	323.0	256.0	297.3	8.6	13.9
2	10	301.6	230.1	274.6	9.8	16.2
3	10	278.6	223.8	268.5	3.8	16.6
<i>Average</i>					7.4	15.6

2.3.1.7 Comparison with Published InSAR Velocity Estimates

To illustrate the potential of feature tracking for measuring surface velocities, a comparison is conducted between the published InSAR measurements and this study along four velocity profiles, which are extracted along the flow lines. Three velocity profiles of 10 km width and one velocity profile of 19 km width are respectively

generated along the flow lines of Fisher Glacier, Mellor Glacier, Lambert Glacier, and the southern end of Amery Ice Shelf. The width of each profile sufficiently includes all the fast flow ice surfaces. The velocity measurements derived from feature tracking and InSAR are plotted individually for each velocity profile (Figure 2.7a-d).

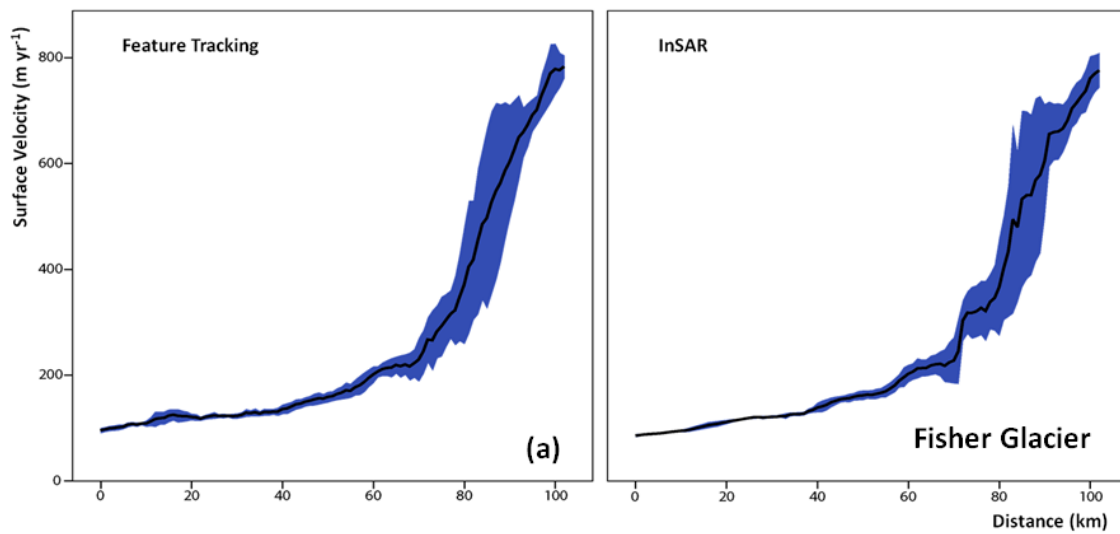


Figure 2.7 (a-d) Surface velocity profiles for the Fisher Glacier, Mellor Glacier, Lambert Glacier, and Amery Ice Shelf; (e) Comparisons between feature tracking and InSAR measurements along four velocity profiles.

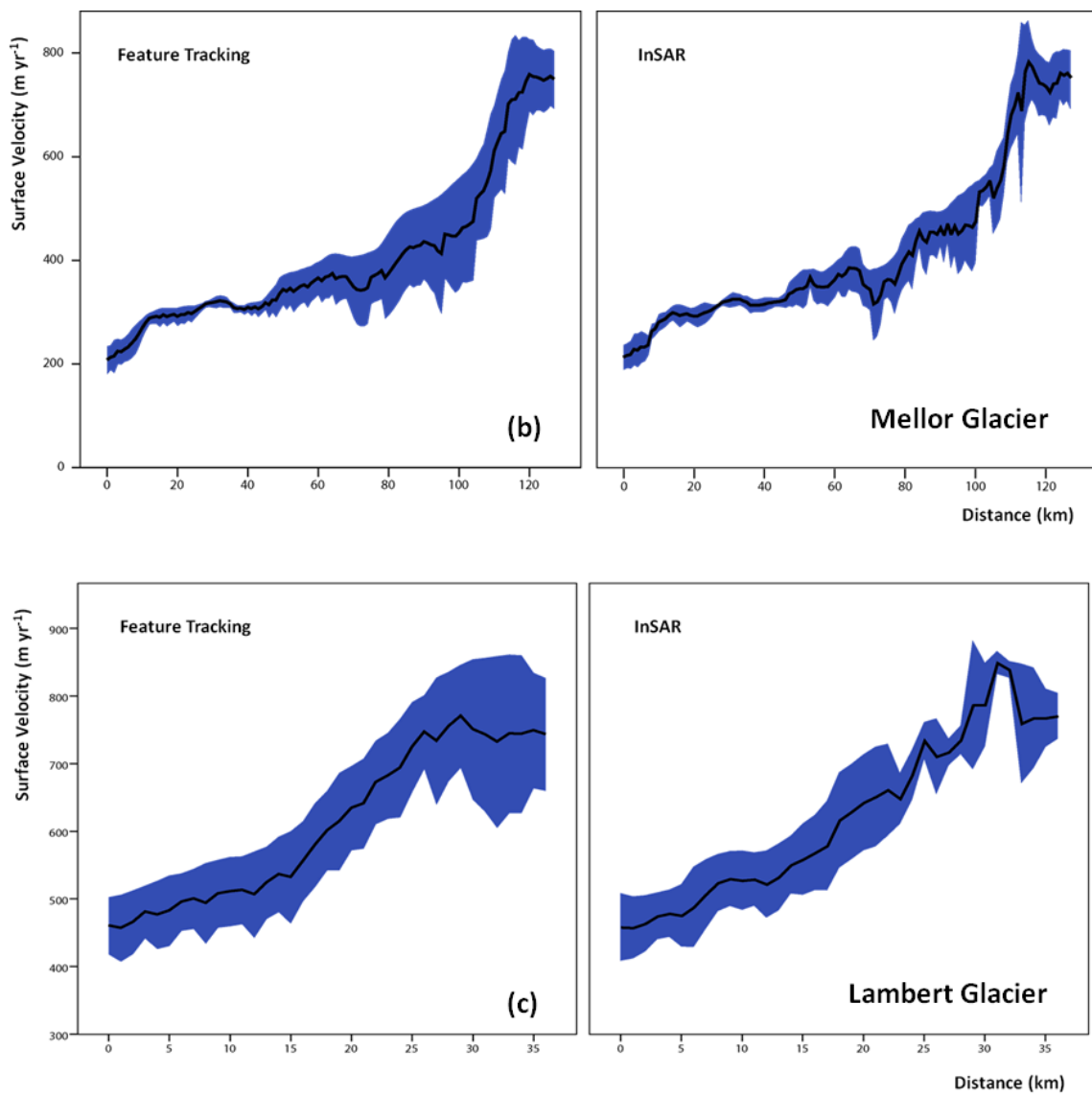


Figure 2.7 continued.

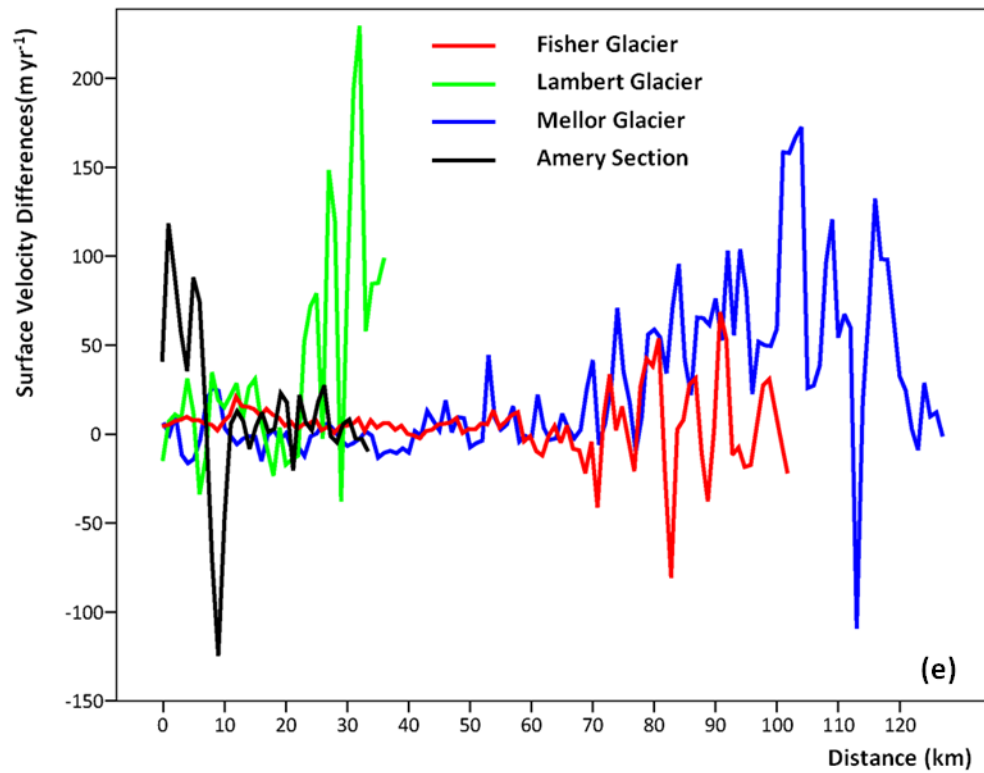
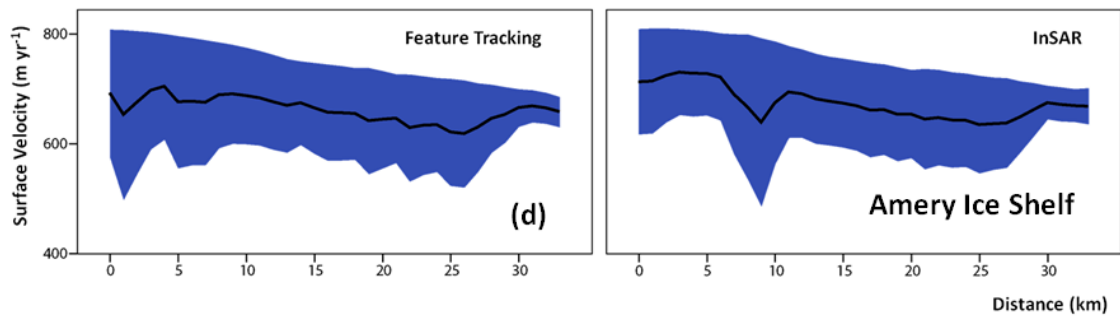


Figure 2.7 continued.

Close agreement is observed between surface velocity profiles. Across the flow direction, InSAR measurements have fewer variations than feature tracking in some

portions due to the fact that some InSAR measurements are missing. In addition, the differences between the mean of feature tracking-derived and InSAR-derived measurements for each velocity profile are plotted in Figure 2.7e. Most of the differences vary between -50 and 50 m yr^{-1} with a trendline of zero. Several high difference values are caused by the InSAR dataset again due to missing data.

2.3.2 Surface Motion Retrieval by SAR Feature Tracking

Without interference from cloud cover and polar nights, SAR images are an ideal good alternative to optical images for feature tracking. Fahnestock *et al.* (1993) and Luckman *et al.* (2003) suggested the potential of SAR feature tracking to routinely map surface velocities in sequential images.

2.3.2.1 Principle of SAR Feature Tracking

The repeat-pass reliability and highly consistent imaging geometry of SAR data allows the surface feature patterns to be tracked over considerable distances. The foundation of the SAR feature tracking method is based upon the intensity of cross correlations between image patches of SAR images obtained at different times (Scambos *et al.*, 1992; Lucchitta *et al.*, 1995; Luckman *et al.*, 2003). Two dimensional surface velocity fields are derived from repeat-pass SAR data.

2.3.2.2 Basic Processing Steps

The coherent interference of waves rebounded from different elementary scatters results in speckle noise in SAR images. This not only complicates the image

interpretation, but also it reduces the accuracy of images. For speckle reduction, SAR data can be frequently multi-look processed by averaging neighborhood pixels (Chen, 1999). Hence, the processing procedure of SAR feature tracking consists of multi-looking intensity images, projecting onto a known map reference, process of feature tracking between images, process of filtering, mosaicking the velocity measurements from many image pairs, and visualizing the results.

Each intensity image was applied with 9-look processing, which makes the spatial resolution 180 m. Before finally visualizing the results, a filtering process was completed to remove the noisy measurements based on a suitable degree of confidence. Measurement removal is determined based on the magnitude, direction filters and SNR ($\text{SNR} > 0.8$), which was discussed in the section on optical feature tracking.

2.3.2.3 Data Preparation

We use ENVISAT ASAR data on the ascending orbital path 271 acquired on August 8th, 2009 and July 24th, 2010 (Table 2.6). These Image Complex Mode (IMS) products were obtained from the European Space Research Institute (ESRIN). The incidence angle is approximately 23.0°. The images are applied with 4-look multi-look processing before any further data processing and analyzing. All the SAR processing is conducted using the GAMMA software package, excluding the process of feature tracking accomplished using Cosi-corr.

Table 2.6 Acquisition parameters for the image analyzed.

Sensor	ENVISAT ASAR	
Orbit/Frame	271	271
Acquisition Dates	2009/08/08	2010/07/24
Incidence angle (°)	23.0°	
Pass Direction	Ascending	
Pixel size of range/azimuth (m)	7.90/3.96	

2.3.2.4 Results of SAR Feature Tracking

The acquired SLC images need to be processed and converted into intensity images for further processing (Figure 2.8a). Through the process of feature tracking, dense spatially distributed two-dimensional velocity measurements were obtained. The spatial distribution pattern of surface motions is well illustrated (Figure 2.8b).

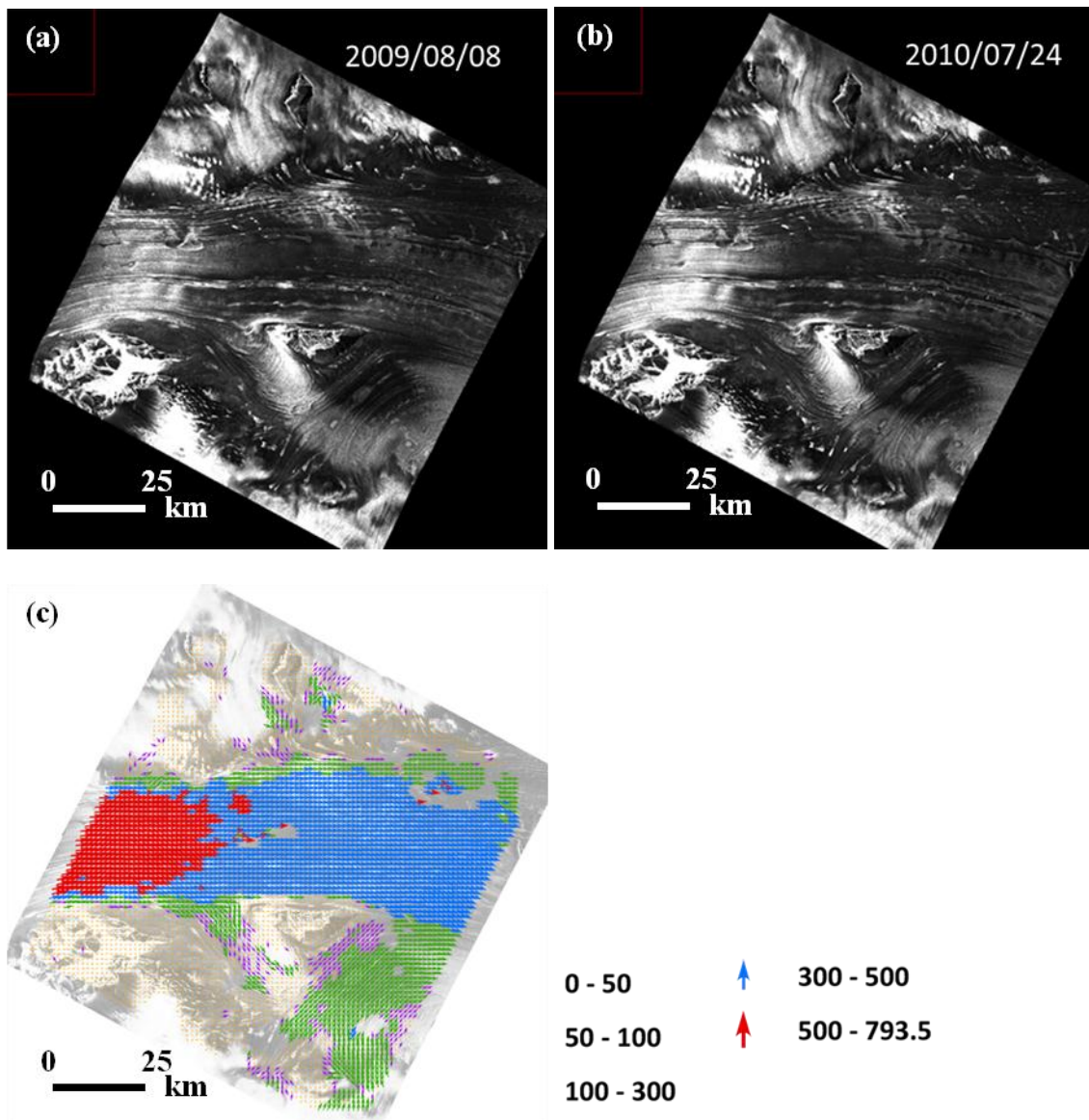


Figure 2.8 (a) Preprocessed ENVISAT ASAR pair for SAR feature tracking; (b) Color-coded SAR feature tracking-derived surface velocity fields.

2.3.2.5 Error Analysis

Similar to optical feature tracking, the surface velocity measurements over the ice-free regions (known as the stable zone) were analyzed. It is assumed that there are no displacements in such regions. Therefore, the non-zero measurements result from uncertainty errors.

Forty-two measurements over the ice-free regions derived from SAR feature tracking method are used for error analysis. The maximum and minimum values are 32.5 and 4.2 respectively. Overall, the uncertainty of SAR feature tracking is approximately 0.1 pixel.

2.3.2.6 Comparison with Published InSAR Velocity Estimates

A comparison was made between the SAR feature tracking measurements and the most recently published Antarctic velocity mapping, which was completed by the Earth Science Data Records for Use in Research Environments (MEaSUREs) program. Within the spatial coverage presented in Figure 2.8, a 68 km long velocity profile is created along the relevant portion of flow line. Across the velocity profile, the measurements are extracted as far as 11 km.

By plotting the highest and lowest velocity ranges (Figure 2.9), clearly is observed the similar variation pattern along the flow direction. Overall, the SAR feature tracking measurements are 50 m yr^{-1} less than the InSAR measurements. This difference is most likely caused by the lower spatial resolution of the SAR images used for feature tracking. To reduce the speckle noise, 9-look multi-look processing is applied to the

SAR images, which unfortunately results in lowering the spatial resolution at the same time.

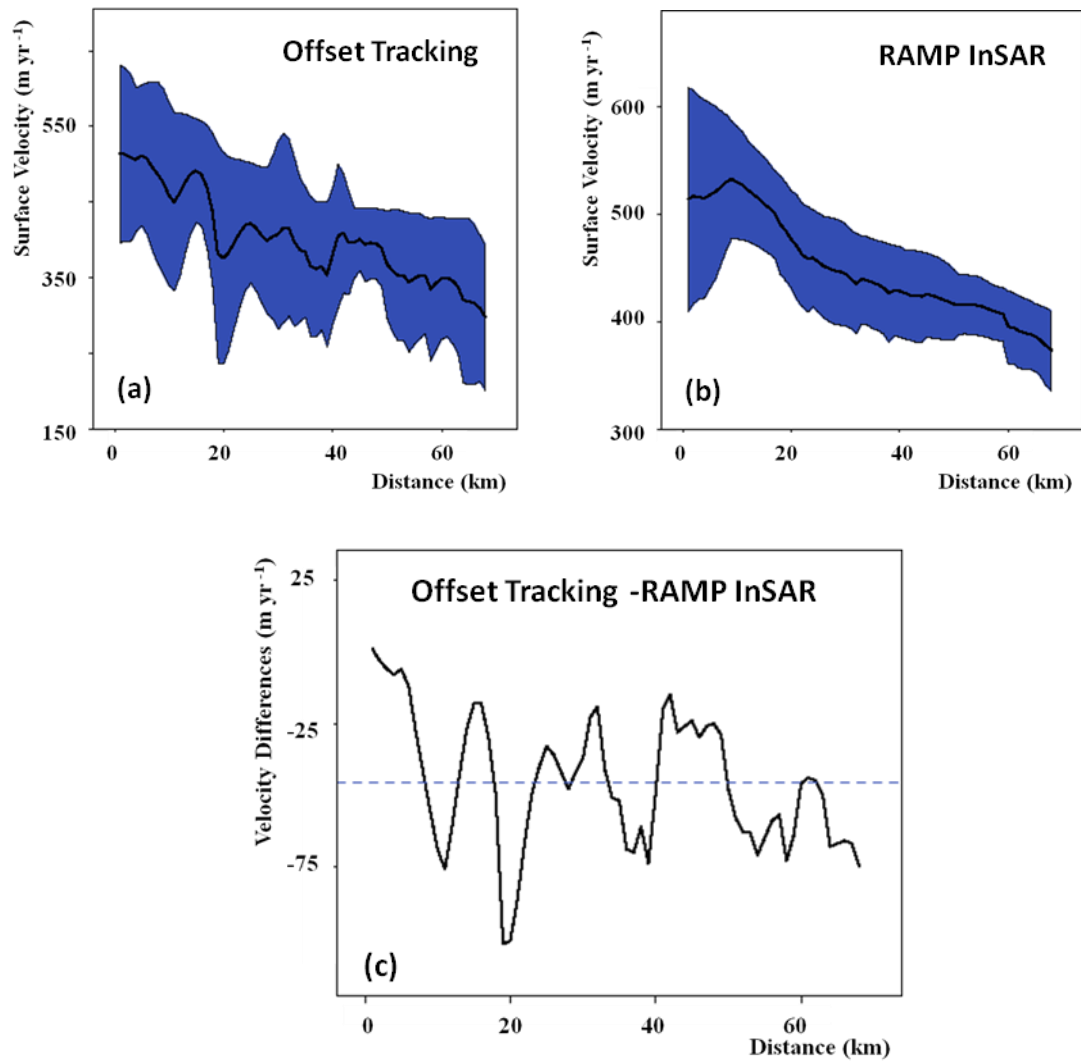


Figure 2.9 Comparisons between SAR feature tracking and InSAR measurements (MEaSURES project) along one individual velocity profile.

2.3.3 Surface Motion Retrieval by Offset Tracking

2.3.3.1 Principles of Offset Tracking

Offset tracking is a SAR image-based method which can compute the sub-pixel displacements occurring between the acquisition time intervals of the co-registered intensity image pairs in the spatial domain (Strozzi *et al.*, 2002). Offset tracking even works well in the absence of visible features (Joughin, 2002). When use of feature tracking or InSAR is not possible to apply, offset tracking is an ideal alternative method for estimates of surface velocities, although the accuracy of the offset tracking method is two times less than InSAR measurements (Strozzi *et al.*, 2002).

Success in estimating the local image offsets depends upon the presence of nearly distinct features in the two SAR images at the scale of the employed patches. The intensity pattern of the two images is correlated once coherence is retained. Oversampling rates are applied to the image patches, and a two-dimensional regression fit to model the correlation function around the peak is determined by interpolation. An effective correlation SNR is determined as the confidence level of each offset by comparing the height of the correlation peak relative to the average level of the correlation function.

Offsets are measured using patches that are $M_1 \times M_2$ (range x azimuth) pixels at a set of positions in the image. The desired offsets in range and azimuth directions are yielded by the two-dimensional correlation function $C(n_1, n_2)$, which is defined as (2.1) (Werner *et al.*, 2005).

$$R(n_1, n_2) = \sum_0^{M_1} \sum_0^{M_2} I_1(m_1 + n_1, m_1 + n_1) I_2^*(m_1, m_2) \quad (2.1)$$

where I_1 and I_2 are the detected over-sampled SLC data $S_1 S_1^*$ and $S_2 S_2^*$. The power spectrum of the intensity image $I_1 = S_1 S_1^*$ or $I_2 = S_2 S_2^*$ has twice the samples of the SLC data, hence the oversampling factor of the SLC is set to 2. Oversampling improves the sampling of the desired correlation function obtained from the patches.

For simplicity, offset fields are mapped by selecting small image patches centered on distinct features and searching a subsequent image for matching patches. Unlike feature tracking, offset fields are generated with a cross-correlation of detected patches of SAR intensity images and computed at the peak of the cross-correlation function (Figure 2.4). Offset fields between two SAR images acquisition time interval are calculated in both slant-range (e.g. in the line-of-sight of the satellite) and azimuth (e.g. along the orbit of the satellite) directions. The offsets are caused by orbital geometry and surface movements; they are related to orbit configurations and are separated using precision orbit and GCPs, then the offsets related to surface displacements are estimated.

2.3.3.2 Basic Processing Steps

In the absence of topographic-related deformation and ionospheric effects, the offset fields in the slant-range and azimuth directions are related to satellite orbit configuration of the two SAR images and displacement occurring between the acquisition intervals. To conduct the offset tracking processing, three major stages are

implemented. First stage is determination of the orbital offset between two SAR images. A bilinear polynomial function is constructed by cross correlation of distinct surface features of intensity images. Then second stage is precise estimation of the offsets. According to the position indicated by the bilinear polynomial function, the offsets are precisely estimated by adjusting the patch sizes for offset estimation. Third stage is transformation to displacement from offsets. The bilinear polynomial function is used to separate the orbital offsets from the displacement estimations, which are computed both in range and azimuth directions. Final is geocoding of the results. Due to that the displacements are derived in the SAR geometry, the results are expected to be converted in the ground range-azimuth coordinate systems.

2.3.3.3 Data Preparation

We use ENVISAT ASAR data on the ascending orbital path 271 acquired on August 8th, 2009 and July 24th, 2010 (Table 2.5, Figure 2.10). These Image Mode (IM) products are obtained from European Space Research Institute (ESRIN). The incidence angel is approximately 23.0°. All the SAR processing is conducted using GAMMA software package, excluding the process of offset tracking accomplished by Cosisi-corr.

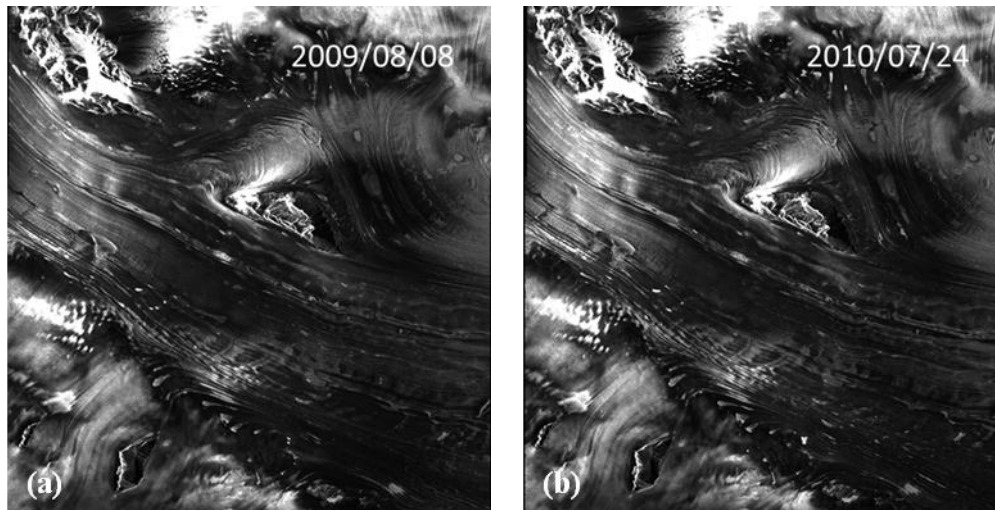


Figure 2.10 9-look Intensity ENVISAT ASAR images of (a) 2009/08/08 and (b) 2010/07/24 for offset tracking based on radar geometry.

2.3.3.4 Results of Offset Tracking

Offset tracking results are first discussed for the LAS regions. The slant-range and azimuth displacements were computed respectively to provide a better view of a two-dimensional velocity field (Figure 2.11a-b). The results illustrate the spatial distribution patterns of surface velocities. Scaling the displacements to meters per year, the surface velocities are shown in Figure 2.11c.

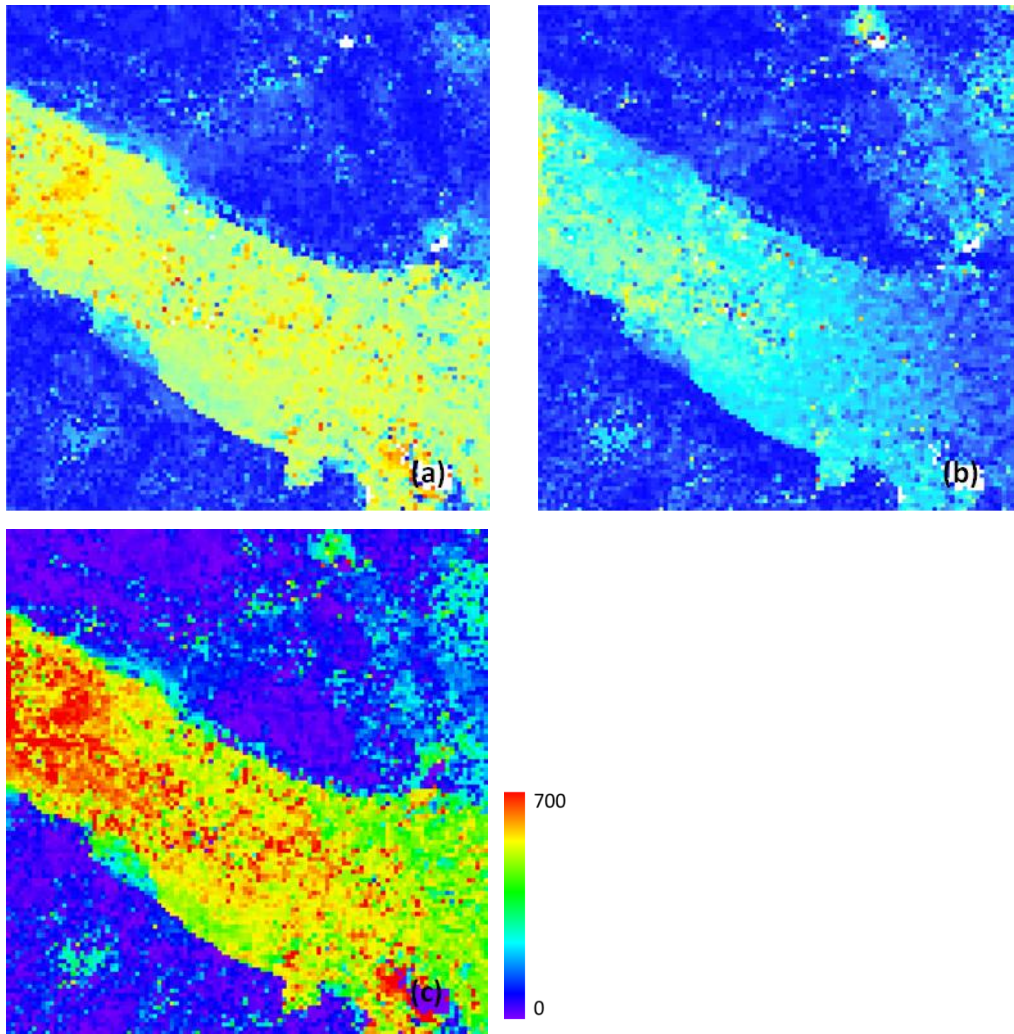


Figure 2.11 Offset fields under Radar geometry in (a) slant-range and (b) azimuth direction; the intensity of the displacement is shown in (c).

2.3.3.5 Error Analysis

Error analysis is fundamental to assess the applicability of offset tracking to surface velocity fields. In this study the offset estimations are scaled into m yr^{-1} for further comparison. The expected uncertainty is conducted by estimating the non-zero

velocity measurements in stable regions (e.g. exposed rocks). The extracted non-zero velocities are computed and represent the uncertainty of the offset tracking method. Our analysis suggests that the uncertainty of offset tracking is 0.06 m d^{-1} (22.1 m yr^{-1}).

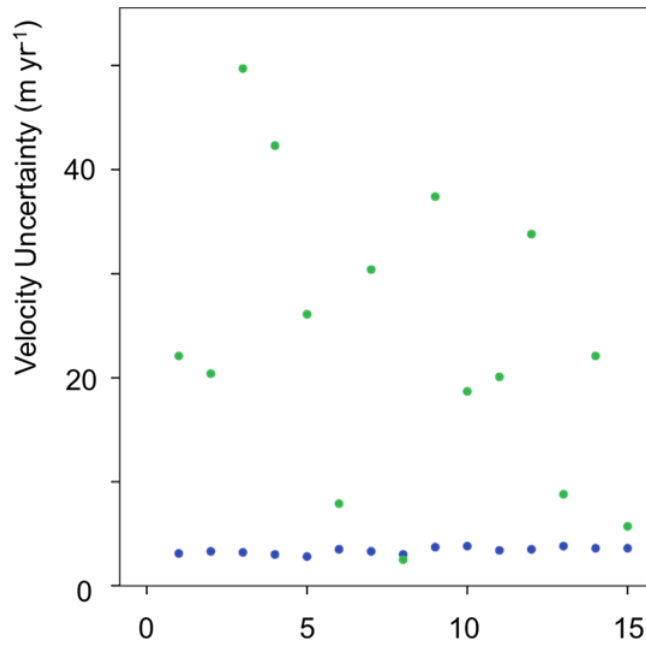


Figure 2.12 Error analysis for the offset tracking method using sixteen measurements (x axis).

2.3.4 Surface Motion Retrieval by SAR Interferometry (InSAR)

InSAR is adopted in this study for its advantages; (1) sensitivity to small changes (Joughin *et al.*, 1996); (2) unconstrained by weather conditions (compared with optical data). One of the major limitations of InSAR is that velocities are only given in radar

look direction (one dimension), whereas the feature/offset tracking methods give two-dimensional velocities. Another disadvantage of InSAR is temporal decorrelation (Zebker & Villasenor, 1992), which might be caused by excessive surface motions, snow accumulation or redistribution through precipitation or wind, and surface melt.

2.3.4.1 Principle of InSAR

Two complex SAR images of the same surface area but acquired at slightly different orbit configurations are combined to exploit the interferometric phase difference occurring between the acquisition time intervals (Rosen *et al.*, 2000). The interference patterns caused by phase differences of the two images are known as interferometric SAR or InSAR. After co-registering the consistently processed SAR pairs, interferometries can be implemented to estimate the phase difference using maximum coherence as a means for matching small patches between complex SAR image pairs (Derauw, 1999). Hence, an interferogram is actually a plot of phase difference shifts as a function of position. The phase difference ϕ in the resulting interferogram contains contributions from several independent terms (Bamler & Hartl, 1998) and is generally presented as a linear summation given as:

$$\phi = \phi_{topography} + \phi_{displacement} + \phi_{atmosphere} + \phi_{noise} + \phi_{flatten} \quad (2.2)$$

where $\phi_{atmosphere}$ is atmospheric-related phase caused by propagation delayed, which often occurs in the troposphere and ionosphere; ϕ_{noise} is system noise; $\phi_{flatten}$ (flat-earth

phase) is an orbital phase depending on the viewing geometry of the SAR image pair; $\phi_{displacement}$ is displacement-related phase caused by local displacements of the ground surface between consequential image pairs; and $\phi_{topography}$ is topographic-related phase due to the relief of the imaged area. If all the four terms $\phi_{topography}$, $\phi_{flatten}$, $\phi_{atmosphere}$, and ϕ_{noise} are neglectable from the interferogram, then the motion-related phase can be derived to exploit a displacement map.

Since the phase difference $\phi_{displacement}$ is measured in interval from 0 to 2π as a relative phase difference, the ambiguity constituted in the number of wavelengths needs to be configured. This is called phase unwrapping. During this process, the discrete fashion of the fringe pattern is transformed to continuous values.

It is found that the phase difference ϕ is sensitive to the term $\phi_{displacement}$ (Strozzi *et al.*, 2007). Once the phase difference $\phi_{displacement}$ is unwrapped, then the absolute phase difference is ready to be converted to surface velocities. The geometry for the surface velocity measurement from InSAR technique depicted schematically in Figure 2.13 explains the conversion relationship between $\phi_{displacement}$ and surface velocity term projecting in the slant range direction.

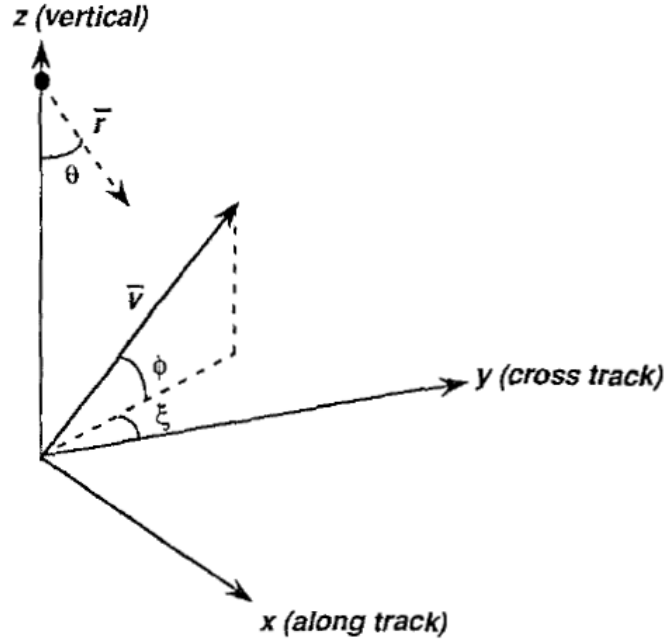


Figure 2.13 Schematic map of the geometry for the measurement of ice surface velocity from InSAR (Kwok and Fahnestock, 1996).

According to this geometry shown in Figure 2.13, the surface velocity in slant range direction V_r is given by:

$$V_r = \frac{\lambda \phi_{displacement}}{4\pi\Delta T} + V_0 \sin\theta \cos\epsilon \quad (2.3)$$

where λ is the radar wavelength; ΔT is the time interval; V_0 is a baseline velocity; θ is the radar look angle; and ϵ is the ice flow direction. The second term is considered a spatially constant component of the surface velocity. In this fashion, the contribution to

the displacement field (or to any other local optical-path variations) has resulted from the wavelength, displacement-related phase, and acquisition time intervals.

2.3.4.2 Basic Processing Steps

Interferometric processing of SAR imagery allows determination of surface velocity fields with centimeter-level precision. According to Equation 2.2 and Equation 2.3, InSAR processing is designed with the following steps. (1) Selection of suitable interferometric SAR image pairs, which aims to minimize atmospheric term $\phi_{\text{atmosphere}}$ and noise term ϕ_{noise} ; (2) geometric co-registration of selected InSAR pairs, which are required to be registered prior to determining the phase difference and estimating the baseline; (3) generation of the interferogram and estimation of interferometric correlation; (4) correction of the flat-Earth phase, which aims to remove the term ϕ_{flatten} ; (5) adaptive filtering of interferograms; (6) unwrapping of difference phase and removal of any ambiguities (Goldstein et al., 1988). Phase information is measured in modulo 2π but motion information requires the absolute phase be determined; (7) conversion of phase to displacement in slant range direction; (8) geocoding of the results transforming from the SAR geometry to map geometry.

All collected SAR image pairs are precisely co-registered on a reference sampling grid for the unique master image acquisition acquired for this project. During InSAR processing, only InSAR pairs of small perpendicular baseline (<100 m) will be used to generate the differential interferograms and coherence images. The interferograms with correction of the curved Earth phases will then be filtered to reduce

the amount of phase noise, which is always present in SAR images. The final step is the removal of atmosphere artifacts, unwrapping the differential interferometric phases, conversion of the phase values to displacement units, and geocoding the output products.

2.3.4.3 Data Preparation

The ERS-1/2 Tandem SAR Mission operated from 1991 to present and which makes it possible to collect a considerable amount of SAR data at C-band (Attema, *et al.*, 1998). ERS-1 follows ERS-2 with a gap of 24 hours, which makes a one-day time interval between successive acquisitions. The short time intervals increase the possibility to detect ice motions, and the fast motions in particular. This study used a pair of ERS-1/2 tandem SAR images obtained from European Space Research Institute (ESRIN) archives as Level-1 SLC data. These two images are on ascending orbital paths 23577 and 3904 (Table 2.7), with an incidence angle of 23.5° . The topographic influence in the interferogram was removed during the processing using the DEM (Liu *et al.*, 1999) delivered by the NSIDC. The InSAR data processing is implemented in the GAMMA software (Strozzi *et al.*, 2002).

Table 2.7 Two ERS-1/2 tandem SAR SLC images suitable for interferometric processing.

Sensor	ERS-1	ERS-2
Orbit/Frame	05669/5067	25342/5066
Acquisition Dates	05/20/1996	05/21/1996
Incidence angle (°)		23.5
Effective baseline (m)		-51.3
Coherence		0.97
Pass Direction		Ascending
Pixel size of range/azimuth (m)		26.3/30.0

2.3.4.4 InSAR Results

An interferometric motion analysis is carried out based upon a pair of SAR images from the ERS-1/2 Tandem Mission in 1996 with GAMMA software for data processing. The amplitude and the coherence images are shown in Figure 2.14 (a-b); the interferogram shows the surface motion related phase difference that occurred during the image acquisition interval, converted from which the surface velocity measurements are illustrated in Figure 2.14 (d-g). The distribution pattern of surface velocities is observed clearly across the image spatial coverage, from upstream to the outlets of sub-basins, the velocity variations range from 0 to 1.05 m d^{-1} .

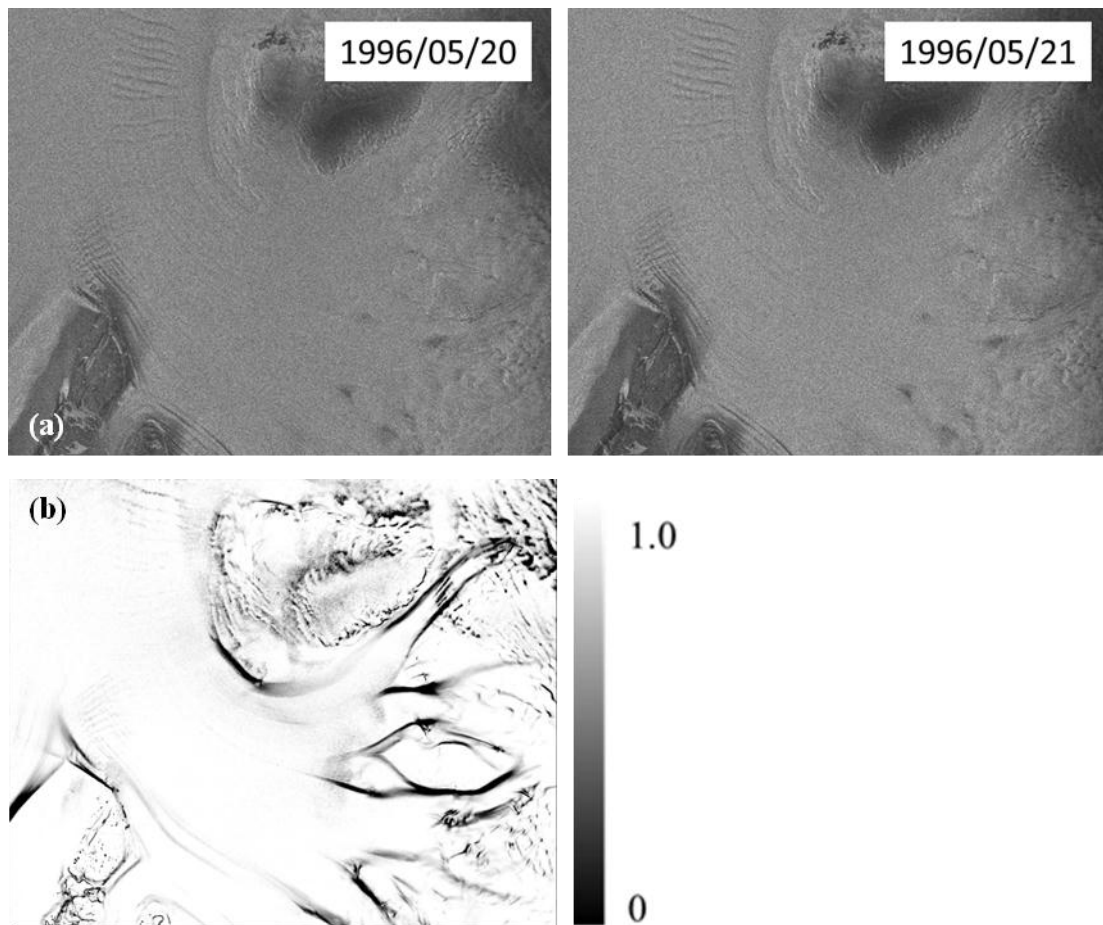


Figure 2.14 (a) Intensity image; (b) Wrapped Interferogram derived from the ERS-1/2 InSAR pair. The topographic contribution to the phase has been removed using topography generated by the RAMP DEM; (c) Coherence image. (d) Slant-range component displacement; (e) Azimuth component displacement; (f) Horizontal displacement map; (g) Geocoded velocity map.

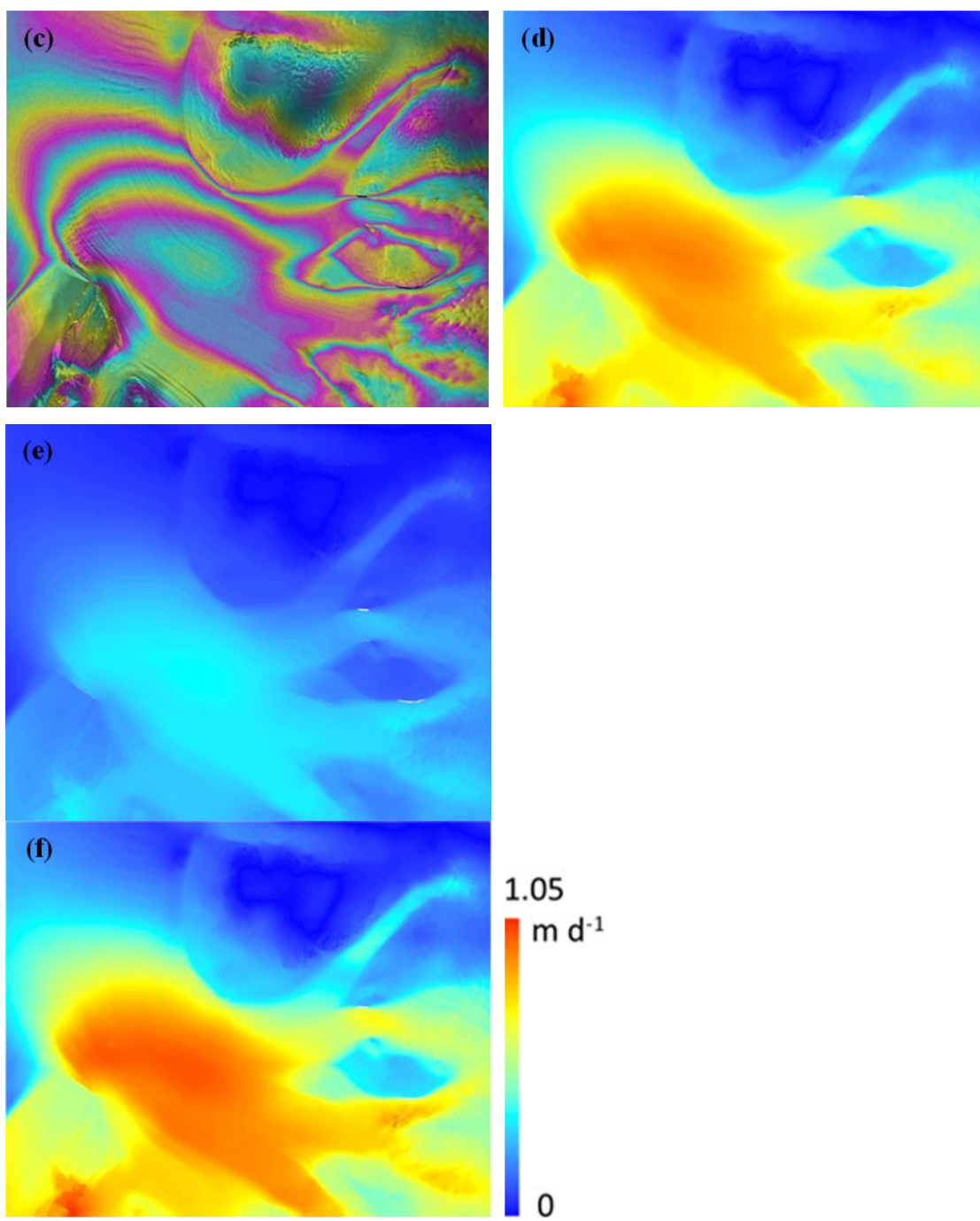


Figure 2.14continued.

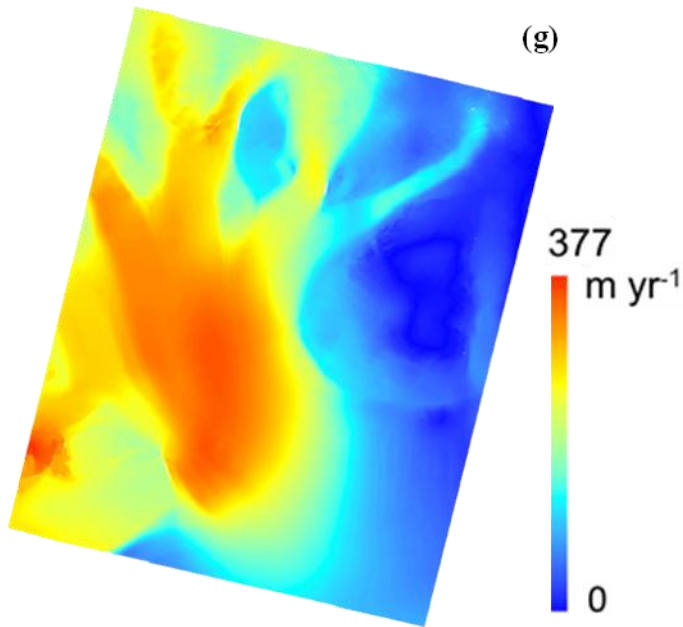


Figure 2.14 continued.

2.4 Discussion

The above analysis outcomes manifest three methods appropriate to explore surface velocity fields for the LAS. SAR images are ideal substitutes for optical images, particularly in Antarctica. The reduction of speckle noise can be conducted by oversampling of the SLC images prior to estimating the displacements, which is also called multi-look processing. According to the error analysis, the uncertainty of SAR feature tracking is approximately 0.1 pixel, while the pixel size is determined by oversampling procedure. Optical and SAR feature tracking is suitable to determine the surface velocity measurements, achieving similar accuracy as InSAR. It is found that the spatial distribution of surface velocity fields affects the retrieved measurements. When

displacement has been accumulated enough to be identified, the uncertainty caused by temporal decorrelations among image pairs can be ignored. Feature tracking rarely works when there are no sufficient glacier surface features, such as crevasses and nunataks, regardless of whether the data are optical images or SAR images. Considering the data availability of datasets, feature tracking method is highlighted by this study to enable a better view of the surface velocity spatial distribution of the LAS using Landsat images received from USGS. Thus, accuracy is proportional to pixel size and actual velocity magnitude.

Offset tracking is useful when feature tracking is limited by insufficiency of visible surface features. The coregistration of SAR images is implemented automatically using the GAMMA software package. The offsets can be computed in slant-range and azimuth directions respectively first and converted into resultant displacements later. However, the accuracy of offset tracking is significantly lower than the feature tracking method, which makes offset tracking method not suitable for high resolution surface velocity mapping.

InSAR works well in the slow-flowing regions. This approach relies upon high coherence and proper physical baselines between the images as well as accurate DEM products. To maintain high coherence between images, the time separation between images is usually several days or months, which makes the InSAR-derived measurements not sufficiently representative for mean annual velocity fields.

Appropriate time intervals between images should be considered in data selection both for feature tracking and offset tracking methods, since the rapid flow regions make

it possible to use a short time interval. The velocity field derived by two sequential satellite remotely sensed images only represents the motion occurring between the acquisitions of the two scenes, which is an average velocity. To accumulate detectable displacement accumulations, the acquisition intervals usually are longer than one year. In fact, detectable displacement accumulations are not sensitive to seasonal variations of surface velocity.

Though frequent cloud cover severely hampers the acquisition of suitable high resolution optical satellite images near the ice shelf margin, the growth of crevasses and lack of features on ice surface heavily restricts a high density of surface velocity observations. The temporal durations between image pairs usually are over one year, resulting is that the feature tracking-derived measurements not sensitive to seasonal variations. Prerequisite of enough cumulative displacements, the accuracy of the optical feature tracking derived measurements is approximately one pixel in the stable regions. For instance, for Landsat TM data (30 m), the velocity retrieval errors can approach a maximum of 15-30 m yr⁻¹. If the ice surface moves fast (over than 300 m yr⁻¹), then the accuracy is observed varying from -7.4% to 15.6%. It is an important step to make the features indefinable between images by choosing the datasets with longer time acquisition intervals for slow-moving regions (typically a year for fast-moving regions). It is noted that the image correlation procedure can fail in areas of high lateral shearing (e.g. at the confluence zone), which this can be identified by distortion and rotation of surface features and great variations in motion directions. Since enough measurements

are observed around such regions, this problem does not impact further measurements and analysis.

Overall, each method discussed in this chapter has its potential and certain limitations to mapping the surface velocities. The presented velocity measurements are mutually consistent, which reveals the feasibility and accuracy of feature tracking technique. Among these three proposed methods, InSAR is the most accurate technique to extract the surface velocity information. In addition, offset tracking is an ideal method to complement the other two with the advantage of no need for phase unwrapping and coregistration. Considering the measurement accuracy and availability of datasets, optical feature tracking has its advantageous over other methods. As a consequence, feature tracking is used by this study for the surface velocity mapping and analysis of the LAS in multiple time series.

CHAPTER III

SURFACE VELOCITY VARIATIONS ANALYSIS OF THE LAMBERT GLACIER- AMERY ICE SHELF SYSTEM (LAS)

3.1 Background

Grounded ice is the most important control on the dynamics and mass balance changes of the Lambert Glacier-Amery Ice Shelf system (LAS). Based on previous researches, considerable spatial variations in the surface velocity have been mapped in the LAS. However, the temporal and spatial sparsity of velocity measurements have made it difficult to exploit and understand the nature of any dynamic changes in the LAS. Likewise, estimations of mass flux are susceptible to large uncertainties due to the sparse velocity measurements. The long-term investigations of the behavior of the LAS provide us the knowledge of the glacial basin evolution or any significant changes of the LAS in East Antarctica. Any significant variation in surface characteristics (e.g. surface velocity, surface slope, and elevation) can be measured; however these measurements can be subject to research bias (Bindshadler, 1993). Short-term variations in satellite-derived surface velocities have been found at two largest outlet glaciers in Greenland and are used in estimations of the ice discharge and mass loss (Howat *et al.*, 2007). To reduce the possible effects caused by seasonal, annual, and intra-decadal fluctuations in the surface velocity measurements, a record of velocities at the decadal scale are required. Long-term observations of surface velocity also enable to explain any observed rapid change prior to ice shelf collapses (Rack *et al.*, 1999).

Changes in velocity structure and widespread ice acceleration have been detected in the Greenland Ice Sheet (Rignot & Kanagaratnam, 2006) and some large outlet glaciers in Greenland (Howat *et al.*, 2007), which are perhaps related to the increased basal lubrication from surface meltwater penetration (Thomas *et al.*, 2009). The variability in the ice surface velocity over time and space is sensitive to climate changes, but most of those previous studies and findings were based on a relatively short period (several years to decades) of observations.

Early velocity surveys were implemented by re-measuring the sparsely distributed ice-movement markers (Budd *et al.*, 1982). Those early measurements provided fundamental baseline information for assessing the variations of surface velocity when compared with the later observations.

King *et al.* (2007) were the first to precisely evaluate the velocity variations of the Amery Ice Shelf over a 30-year period. They compared surface velocity derived from geodetic quality measurements in the 1960s and more recent GPS measurements to assess the changes of surface velocities in the northern LAS regions for the period 1968-1999. A comparison at nine locations indicated a small velocity slowdown ($\sim 0.6\%$ or $\sim 2.2 \text{ m yr}^{-1}$) of the ice shelf. This study has provided important new measurements in the long-term velocity changes, but the spatial sparsity of the field measurements has made it difficult to explain the nature of the dynamics of the ice shelf.

Besides the velocity magnitude and the variations in time series, estimating changes of large ice shelf fronts across reference positions is also considered a substantial indicator to global change (e.g., SCAR/IGBP, 1989). Since the early 1970s,

the Amery Ice Shelf front has been studied using a variety of satellite image types including the military Keyhole satellites (KH-7 and KH-9), Landsat Multispectral Scanner (MSS), Thematic Mapper (TM), Enhanced Thematic Mapper Plus (ETM+) images, and the recent Radarsat-1 and ENVISAT SAR images. By the slant-range analysis of satellite radar altimeter data, it is estimated that mean annual motion of the Amery Ice Shelf front during the period of 1978-1994 is $1.03 \pm 0.04 \text{ km yr}^{-1}$ (Zwally *et al.*, 2002b). It is also suggested that such seaward motion may sustain for decades and lead to a large-scale calving events.

The last major iceberg calving event from the Amery Ice Shelf is thought to have occurred between late 1963 and early 1964. The survey during 1936-1968 (Robertson, 1992) indicated a mass loss of 9660 km^2 from the Amery Ice Shelf front, which is approximately one fifth of the Amery Ice Shelf in 1963 (Budd, 1966). The advance of the ice shelf front is surveyed by this study using satellite images acquired during 1972-2012, prior to which the historic positions of the ice shelf front were delineated based on Fricker *et al.* (2002a).

As highlighted in Chapter II, feature tracking enables the information of ice flow characteristics to be determined from the satellite images during the time interval between the satellite images. Hence, feature tracking has the potential to map the surface velocities for multiple time periods. The newly developed two dimensional surface velocity maps are included in this chapter, which cover the time periods of 1988-1990, 1999-2004, and 2007-2011. The time intervals of processed satellite images are usually one to two years. This chapter also focuses on the comprehensive assessment of surface

velocity variations of the LAS and determination if any significant change has occurred between the observation acquisition intervals.

3.2 Data Acquisition

For feature tracking, Landsat Thematic Mapper (TM) images acquired from 1988-1990 and the Landsat Enhanced Thematic Mapper Plus (ETM+) images acquired from 1999-2004 and 2007-2011 are used for this study. All Landsat images are Level1G (L1G) products with the systematic radiometric and geometric correction provided by U.S. Geological Survey (USGS). Eighteen TM image pairs and eighty-one Landsat ETM+ image pairs of cloud-free (cloud cover is less than 10%) are used for feature tracking. A significant number of ETM+ images are obtained for the time period of 2007-2011 due to the need of Scan Line Corrector (SLC)-off correction following the failure of the scan line corrector on Landsat 7 on May 31st, 2003 (Maxwell *et al.*, 2007). Frequent cloud cover severely hampers the acquisition of suitable sequential Landsat image pairs. Thus, several Moderate Resolution Imaging Spectroradiometer (MODIS) single visible band (channel 02) images acquired during 2000-2001 and 2007-2009 for the northern part of the Amery Ice Shelf provided by the National Snow and Ice Data Center (NSIDC) serve as substitutes where no cloud-free Landsat image coverage available. These MODIS images at the spatial resolution of 250 m have been processed to map the surface velocities of 1988-1990 using the same method. Table 3.1 summarizes the remote sensing satellite data acquired for this study.

Table 3.1 Summary of acquired satellite datasets.

Images	Epoch	Scenes(s)	Used for	Provider
<i>MSS</i>	1972	2	Advance of Ice Shelf Front	USGS
<i>TM</i>	1988-1990	36	Feature Tracking	USGS
<i>TM</i>	1988	2	Advance of Ice Shelf Front	USGS
<i>ETM+</i>	1999-2003	28	Feature Tracking	USGS
<i>ETM+</i>	2009-2011	134	Feature Tracking	USGS
<i>ETM+</i>	2002-2012	8	Advance of Ice Shelf Front	USGS
<i>MODIS</i>	2000-2001	2	Feature Tracking	NSIDC
<i>MODIS</i>	2007-2009	4	Feature Tracking	NSIDC

The Radarsat-1 Antarctic Mapping Project (RAMP) InSAR velocities during 1997-2000 were provided by the Byrd Polar Research Center at the Ohio State University, which are compared with the feature tracking-derived surface velocities for the same time period. The forty-seven *in situ* velocity GPS measurements made during 1990-1999 and published by King (2002) are used for the validation of the velocities computed in this study using feature tracking (Table 3.2). According to the acquisition intervals, these *in situ* velocities are separated to two groups for the comparisons during the two time periods of 1988-1990 and 1999-2004 to compare with two of the three velocity maps are produced.

Table 3.2 Forty-seven GPS velocity measurements made in the Amery Ice Shelf during 1990-1999 (King, 2002).

Site	Latitude	Longitude	Velocity(m yr ⁻¹)	Direction(°)	Epoch
GA27	-71.518	69.8481	359.65	23.88	1990
GA23	-71.252	68.9478	205.66	23.72	1990
GA24	-71.398	69.9833	355.45	18.75	1990
GT82	-70.532	66.0744	65.52	73.36	1990
GA02	-70.108	68.6085	221.21	90.97	1990
GT62	-70.314	66.167	50.69	64.94	1990
GT06	-70.35	65.5977	76.5	80.96	1990
GA04	-70.137	68.9462	268.13	68.85	1990
GA42	-70.187	69.4701	333.84	33.19	1990
GA26	-71.47	69.2596	324.73	26.72	1990
GT05	-70.502	66.4624	111	68.12	1990
GA21	-71.068	69.1838	259.1	16.58	1990
GA06	-69.935	69.4578	363.81	29.16	1991
GA29	-71.917	68.6695	382.04	35.87	1991
G282	-71.648	68.988	345.24	36.56	1991
GA05	-70.063	69.5286	375.45	31.31	1991
GA03	-70.043	68.6011	140.16	95.17	1991
GA34	-71.624	70.143	211.88	23.93	1991

Table 3.2 continued.

Site	Latitude	Longitude	Velocity(m yr⁻¹)	Direction(°)	Epoch
GA33	-71.487	70.5734	229.86	-6.59	1991
G31B	-71.706	69.5553	360.31	34.85	1991
GA35	-71.839	68.4332	394.9	34.03	1991
GA25	-71.404	68.6876	167.87	39.5	1991
GA32	-71.452	70.1348	333.45	15.77	1991
GA30	-71.641	68.4698	302.28	29.57	1991
GA01	-70.189	68.7332	247.22	80.44	1991
GA07	-70.16	69.9927	498.01	25.6	1991
G242	-71.287	69.7888	347.29	17.79	1991
GA11	-70.297	70.5976	442.51	20.4	1991
GA22	-71.204	70.2663	350.31	17.06	1991
GA09	-69.908	69.8481	435.99	28.91	1991
GA72	-70.268	70.1336	459.6	20.76	1991
GA08	-70.012	69.8596	457.48	28.48	1991
A130	-70.877	69.8569	355.46	10.79	1999
A129	-70.867	69.8456	355.17	10.7	1999
A308	-70.79	68.8905	4.83	11.09	1999
A33_	-70.546	70.2945	374.96	9.65	1999
A201	-70.867	69.8887	352.39	10.59	1999

Table 3.2 continued.

Site	Latitude	Longitude	Velocity(m yr⁻¹)	Direction(°)	Epoch
G2W1	-70.169	70.8614	472.18	29.02	1999
A301	-70.837	69.6985	347.9	10.39	1999
G1S1	-69.502	71.7206	806.08	44.58	1999
G1W1	-69.501	71.72	796.1	44.28	1999
G1E1	-69.501	71.7223	784.75	44.23	1999
A131	-70.881	69.8308	350.29	11.2	1999
A37_	-70.749	69.9884	359.07	9.2	1999
CAMP	-70.892	69.8733	353.26	10.95	1999
A35_	-70.641	70.1779	372.04	9.67	1999

3.3 Surface Velocity Mappings

To understand the dynamic changes of the LAS, the surface velocities are computed for multiple periods using feature tracking. The surface velocity mappings are made covering one to two year intervals during three separate time periods of 1988-1990, 1999-2004, and 2007-2011.

3.3.1 Surface Velocity Observations (1988-1990)

Thirty-six Landsat TM images are used to determine the LAS's surface velocities during 1988-1990 (Figure 3.1). The surface velocity vectors are derived using the feature tracking method and a complex surface velocity distribution is observed for the LAS

except the partial Amery Ice Shelf front. Sub-pixel displacements of the full resolution images are with steps of eight pixels through eighteen TM image pairs, yielding approximately 150,000 surface velocity vectors. Furthermore, the quality control procedure is applied to reduce miscorrelated estimations. The observed surface velocities vary from 0 to 1300 m yr⁻¹. Two substantial tributaries of the Fisher Glacier bifurcate and extended 180 km inland from the corresponding grounding line. The upstream Lambert Glacier meet the Fisher Glacier and the Mellor Glacier in the confluence zone where appear a complex surface velocity pattern. The velocities of all these three glaciers where they meet the grounding line are observed at approximately 800 m yr⁻¹. The surface velocities on the tributaries on both east and west sides of the Amery Ice Shelf are found ranging from 0 - 200 m yr⁻¹. The northern terminus of the ice shelf is advancing seaward in a north-easterly direction at about 1301 m yr⁻¹.

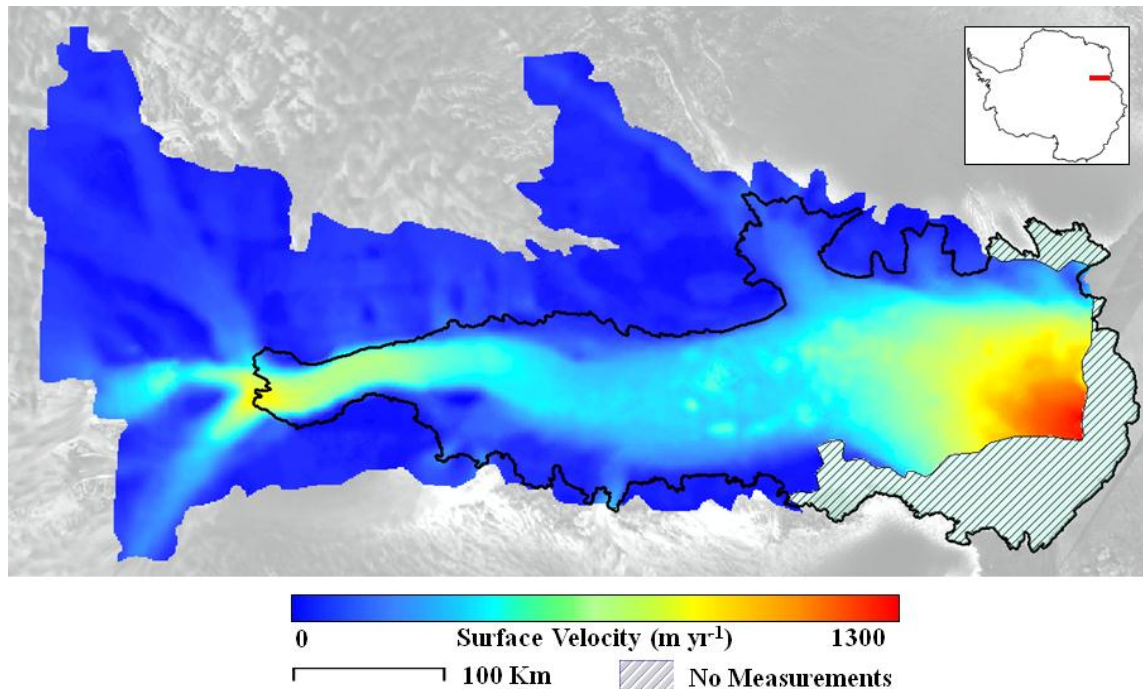


Figure 3.1 Surface velocity map (1988-1990) interpolated with the velocity fields derived by this study using the Ordinary Kriging method. The map is overlaid with Radarsat-1 image mosaic.

3.3.2 Surface Velocity Observations (1999-2004)

The LAS's surface velocity map for the time period of 1999-2004 is developed using the feature tracking method (Figure 3.2). The surface velocity vectors are derived and the distribution pattern of the surface velocities is found similar to the time interval of 1988-1990 expect some regions where no measurements are observed. Sub-pixel displacements of the full resolution images are with steps of fifteen pixels through fourteen ETM+ image pairs, yielding approximately 50,000 surface velocity vectors.

Furthermore, the quality control procedure is applied to reduce miscorrelated estimations. The observed surface velocities vary from 0 to 842 m yr⁻¹. Due the lack of cloud-free Landsat image pairs during 1999-2004, four substitute MODIS image pairs acquired during 2002-2004 are utilized to derive surface velocity measurements in the northern LAS, where around 30,000 surface velocity vectors are observed varying from 82 to 1107 m yr⁻¹.

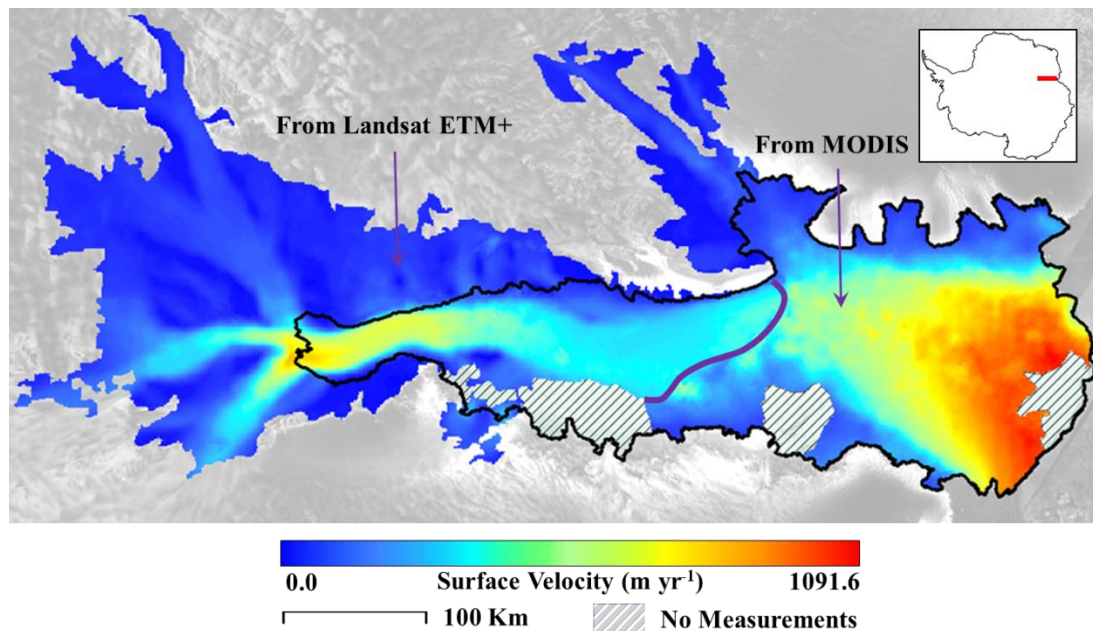


Figure 3.2 Surface velocity map (1999-2003) determined using feature tracking and interpolated with the derived velocity fields using the Ordinary Kriging method. The map is overlaid with the Radarsat-1 image mosaic.

3.3.3 Surface Velocity Observations (2007-2011)

Feature tracking method is applied to 134 SLC-off corrected Landsat ETM+ images to determine the LAS's surface velocity during 2007-2011 (Figure 3.3). Nine pairs of SLC-off ETM+ images are gap-filled using additional 116 ETM+ images. Sub-pixel displacements of the full resolution images are with steps of fifteen pixels through these nine ETM+ image pairs. Over 70,000 derived surface velocity vectors meet the quality control criteria. Insufficient ETM+ images and high inquiry of accurate Ground Control Points (GCPs) for image co-registration make MODIS images with a larger footprint suitable for the area the northern end of the LAS. Four MODIS images acquired during 2007-2009 are processed and analyzed. The approximately 10,000 surface velocity vectors determined from the MODIS images are integrated and the observed surface velocities vary from 0 to 995 m yr⁻¹.

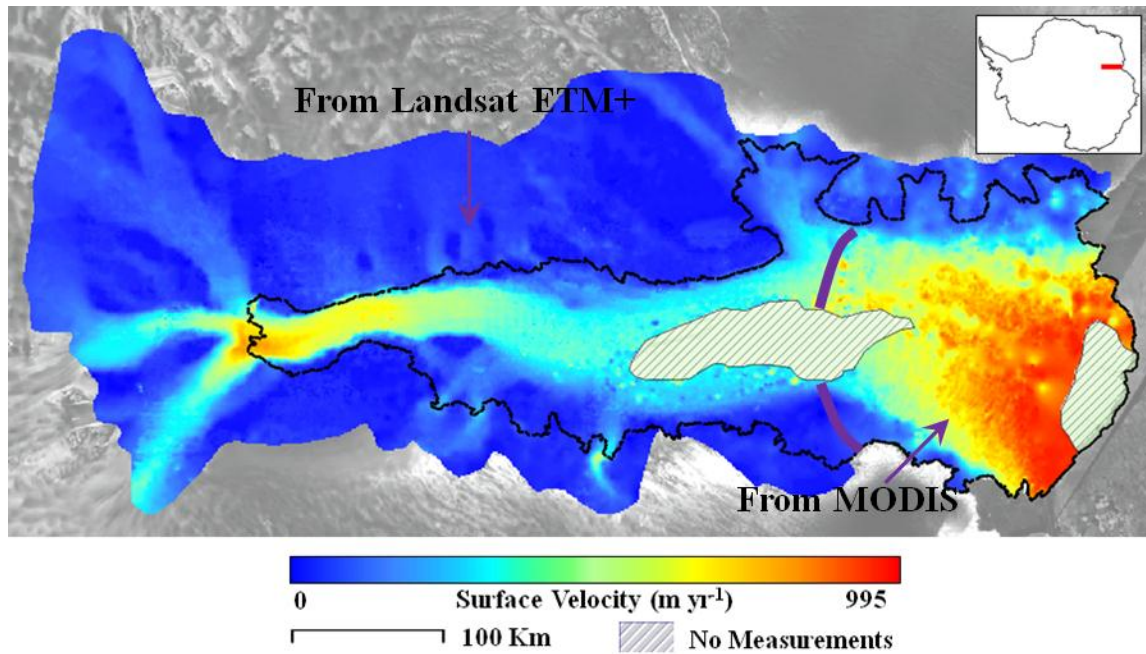


Figure 3.3 Surface velocity map (2007-2011) determined using feature tracking and interpolated with the derived velocity fields using the Ordinary Kriging method. The map is overlaid with Radarsat-1 image mosaic.

3.3.4 Combined Surface Velocity Observations of Three Time Intervals

Based on the developed surface velocities, three maps are presented to illustrate the surface velocities of the LAS for 1988-1990, 1999-2004, and 2007-2011, respectively (Fig 3.4). The three maps highlight very similar and consistent surface velocity spatial distribution patterns. For instance, in 1999-2004 (Fig 3.4b), the velocities can be separated into four groups, representing the glacial flow (southern end), the upper ice-shelf flow, the lower ice-shelf flow, and the tributary glacial flow (western and eastern sides).

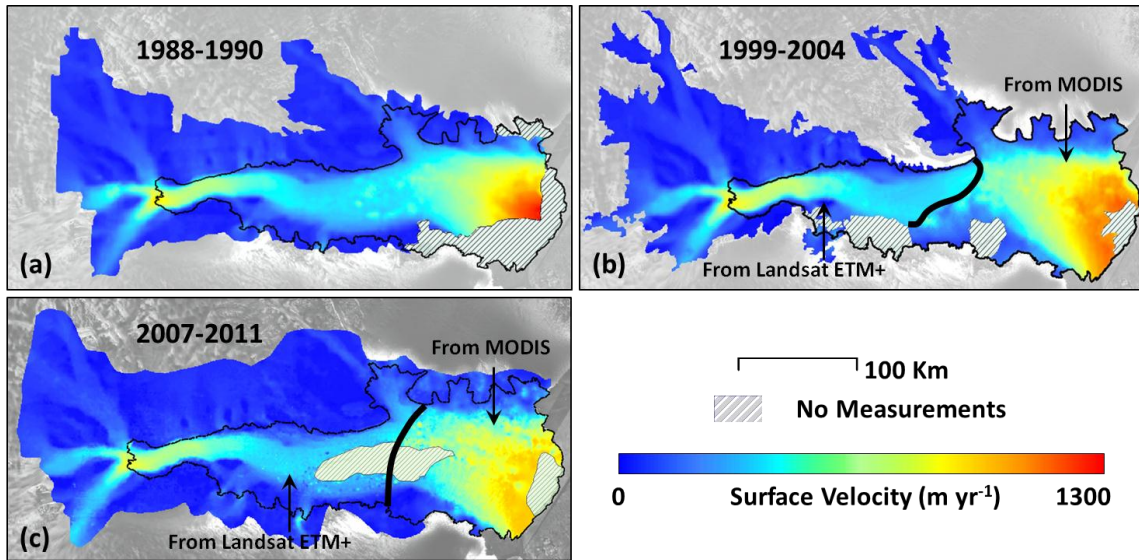


Figure 3.4 Surface velocity map of (a) 1988-1990, (b) 1999-2004, and (c) 2007-2011 for the LAS. All maps are overlaid over the Radarsat-1 image mosaic. The thick black solid line separates Landsat- and MODIS- derived surface velocities. The hatched areas indicate the missing Landsat/MODIS observations.

In Figure 3.4, the surface velocities particularly the lower ice-shelf flow perform a slowing trend. As is evident in the color-coded maps, the dominant high velocities over the vast fast moving lower ice-shelf region are decreasing. The highest velocity observed for the same areas using feature tracking also decreases from 1293 m yr^{-1} for 1988-1990, to 1034 m yr^{-1} for 1999-2004, and to 938 m yr^{-1} for 2007-2011. To illustrate the temporal variations, the surface velocity profiles of the major ice flow of the LAS were extracted and plotted for further analysis (refer to Section 3.5.3).

3.4 Comparisons of Feature Tracking and the Published Velocities

Currently, there are two popular InSAR velocity maps for the LAS that have been used in a number of studies. The first is the InSAR velocity mapping produced by the RAMP during 1997-2000 (Jezek, 2002). The other product is the most recently published Antarctic velocity mapping using multiple satellites InSAR data (Rignot *et al.*, 2011). Quantitative comparisons on feature tracking records of surface velocity are presented with the most recent InSAR velocity estimates produced by the NASA Making Earth Science Data Records for Use in Research Environments project (MEaSUREs, Rignot *et al.*, 2011b).

3.4.1 Comparison of Feature Tracking and the RAMP InSAR Velocities

A comparison was carried out between the surface velocity mapping for 1999-2004 and the contemporary RAMP InSAR measurements for 1997-2000 (Figure 3.4a) to examine the spatial distribution of velocity magnitudes. As both feature tracking and the InSAR observations are incomplete over the study area only the overlapping areas were considered for further comparison. Small velocity differences are found over most of the study area. Since the absolute velocity differences cluster in a small range (Figure 3.4b), it is not an ideal parameter to illustrate the spatial distribution of velocity differences of the LAS well.

In addition, the similar magnitude differences represent quite different percentages of the absolute magnitude for the high and low velocity portions of the LAS. Therefore, velocity differences, a percentage of the absolute difference between the

feature tracking and InSAR derived surface velocities divided with the feature tracking derived surface velocity, were calculated as illustrated in Figure 3.5c. Most of the high percentage differences are observed in the slow-flowing regions or along the ice shelf margins where velocity gradients are high. Lower percentage differences are observed in the fast-flowing regions, which is also consistent with the absolute magnitude difference map. High percentage differences represent large difference between the feature tracking and InSAR derived measurements, while percentage differences are inversely proportional to the surface velocity estimates. High percentage differences are often found in the stable regions, where the feature tracking derived surface velocities are usually subjective to the greatest uncertainty. In those regions, the uncertainty of the feature tracking measurements is usually one order greater than the InSAR measurements, which result in high percentage differences. Due the lack of features for correlation, featurelessness, high uncertainty is observed in the regions surrounding the Gillock Island.

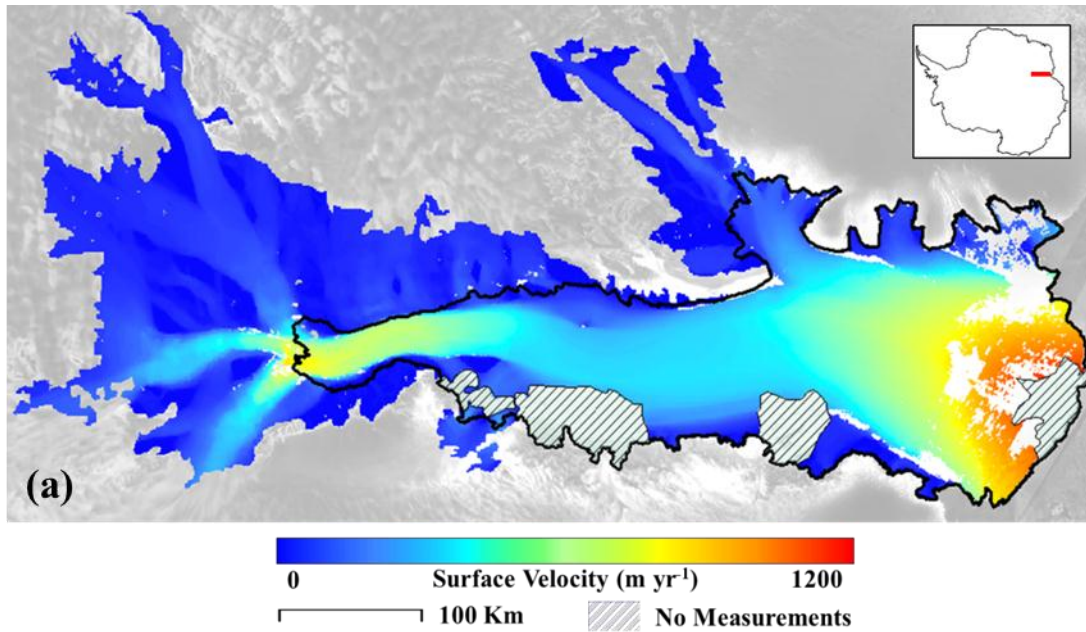


Figure 3.5 (a) Surface velocity map (1997-2000) created by RAMP using InSAR; (b) Magnitude of velocity difference between InSAR measurements and this study; (c) Velocity difference in percentage between InSAR measurements and this study. The maps are overlaid with Radarsat-1 image mosaic. The purple dashed line is a boundary separating Landsat- and MODIS- derived surface velocity measurements. White color represents the missing InSAR measurements. The inset map shows location of the LAS in Antarctica.

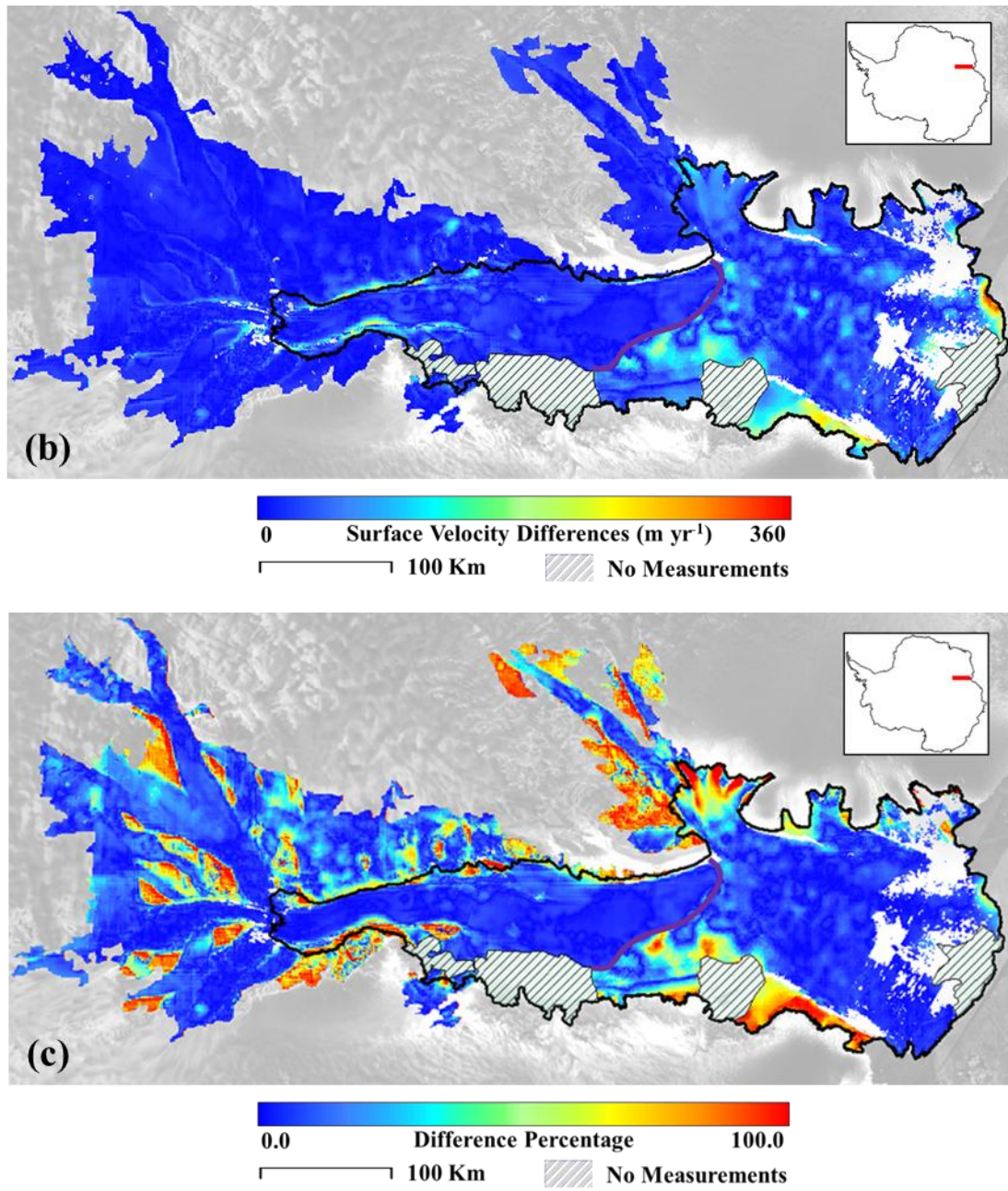


Figure 3.5 continued.

The absolute velocity differences between this study and InSAR measurements are plotted for the Landsat- and MODIS- derived velocities respectively (Figure 3.6a). Overall, there appears to be a good agreement between this study and InSAR measurements for the LAS. Most of the absolute velocity differences between this study and RAMP InSAR measurements are on greater than 100 m yr^{-1} . Approximately 60% of the absolute velocity differences less than 50 m yr^{-1} come from the Landsat derived velocities, while another 25% is contributed by the MODIS derived velocities. Only 1% of absolute velocity differences are higher than 250 m yr^{-1} . The Figure 3.6b makes the further effort to illustrate the velocity differences, since percentage difference appears to be a better indicator for interpreting both small and large differences in detail. Over 70% of the percentage velocity differences between this study and the InSAR measurements are less than 20%. Besides, there are only slight percentage differences (1-3%) come from Landsat and MODIS. Considering the estimates accuracy which has been discussed in Chapter II, it is confident to conclude that Landsat derived surface velocities appear more consistent with the InSAR measurements, compared with the MODIS derived surface velocities. High percentage velocity differences of the Landsat derived velocities are mostly caused by the uncertainty measurements in the stable regions, which is also illustrated in Figure 3.5c.

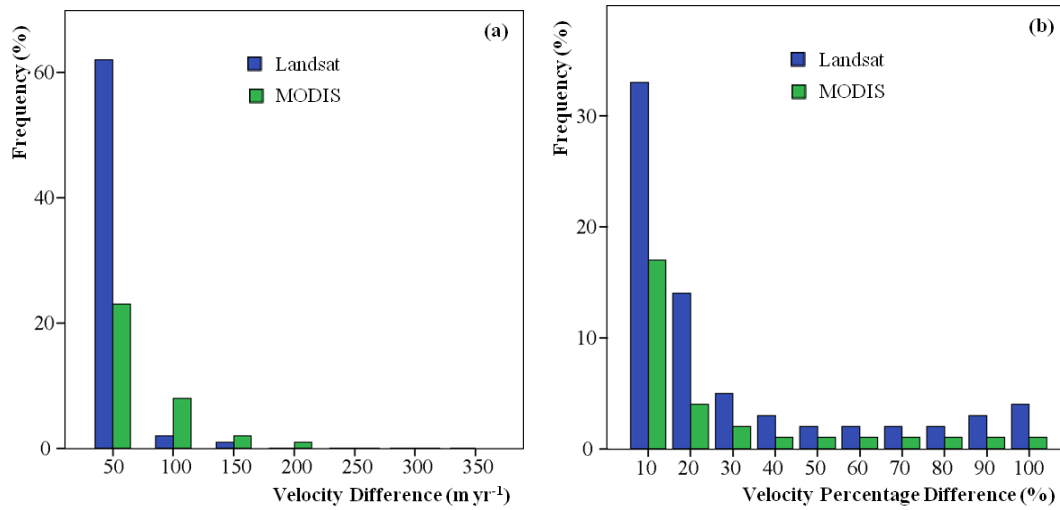


Figure 3.6 Frequency distribution of (a) absolute velocity differences and (b) percentage velocity differences between RAMP InSAR measurements and feature tracking with Landsat and MODIS.

3.4.2 Comparison of Feature Tracking and the Field Measurements

King (2002) published forty-six GPS velocity measurements made during 1990-1999 (Table 3.2). These GPS measurements are separated into two groups based on temporal coverage (1988-1990 and 1999-2004) and compared with the remote sensing-derived surface velocity estimates made within 2 km during the same time period. The feature tracking and the GPS measurements are assumed independent samples and normally distributed. A t-test at the 95% confidence intervals is considered appropriate and is conducted on the Landsat-derived and MODIS-derived surface velocity measurements to determine whether there is a significant difference between two group means (Levesque, 2007). PASW Statistics 18 is used to implement the calculations.

For the time interval of 1988-1990, the average absolute velocity differences between the feature tracking and GPS measurements is 29.8 m yr^{-1} (10.6%). The feature tracking derived measurements are plotted as solid light gray triangle in Figure 3.7a, while the GPS measurements are presented as solid black dots. The feature tracking derived measurements mostly distribute within the 95% confidence intervals, except a few sites (e.g. G242, GA02, GA08, GA23, and GA72) (Figure 3.6a). As illustrated in Figure 3.7b, the absolute velocity differences between the above two measurement groups appear to vary around the mean value (29.8 m yr^{-1}), while the percentage velocity differences vary around the corresponding mean (10.6%). To investigate if there is any significant correlation between the two types of velocity differences and the velocity magnitudes, Figure 3.7c is created. Two types of velocity differences randomly distribute across the plotting and there is no significant correlation found between the velocity differences and the velocity magnitudes.

The same analysis has been applied to the time interval of 1999-2004, while the average absolute velocity differences between the feature tracking and GPS measurements is 11.6 m yr^{-1} (1.7%). Excluding the outliers in a few sites (e.g. A130, A33_, and G2E1), most of the feature tracking derived measurements distribute within the 95% confidence intervals (Figure 3.7d). As illustrated in Figure 3.7e, the absolute velocity differences between the above two measurement groups appear to vary around the mean value (11.6 m yr^{-1}) and the percentage velocity differences vary around the corresponding mean (1.7%), which is better than the time interval of 1988-1990. No

significant correlation is observed by plotting the velocity differences and the velocity magnitudes for the time interval of 1999-2004 (Figure 3.7f).

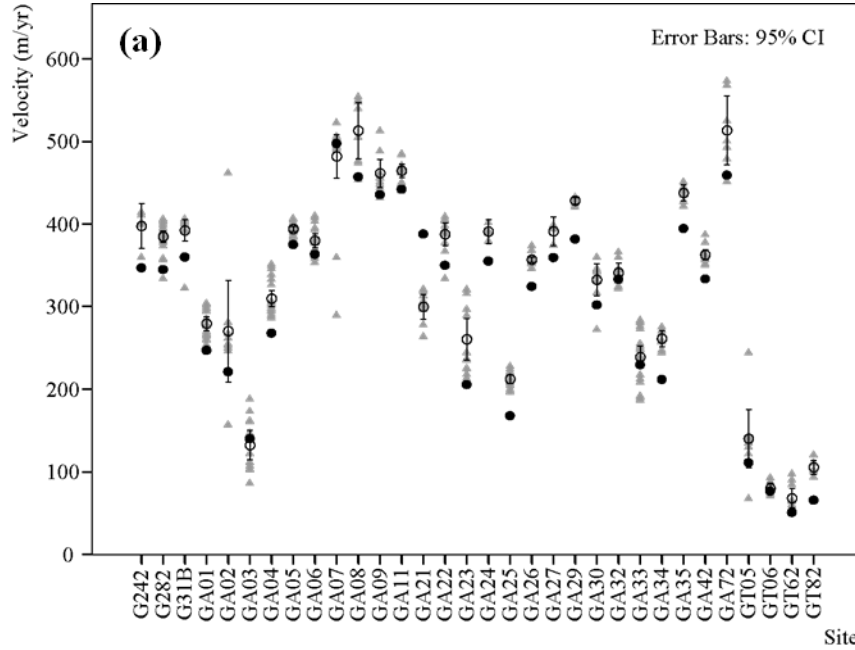


Figure 3.7 (a) The feature tracking derived velocity measurements (solid light gray triangle) during 1988-1990 within 2 km of the GPS velocity fields (solid black dots); (b) The absolute differences in m yr^{-1} and percentage differences for all the GPS velocity fields collected during 1990-1991; (c) Plot of surface velocity magnitude and absolute differences and percentage differences for the time period of 1988-1990; (d) The feature tracking-derived velocity measurements (solid light gray triangle) during 1999-2004 within 2 km of the GPS velocity fields (solid black dot); (e) The absolute differences in m yr^{-1} and percentage differences for all the GPS velocity fields collected in 1999; (f) Plot of surface velocity magnitude and absolute differences and percentage differences for the time period of 1999-2004.

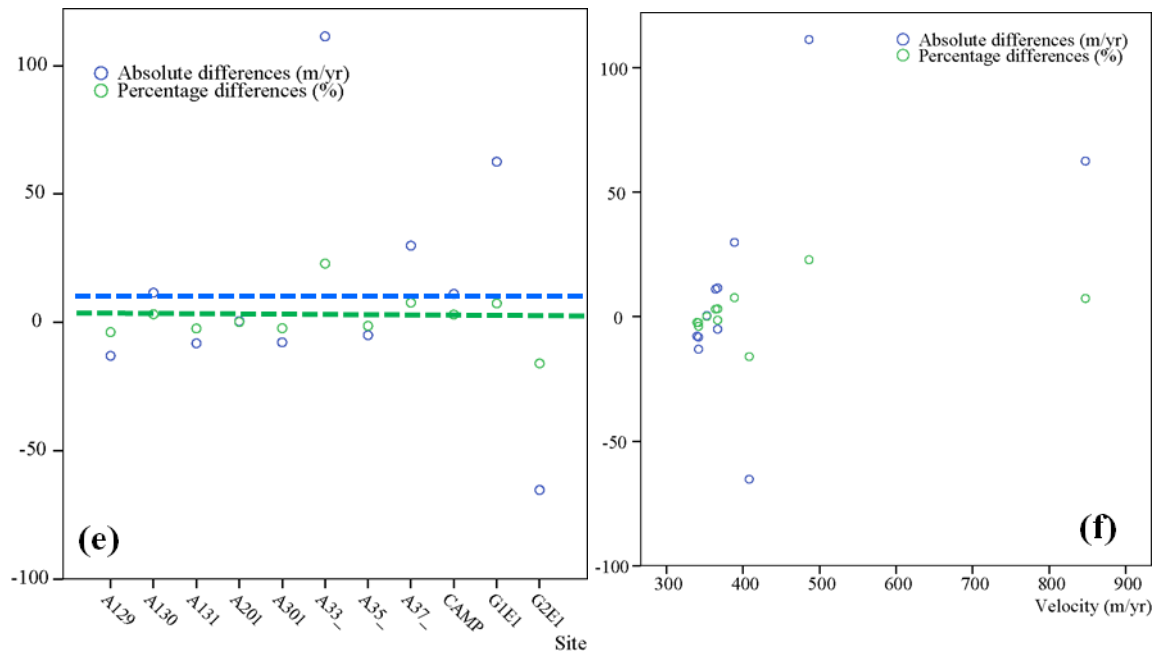


Figure 3.7 continued.

3.5 Advanced Analyses

The surface velocity maps for multiple time periods are analyzed in three different aspects, which involve (1) congruency of surface velocities derived from Landsat and MODIS difference data sources, (2) analysis of fast-moving regions, and (3) analysis of surface velocity variations.

3.5.1 Congruency Test

For the time interval of 1999-2004, the surface velocity measurements consist of the MODIS-derived velocities for the Amery Ice Shelf front region and the Landsat-derived velocities for rest regions. A congruency test is conducted to check the consistency of surface velocities derived from different datasets for the same moving ice surface. In the overlapping areas, four spatially-distributed sites with a 2.5 km radius were used to compare surface velocity measurements from Landsat and MODIS. Four hundred comparisons are conducted between the Landsat-derived velocity measurements and the closest MODIS-derived measurements falling within each 1 km radius (Figure 3.8). For the 400 comparisons, the maximum difference in velocity was 35 yr^{-1} while 35° was the upper limit of absolute directional differences. The average magnitude difference was -4.6 m yr^{-1} and average direction difference was 7.5° . Therefore, it appears that the MODIS-derived surface velocities are consistent with the Landsat-derived surface velocities over distances within 1 km.

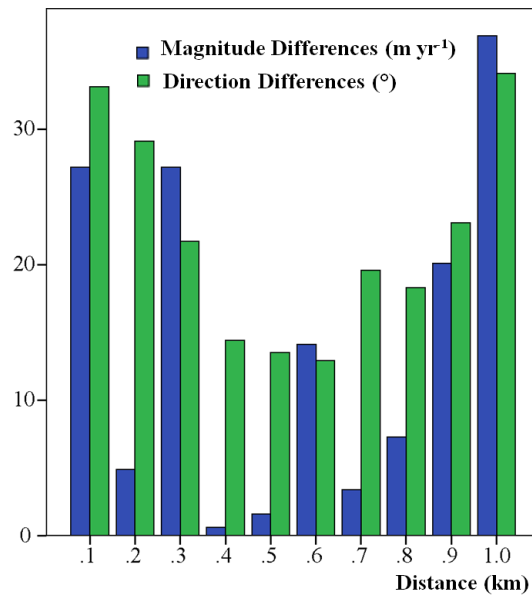


Figure 3.8 The comparisons between the Landsat-derived velocity magnitude and direction and the closest MODIS-derived velocity measurements per 100m within a 1 km radius.

3.5.2 Delineation of Fast-moving Areas, Flowlines, and Imaginary Flux gates

Under a steady state, the volume of ice is assumed to remain constant between two adjacent flowlines for the full length (Hooke, 2005). Assuming ice is incompressible, the highest velocities are where the flowlines are closest together. The centerlines can be identified by delineating the highest surface velocities. In this study, the centerlines are delineated from a group of intersections of flowlines with polygonal velocity contours.

Several velocity profiles are delineated along the corresponding centerlines for further comparison. The spatial extent and velocity gradient information of each individual glacier is determined using velocity maps whose velocities are segmented into 50 m yr^{-1} intervals for the time periods of 1988-1990 (Figure 3.1), 1999-2004 (Figure 3.2), and 2007-2011 (Figure 3.3). The fast-moving portions of the three major tributary glaciers of the LAS have been separated from the background sheet flow using 150 m yr^{-1} velocity.

The identified fast-moving areas of the Lambert Glacial Basin, Mellor Glacial Basin, and the Fisher Glacial Basin cover four time intervals (Figure 3.9a). This study contributes to the time intervals of 1988-1990, 1999-2004, and 2007-2011, while the RAMP InSAR velocities contribute the fourth time interval of 1997-2000. A clear decreasing trend is observed from late 1980s to 2011s by plotting the fast-moving areas for each individual glacial basin. The fast-moving areas do not uniformly distribute among these three large glacial basins. The Lambert Glacial Basin and the Mellor Glacial Basin have similar level of fast-moving areas during the four time intervals from late 1980s to 2011s. The fast-moving area of the Fisher Glacial Basin is nearly $1.0 \times 10^6 \text{ km}^2$ smaller than any of the other two glacial basins, the Lambert Glacial Basin and the Mellor Glacial Basin in late 1980s. Between the Fisher Glacial Basin and any of the other two glacial basins, these differences of fast-moving areas keep narrowing down to approximately $0.8 \times 10^6 \text{ km}^2$. The details of fast-moving areas discussed above are provided in Table 3.3.

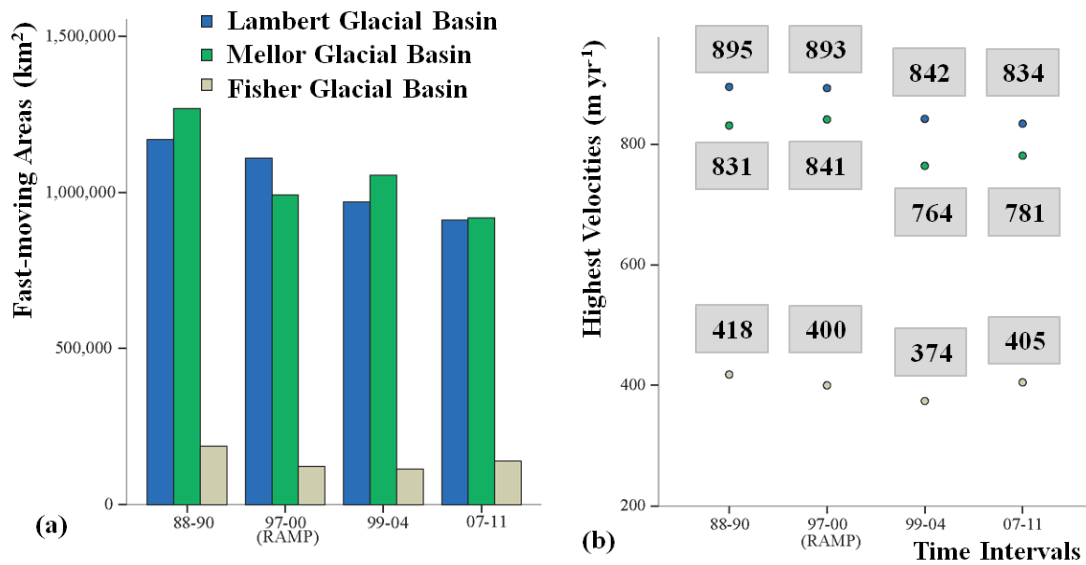


Figure 3.9 (a) Fast-moving areas and (b) highest velocities of the three major glaciers derived by feature tracking for the time intervals of 1988-1990, 1999-2004, and 2009-2011 and derived by InSAR for the time interval of 1997-2000 (RAMP).

The highest velocities of the Lambert Glacial Basin and the Mellor Glacial Basin are observed decreasing (Figure 3.8b), covering the same four time intervals as in Figure 3.8a. Three time intervals come from this study and the fourth comes from RAMP InSAR velocities. The highest velocities of the Lambert Glacial Basin and the Mellor Glacial Basin appear consistently variation trends, which include the drop from late 1990s to 2000s and two rises from late 1980s to 1990s and from late 1990s to 2000s. Due to coving smaller fast-moving grounded ice surface compared to the other two glacial basins, the highest velocities of the Fisher Glacial Basin appear a continuously

decreasing trend from late 1980s to 2000s and then follow with a slight increasing from 374 to 405 m yr⁻¹.

Table 3.3 Comparison of the spatial extents of the fast-moving areas of the three major glacial basins between this study and the RAMP measurements.

Time Intervals	<i>Fast-moving Extent (km²)</i>		
	<i>Lambert</i>	<i>Mellor</i>	<i>Fisher</i>
1988-1990	1,169,936	1,267,680	186,434
1997-2000	1,109,060	991,560	122,104
1999-2004	970,151	1,054,785	112,982
2007-2011	910,585	918,019	139,150

Note: Fast-moving Extent (>150 m yr⁻¹); * driven from RAMP

The spatial extent and velocity contour information of fast-moving areas of these three glacial has been determined by this study for the three time intervals of 1988-1990, 1999-2004, and 2007-2011. The comparisons are made to show the differences of the fast-moving areas identified by this study (1988-1990, 1999-2004, and 2007-2011) and the RAMP measurements (1997-2000).

For the time interval of 1988-1990, the spatial extent of the surface velocities are color-coded (Figure 3.10), while the surface velocity contours are clearly presented. The

centerline from the interior grounded ice to the Amery Ice Shelf are presented as a solid black line for each glacial basins, pointing the direction through which the ice surface velocities increase the fastest.

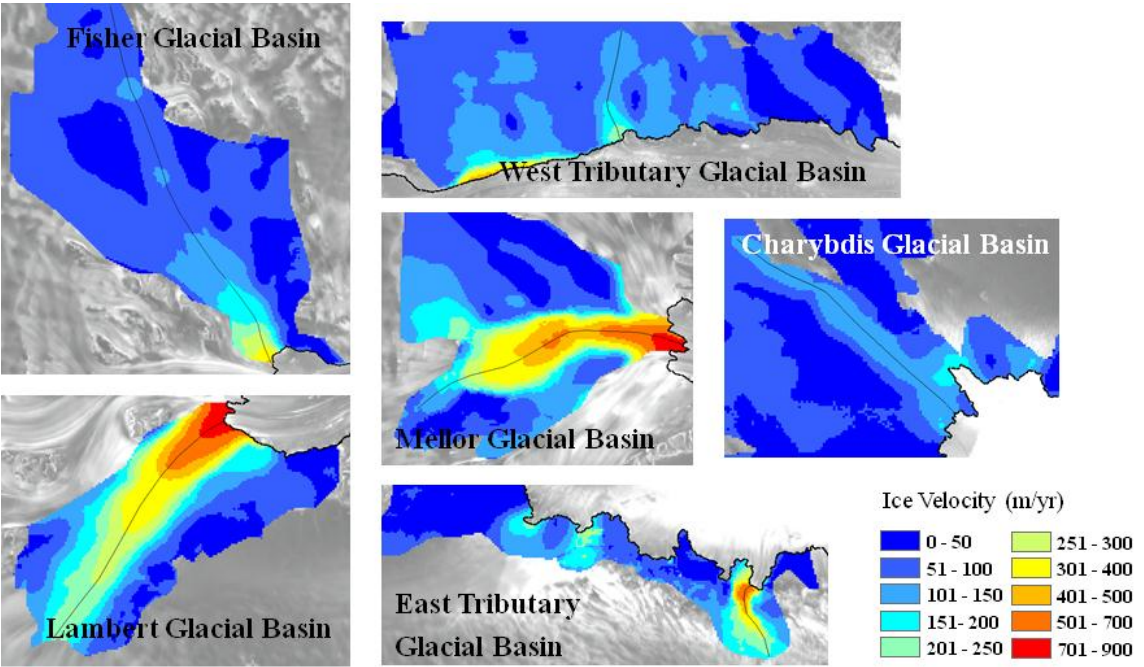


Figure 3.10 Flow contour features of 1988-1990 for the Lambert Glacier, the Mellor Glacier, the Fisher Glacier, the West Tributary Glacier, the Charybdis Glacier, and the East Tributary Glacier

The spatial extent of the surface velocities of 1999-2001 (Figure 3.11) are color-coded with the same break values as Figure 3.9. The centerline is placed upon the same

geographic locations intersecting the clearly presented surface velocity contours. A slight shrinkage of fast-moving regions is observed from late 1990s to late 2000s.

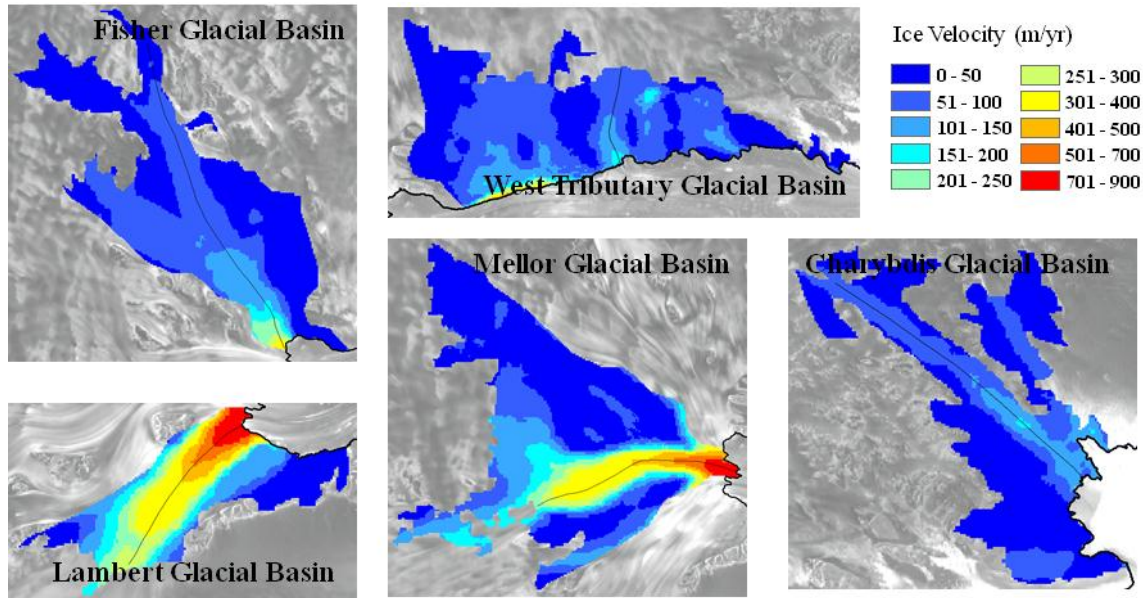


Figure 3.11 Flow contour features of 1999-2004 for the Lambert Glacier, the Mellor Glacier, the Fisher Glacier, the West Tributary Glacier, and the Charybdis Glacier.

The spatial extent and velocity contours of 2007-2011 are presented in Figure 3.12. There is no significant change observed in the spatial distribution pattern of surface velocities of 2007-2011, which is alike to the observations of the other two time periods.

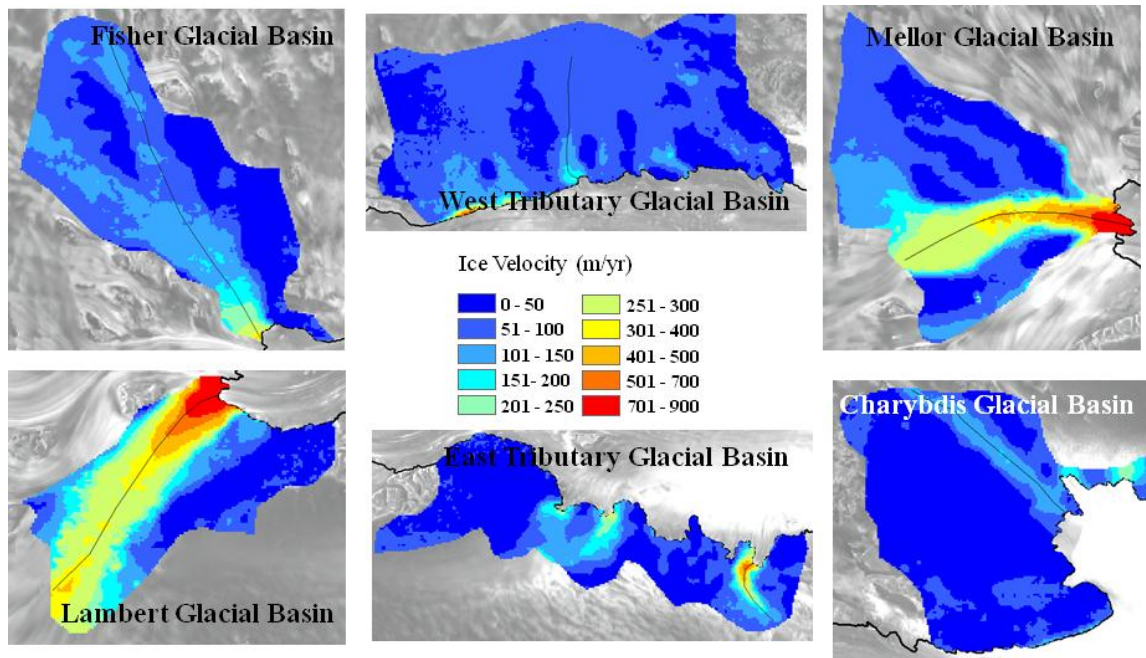


Figure 3.12 Flow contour features of 2007-2011 for the Lambert Glacier, the Mellor Glacier, the Fisher Glacier, the West Tributary Glacier, the East Tributary Glacier, and the Charybdis Glacier.

3.5.3 Variation Analysis of Surface Velocity

The centerlines with certain width have been placed in the Amery Ice Shelf, the Lambert Glacier, the Mellor Glacier, and the Fisher Glacier (Figure 3.13). The surface velocities varying between the high and low values are presented in the area charts (Figure 3.14-3.17) for the three time intervals of 1988-1990, 1999-2004, and 2007-2011. Each centerline of the three glaciers is created starting from the interior grounded ice surface and ending at the grounding line, which is the boundary between the grounded ice surface and the Amery Ice Shelf. The centerline of the Amery Ice Shelf is created

starting from the grounding line to the seaward ice shelf front. The mean values are presented as solid black lines and the high values usually locate close to the center of the centerline in the surface velocity maps.

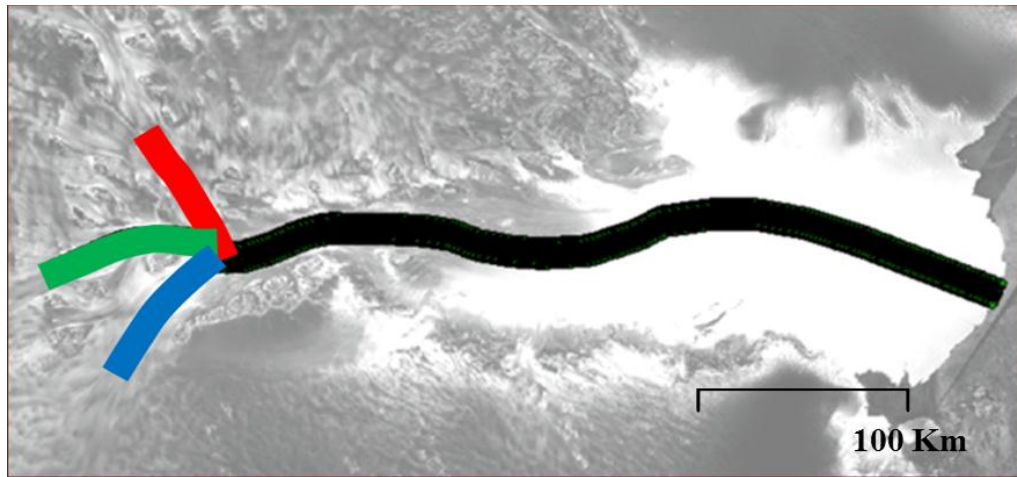


Figure 3.13 Location of the centerlines for the Amery Ice Shelf (Black), the Lambert Glacier (Blue), the Mellor Glacier (Green), and the Fisher Glacier (Red).

The centerline of the Amery Ice Shelf is over 500 km having the width of 18 km. The velocity profile along the centerline of the Amery Ice Shelf appears a stable spatial variation pattern (Figure 3.14). The velocities begin at approximately 800 m yr^{-1} from the grounding line, follow a velocity decreasing to around 350 m yr^{-1} at the central of the Amery Ice Shelf, and speed up again seaward to the ice shelf front over 1000 m yr^{-1} .

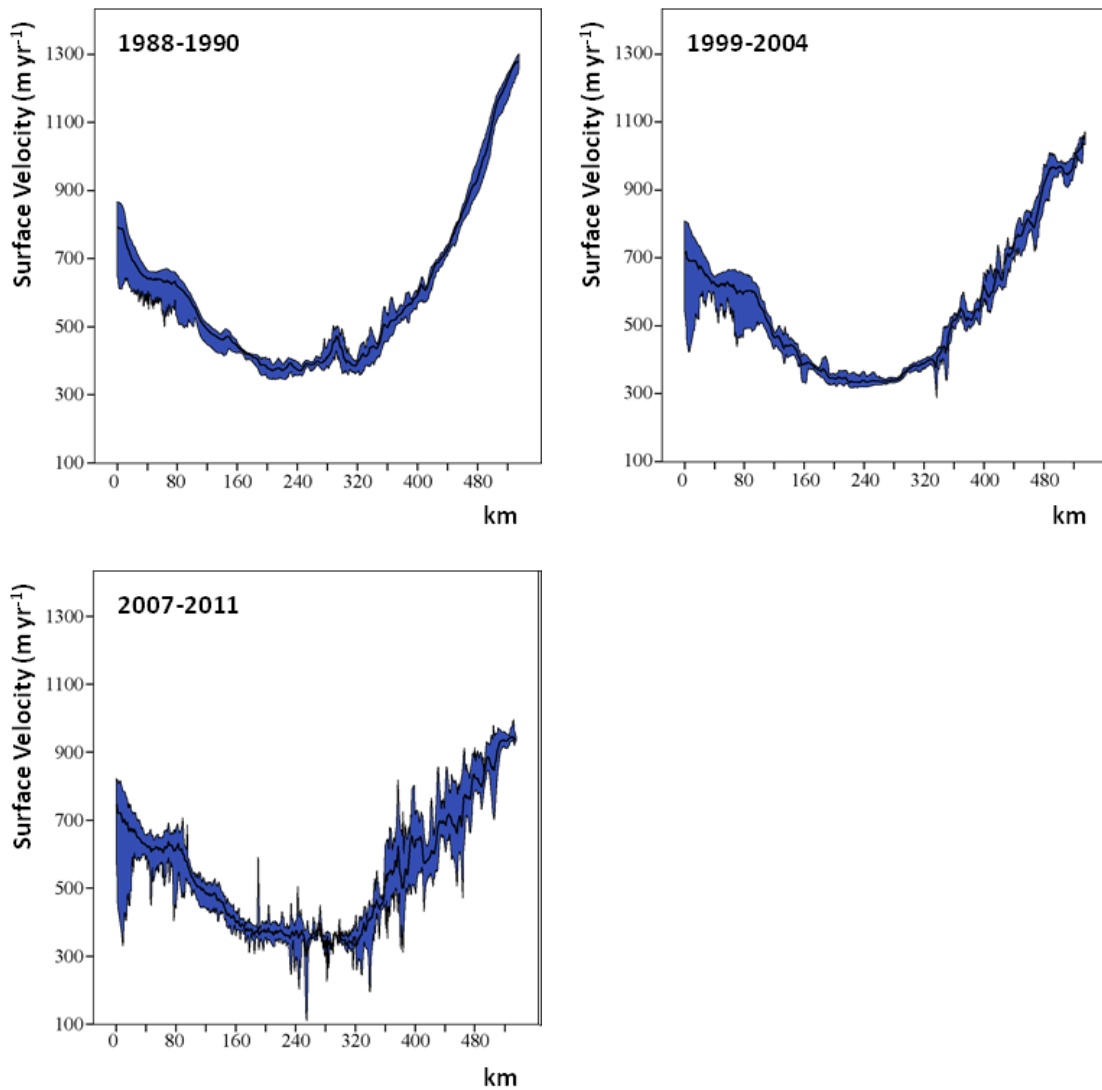


Figure 3.14 Surface velocity profiles for the Amery Ice Shelf in 1988-1990, 1999-2004, and 2007-2011.

The centerline of the Lambert Glacier is approximately 110 km having the width of 10 km. The velocity profile along the centerline of the Lambert Glacier appears differently than the Amery Ice Shelf's velocity profile. The velocities begin at

approximately 250 m yr^{-1} and keep speeding up to around 800 m yr^{-1} when approaching the grounding line (Figure 3.15).

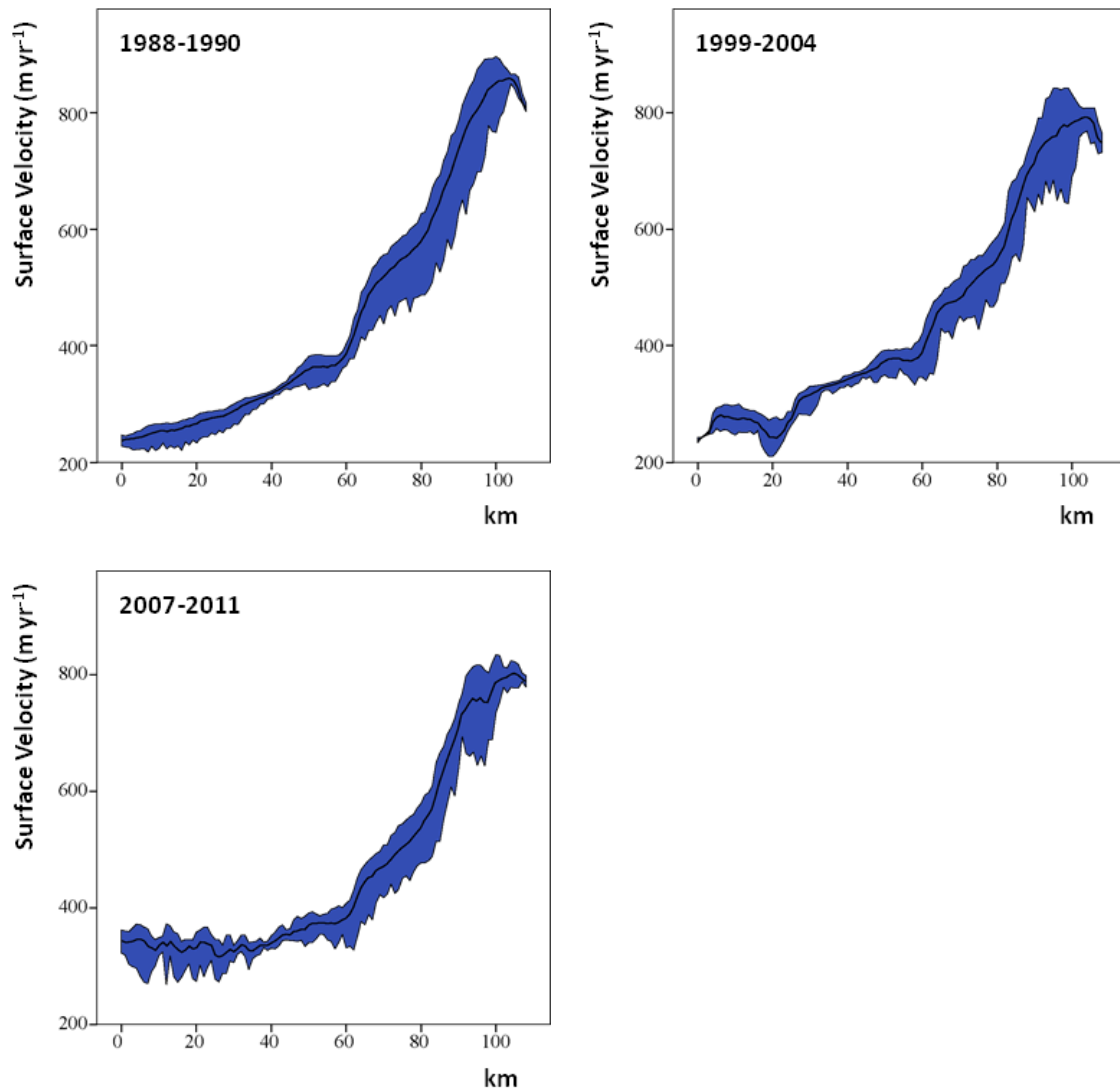


Figure 3.15 Surface velocity profiles for the Lambert Glacier for 1988-1990, 1999-2004, and 2007-2011.

The centerline of the Lambert Glacier is approximately 130 km having the width of 10 km. Due to the spatial size of Mellor Glacier close to the Lambert Glacier, the velocity profile along the centerline of the Mellor Glacier appears similar to the Lambert Glacier's velocity profile. The velocities begin at approximately 200 m yr^{-1} and keep speeding up to around 800 m yr^{-1} when approaching the grounding line (Figure 3.16). Nearby the location of 55 km where is close the middle of the Lambert Glacier, there was a short slowing down between two speeding during the time interval of 1988-1990. This pattern is not observed during the other two time intervals, when the surface velocities increase slowly from the beginning until the 88 km location.

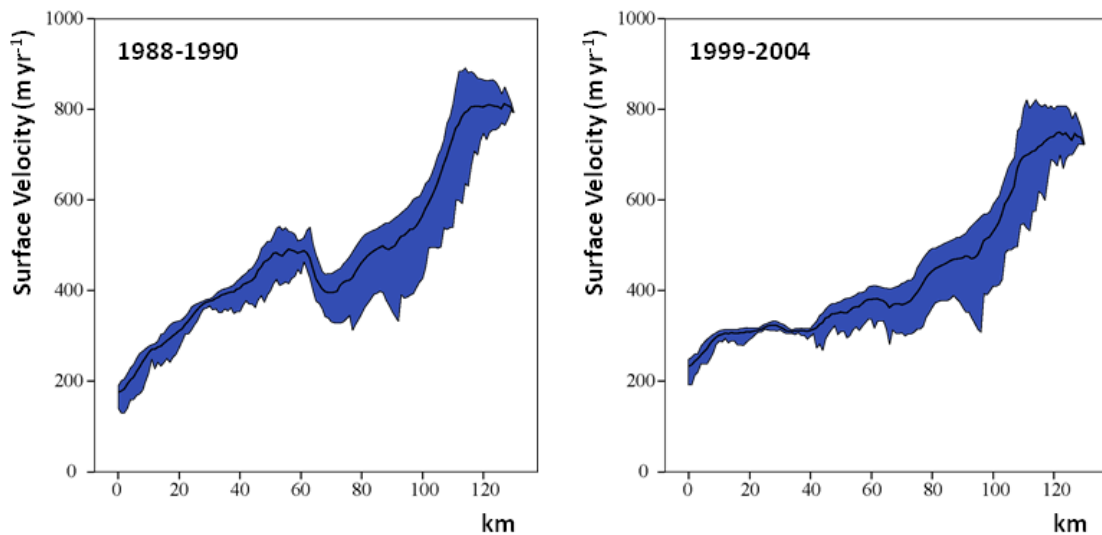


Figure 3.16 Surface velocity profiles for the Mellor Glacier between 1988-1990, 1999-2004, and 2007-2011.

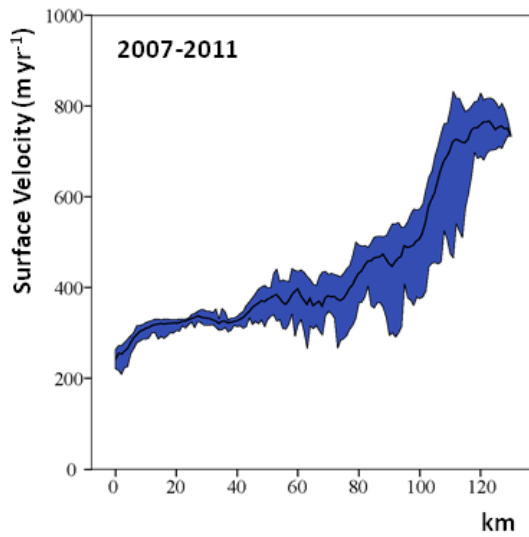


Figure 3.16 continued.

The centerline of the Lambert Glacier is approximately 100 km having the width of 10 km. The fast-moving areas of the Fisher Glacier is much smaller than the other two glaciers, which is reflected by that the velocities increase very slowly along the first 70 km of centerline. Then the velocities speed up to around 800 m yr⁻¹ when approaching the grounding line (Figure 3.17).

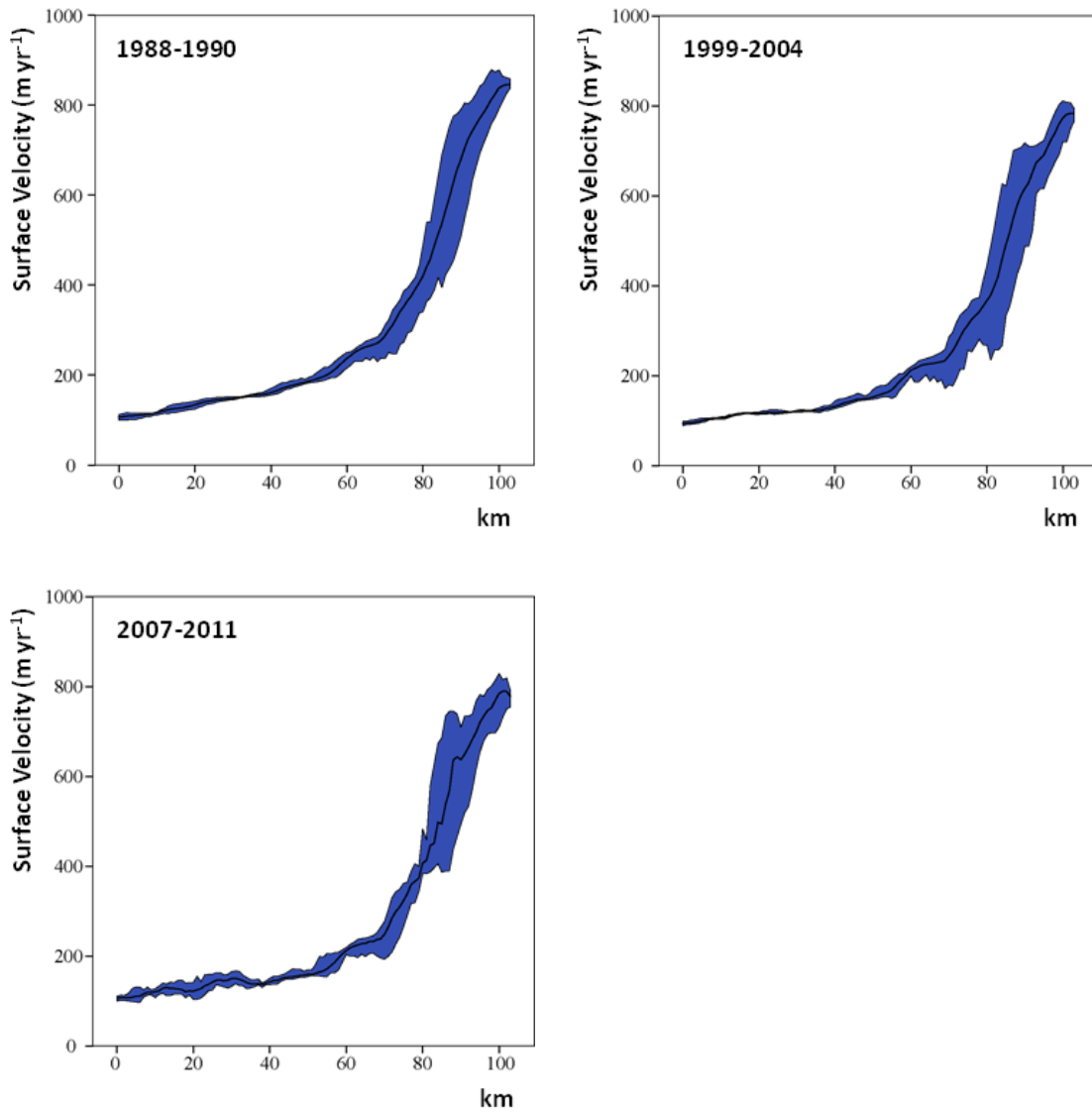


Figure 3.17 Surface velocity profiles for the Fisher Glacier during 1988-1990, 1999-2004, and 2007-2011.

By plotting the surface velocity profiles, the distribution pattern of the velocity centerline of the Amery Ice Shelf appear stable during the three time intervals (Figure

3.18), except a slight decrease at the end of the centerline, which is also considered as the seaward front of the Amery Ice Shelf. The centerline of the Amery Ice Shelf are observed ending at 1279 m yr^{-1} , 1053 m yr^{-1} , and 938 m yr^{-1} for the same location for the three time intervals of 1988-1990, 1999-2004, and 2007-2011 respectively. The slowing rate enables to be estimated by dividing the velocity differences with the temporal differences. It is assumed that the temporal difference between the above three time intervals is approximately a decade. Hence, the seaward front of the Amery Ice Shelf has been slowing 22.6 m yr^{-1} per year from late 1980s to 1990s and slowing 11.5 m yr^{-1} per year from late 1990s to 2000s.

A consistent slight decrease from the late 1980s to 1990s has been observed among all three glaciers at the end of the centerlines, where is nearby the grounding line. The velocities of the three glaciers at the end of the centerlines appear an approximately decreasing of 30 m yr^{-1} . During the same time period, the first 55 km of the Lambert Glacier's centerline velocity appears slight increasing, while an obvious decreasing is observed at the first 55 km of the Mellor Glacier's. There is no significant change observed in the velocity centerlines of the Lambert Glacier, the Mellor Glacier, and the Fisher Glacier from late 1990s to 2000s, exclusive of the velocity keeps increasing at the beginning 55 km of the Lambert Glacier.

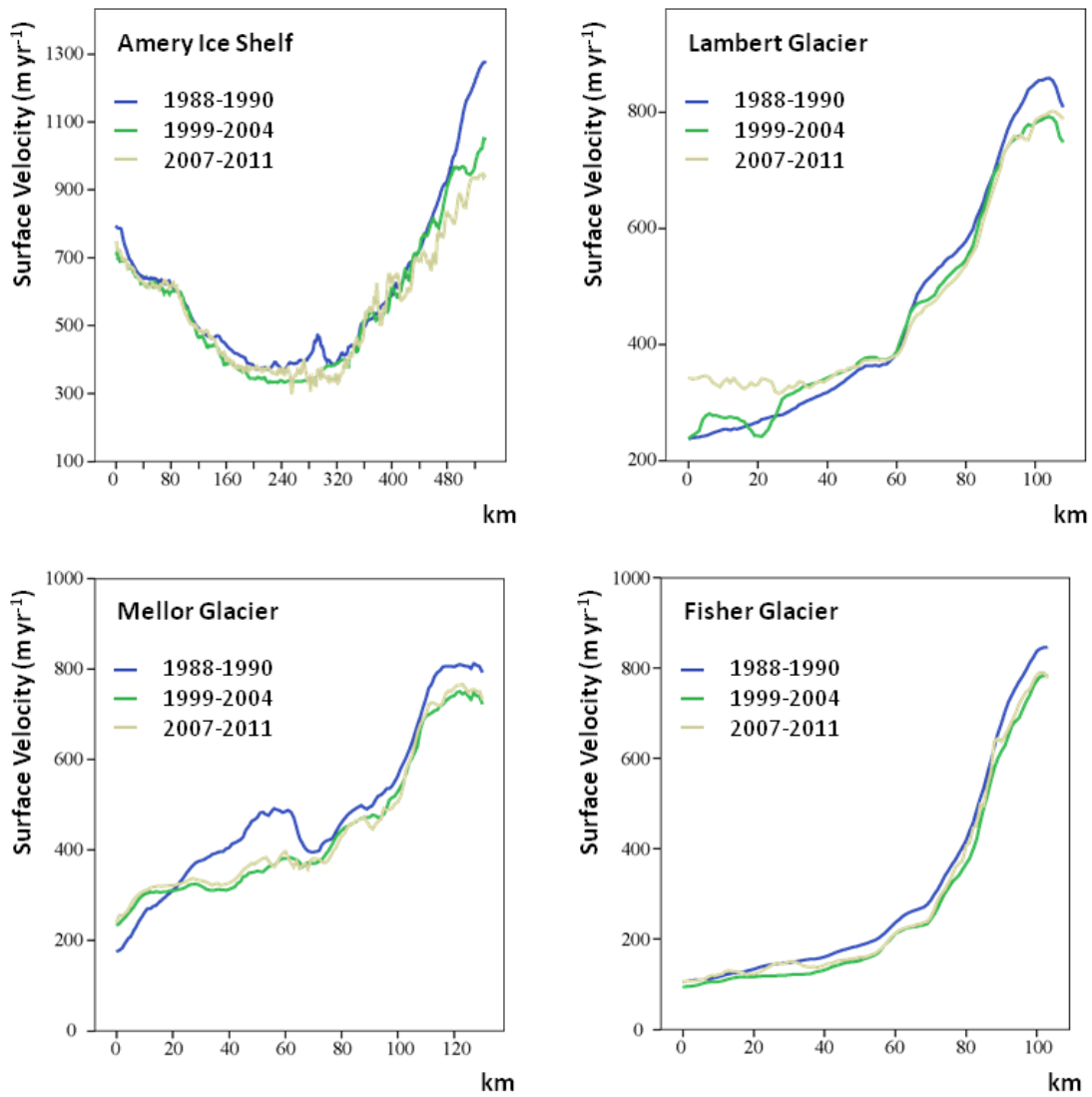


Figure 3.18 Surface velocity profiles of the Amery Ice Shelf, and three major glaciers in 1988-1990, 1999-2004, and 2007-2011.

The velocity variations along the centerline of major tributary glaciers (Figure 3.13) are determined by subtracting the surface velocities from the later time period from the previous measurements and plotting the differences. Surface velocity differences

above 0 indicate a velocity increase, while those below 0 a velocity decrease. It is noted in Figure 3.19 that most of the three examined regions experienced a velocity increase from 1988/1990 to 1999/2004 and velocity decrease from 1999/2004 to 2007/2011, except where the three glaciers flow into the Amery Ice Shelf. The velocity differences where three glaciers reside vary from approximately -50 m yr^{-1} from 1988/1990 to 1999/2004 and 50 m yr^{-1} from 1999/2004 to 2007/2011. The velocities of the Amery Ice Shelf front have kept decreasing from 1988/1990 to 2007/2011.

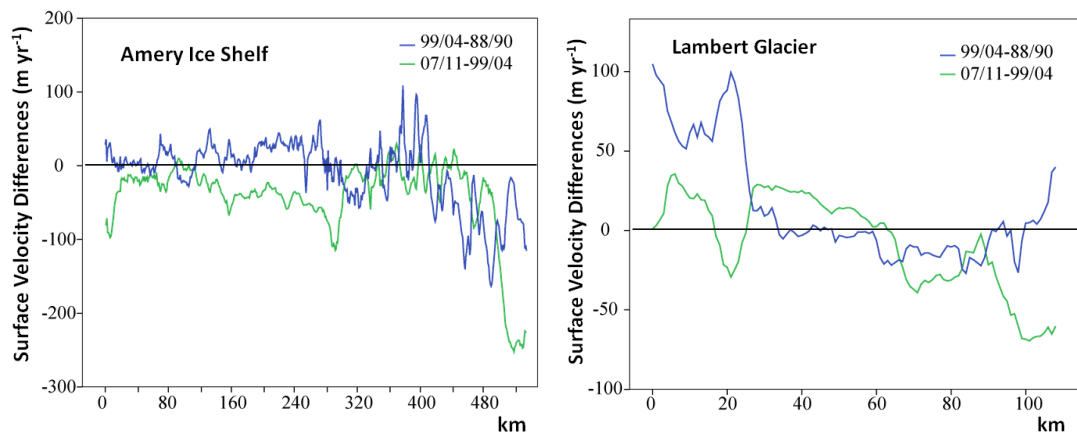


Figure 3.19 Surface velocity variations extracted from the four surface velocity profiles between two time intervals of 99/04-88/90 and 07/11-99/04. The dashed line and solid line represent the linear regression trend for 99/04-88/90 and 07/11-99/04 respectively.

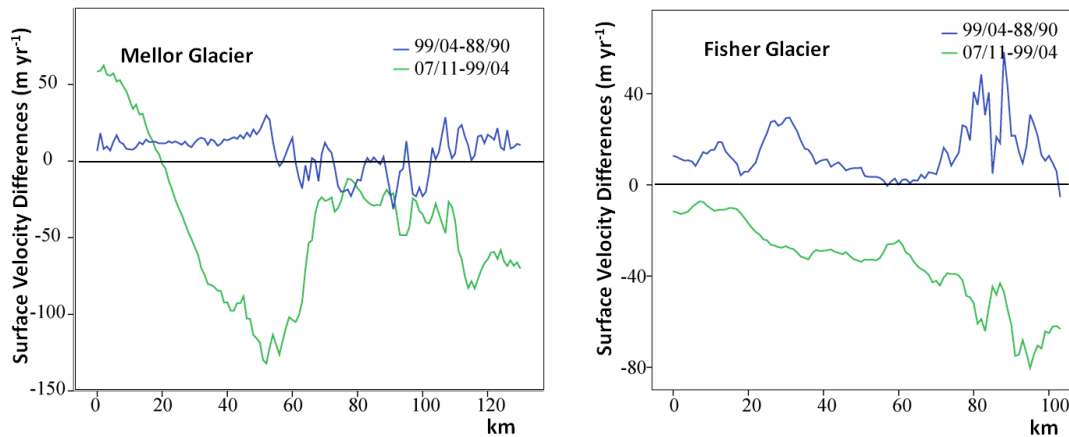


Figure 3.19 continued.

3.5.4 Motion Analysis of the Amery Ice Shelf Front

The Antarctic ice shelves mainly lose mass via iceberg calving from the ice shelf front or basal melting beneath (Jacobs *et al.*, 1992; Rignot & Thomas, 2002). The last major calving event occurred in late 1963 or early 1964. At that time, a massive iceberg roughly 140 by 70 km² was released from the ice shelf front (Budd, 1966). After this calving event, the Amery Ice Shelf is believed to calve again in 60-70 years later (Fricker *et al.*, 2002b). The position of the Amery Ice Shelf front was surveyed by various methods between 1936 and 1968, including airborne, shipborne, and terrestrial methods (Robertson, 1992). The current gradual advance of the Amery Ice Shelf suggests a calving cycle of approximately 40-70 years (Budd, 1966; Fricker *et al.*, 2002b).

Remote sensing becomes common place to monitor iceberg calving events from the Antarctic ice shelves. Many large iceberg calving events in Antarctica have been

studied (see Fricker *et al.*, 2002b; Massom, 2003; Remy *et al.*, 2008), as an increase in such types of events could be an indicator of climate change. The extent of changes of floating ice shelves may limit their ability to buttress the flow of grounded tributary glaciers (Dupont & Alley, 2005). It is found that accelerated glacier flow resulted from a reduction in buttressing of the adjacent ice (Rignot *et al.*, 2004; Goldberg *et al.*, 2009).

Motion of the same surface feature at the ice shelf front is a good indicator for monitoring the extent changes of the Amery Ice Shelf. The previous measurements (Zwally *et al.*, 2002) suggest a mean motion of $1.03 \pm 0.04 \text{ km yr}^{-1}$ during 1978-1994. Fricker *et al.* (2002) updated the estimation for the central part to 1.3 km yr^{-1} for 1997.

For the purpose of determining the rates of advance, the Amery Ice Shelf frontal positions between 1972 and 2009 were surveyed based on satellite images. Seven cross sections are placed in the western (L1 and L15), central (L2, L25, and L3), and eastern sides (L4 and L5) respectively along each individual ice shelf front position (Figure 3.19a). The ice shelf front motion for each cross section point is estimated as the ratio between the advancing distance of the ice surface and the temporal differences. The entire Amery Ice Shelf has been advancing since 1972, but the western, central, and eastern sides perform differently (Figure 3.19b). The advancing velocities of both western and eastern sides have been increasing by 2007, while the central part's velocities remain above 1000 m yr^{-1} . After that, the advancing velocities of L1 and L15 (western side) decreased 175 m yr^{-1} and 126 m yr^{-1} respectively. Yet, the advancing velocities of L4 and L5 (eastern side) kept increasing by 363 m yr^{-1} and 93 m yr^{-1}

respectively. The central part appeared increasing, except L3 where the “Loose Tooth” rift system exists (Fricker *et al.*, 2005).

The above results are consistent with the previous estimates (Zwally *et al.*, 2002b; Fricker *et al.*, 2002b) and indicate that the Amery Ice Shelf front has been advancing at approximately 1000 m yr⁻¹ during 1972-2009. According to the measurements of this study, the three sides of the Amery Ice Shelf front have performed differently. The central and eastern sides have been moving seaward faster than the western side.

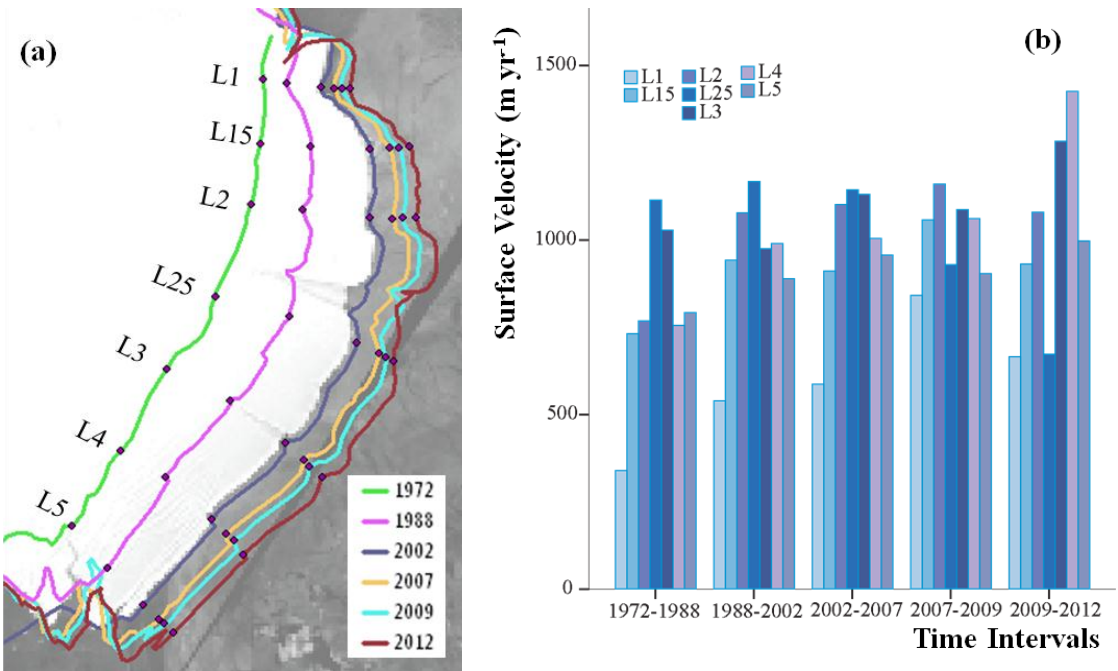


Figure 3.20 The Amery Ice Shelf front positions for seven time intervals from 1988 to 2012. Y axis presents the motion estimation in unit of meter per year.

Two longitudinal rifts exist at the front of the Amery Ice Shelf; the west one is called Rift A and the east one is called Rift B. The upstream ends of the Rift A and Rift B are marked as solid dots for five time periods, which include 1988, 2002, 2007, 2009, and 2012 (Figure 3.21a). The distances between the upstream end and the ice shelf front (Figure 3.21b) indicate that Rift B has been propagating until 2007, while Rift A stopped propagating two years later.

Fricker *et al.* (2005) observed the transverse-to-flow fracture, which is visible at the upstream end of Rift A, propagated 6 km towards Rift B during 1996-2000. It is predicted in the same publication that the iceberg will calve when the eastern end of the transverse-to-flow fracture meets Rift B. The geographic locations of the eastern end of the transverse-to-flow fracture are marked as solid light green dots in Figure 3.20a. Since there was no transverse-to-flow fracture observed prior to 1996, the geographic location for the year of 1988 is excluded. Figure 3.21c indicates that the eastern end of the transverse-to-flow fracture of Rift A has been moving approximately 1.5 km toward to the upstream end of Rift B since 2002. The dashed trend line well illustrates that a decreasing of the distances.

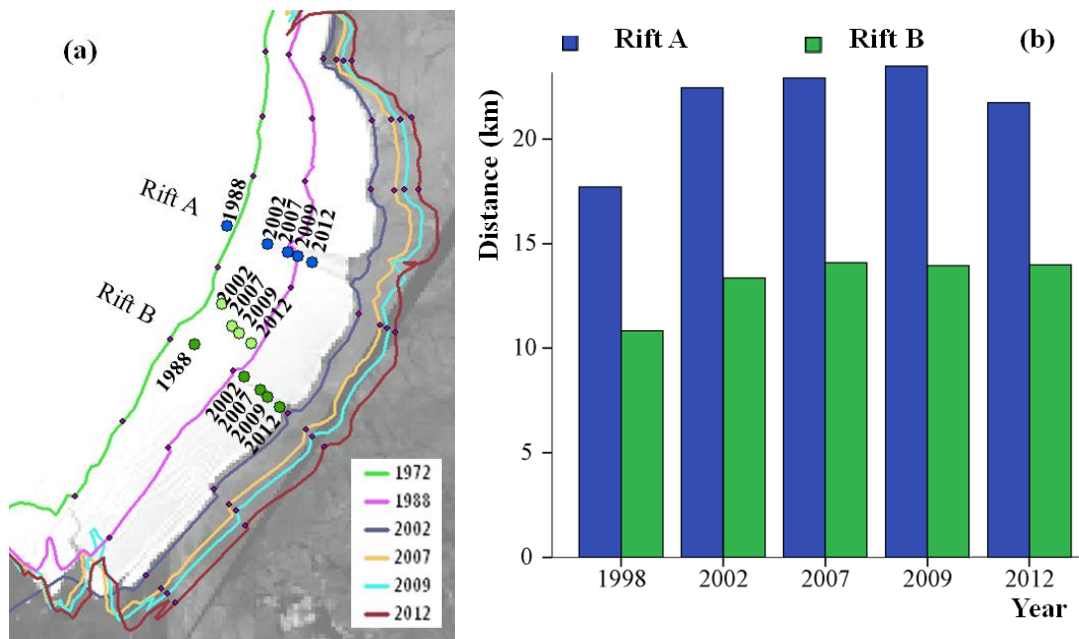


Figure 3.21 (a) The geographic locations of the upstream ends of rift A (solid dark blue dots) and rift B (solid dark green dots) as well as the eastern ends of the transverse-to-flow fracture of Rift A (solid light green); (b) The distances between the upstream ends of rift A and rift B and the ice shelf front for the five time periods during 1988-2012. The Y axis is the distance in km; (c) The plot of distances between the eastern end of the transverse-to-flow fracture of Rift A and the upstream end of Rift B with a dashed trend line.

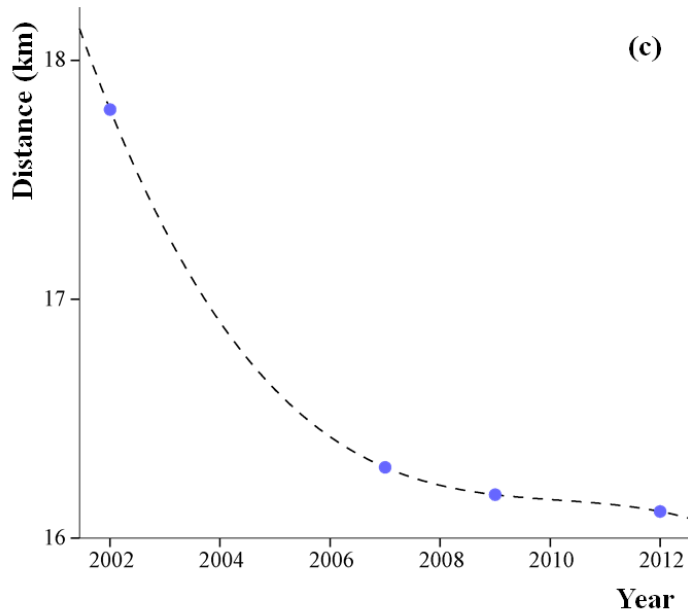


Figure 3.21 continued.

3.6 Discussions

Within the LAS, the complex two-dimensional surface velocity distribution pattern is observed in detail. As Price *et al.* (2008) noted the inland flow conducted by the inland ice migration is substantially slower than the surrounding fast-moving ice and usually is detectable by the feature tracking method. The ice surface velocities evolve from a slow and regular motion at interior regions of higher elevations. Along the flow direction, the grounded ice motion is strongly convoluted. Nearby the confluence zone of the Lambert Glacier, the Mellor Glacier, and the Fisher Glacier, the grounded ice is observed moving fast throughout the grounding line at approximately 800 m yr^{-1} . Entering the Amery Ice Shelf, the ice surface velocities distribute complicated due to

receiving some tributary ice streams while moving towards the northern terminus. By rescaling the surface velocity maps of the LAS, an obvious slowdown over the vast fast moving ice shelf is evident from late 1980s to 2000s.

A series of velocity comparisons are proposed after the surface velocity maps of three time intervals were conducted. Overall, the feature tracking method was able to capture the surface velocities of ice shelves and glaciers. Close agreement is observed both in magnitude and direction between the optical feature tracking for 1999-2004 and the RAMP InSAR surface velocity mapping of 1997-2000. Though the InSAR derived surface velocities are found to be approximately one order better than the feature tracking derived surface velocities for the time interval of 1999-2004, the feature tracking method is robust for simultaneously measuring two-dimensional displacement components. Advantageous over InSAR, feature tracking method works well to identify the fast-moving ice streams ($> 150 \text{ m yr}^{-1}$) and some tributary glaciers ($< 150 \text{ m yr}^{-1}$), these two ranges of surface velocities simultaneously during the tree time intervals investigated by this study.

The velocity change analysis presented by this study is much more extensive than King *et al.* (2007) who only used sparse and sporadic *in situ* and GPS ice velocity fields in their velocity change analysis. A good agreement is observed between the two time periods, during then the data cover between the forty-six velocity measurements and the feature tracking-derived surface velocity estimates. The differences between the feature tracking derived surface velocity measurements and GPS velocity fields are 29.8 yr^{-1} (10.6%) and 11.6 yr^{-1} (1.7%) during 1988-1990 and 1999-2004 respectively. The

velocity differences for 1988-1990 has almost doubles the velocity differences for 1999-2004, due to the spatial resolution satellite images used for 1988-1990 is twice of the 1999-2004's. On one hand, using high spatial resolution images enables to enhance the accuracy of the feature tracking derived surface velocities. On the other hand, the accuracy of the feature tracking derived surface velocities is always limited by the spatial resolution of used satellite images.

The fast-moving areas and the highest surface velocities of the three major glaciers enable to be observed for the three time periods of 1988-1990, 1999-2004, and 2007-2011 using feature tracking. Although the Fisher Glacier is smaller than the Lambert Glacier and the Mellor Glacier, the variations of the fast-moving areas and the highest surface velocities appear consistent among all the three glaciers. An obvious shrinkage of the fast-flowing regions has been observed from late 1980s to 1990s. A decreasing of highest surface velocities has been observed during the same time interval. Later, the fast-moving areas of all the three glaciers appear no significantly changes.

As mentioned earlier, the surface velocity variation is an important factor to estimate the mass balance variation of the LAS. Along the flow directions of the Lambert Glacier, the Mellor Glacier, and the Fisher Glacier, the surface velocities increase throughout the grounding line and enter the Amery Ice Shelf at the highest surface velocity. The surface velocities of the Amery Ice Shelf distribute complicated results in receiving the tributary glaciers while flowing seaward.

The entire Amery Ice Shelf front has been continuously advancing since 1972 according to the measurements derived from the satellite images. The central session of

the ice shelf front has been advancing at over 1000 m yr^{-1} . The velocities of both eastern and western sides remain increasing in 2007. Later, the velocities of the western side start to decrease, while the eastern side continues to increase.

CHAPTER IV

ESTIMATES OF MASS BALANCE OF THE LAMBERT GLACIER-AMERY ICE
SHELF SYSTEM (LAS)

4.1 Mass Balance of the LAS

Balance velocity is a useful indicator to ice dynamics (Testut *et al.*, 2003). The balance velocity is the depth-averaged velocity measured under the circumstance where the ice flux through a cross-sectional profile is in a state of balance with the mass inputs to the profile. Additional details about the balance velocity will be introduced. Due to lack of adequate knowledge of the surface velocity field, the prescribed ice-flow information of the LAS is usually derived from low resolution DEM data. The conventional method to determine the balance velocity is based on the upstream net accumulation rate and ice thickness (Joughin *et al.*, 1997). However, the existence of marine ice under the Amery Ice Shelf (Craven *et al.*, 2009) might add considerable uncertainty to the estimates of the conventional mass budget method due to lack of knowledge of the ice thickness. The recent availability of satellite image-derived altimeter data has enabled the ability to compute of balance velocities. The computation accuracy is enhanced by developing the two-dimensional finite-difference method (Budd & Warner, 1996), which is improved by Fricker *et al.* (2000).

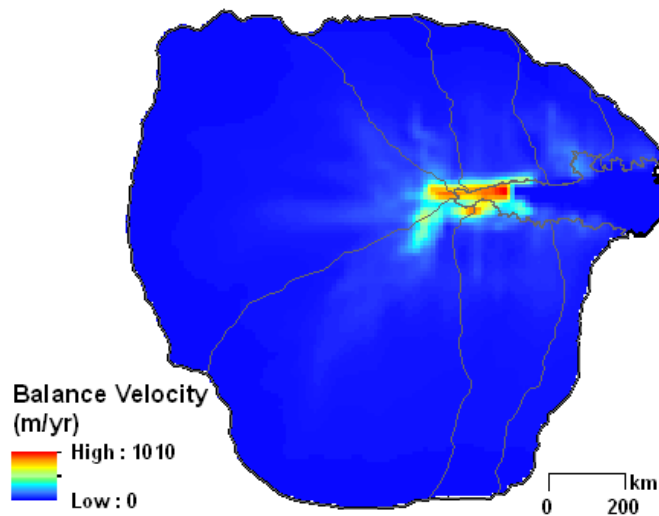


Figure 4.1 Mass balance velocity fields from the Byrd Research Center, Ohio State University (Wu & Jezek, 2004).

A mutual relationship is suggested among the global climate warming, snowfall accumulation, and glacier surging (Rignot *et al.*, 2008). The total mass balance of the ice shelf is an important dynamic process to quantify in order to understand complicated interactions occurring in the Antarctic ice sheet. The general pattern of surface velocity of a glacier is determined by the mass balance. Satellite-based surface velocity measurements have enabled the calculation of balance velocity for the entire LAS and have considerably enhanced our knowledge about its dynamic behaviors and mass balance states (Fricker *et al.*, 2000). Therefore, the balance velocities can provide invaluable insights into the complex flow characteristics of the LAS and can be used to constrain numerical glacier-ice shelf models of the system. The accurate balance velocity measurements also enable to resolve finer scale mass balance estimations of the

LAS (Wen *et al.*, 2008), since the densely distributed balance velocities illustrate the spatial variations of the mass balance estimations well. A major advantage of balance velocity measurements is that they can provide more detailed local information of the mass balance state beyond simple computation of the difference between the surface accumulation rates and the basal melting rates (Wen *et al.*, 2010).

As a unifying theme throughout this chapter, mass balance is usually used to describe the total mass change of an ice covered region (e.g., a glacier, an ice sheet, and a drainage basin). The Amery Ice Shelf (AIS) mass balance is an important indicator of the entire system state of ‘health’ and is sensitive to reflect the global climatic changes since any significant deviation from a balanced state could directly influence global sea level (Meier, 1993). As mentioned in previous chapters, the LAS drains a substantial part of the East AIS and therefore is an important drainage system in terms of the overall AIS mass balance (Fricker *et al.*, 2000).

Accurate estimations of the AIS mass balance are the prerequisite for improving the accuracy of estimating the AIS’s dynamic changes and its contribution to global climate changes. The estimates of mass balance depend on the snow accumulation component which themselves is subject to uncertainties (Alley *et al.*, 2007). Various researchers have estimated the mass balance of Amery Ice Shelf using different techniques as summarized in Table 4.1.

When Allison (1979) first estimated the mass balance of the LAS from the survey velocity data acquired in 1970s, the mass balance of LAS was $+12 \text{ Gt yr}^{-1}$, computed from a mass loss of 18 Gt yr^{-1} and approximately 30 Gt yr^{-1} via outflow into

the LAS. Using data acquired from the 1968-1970 Australian National Antarctic Research Expeditions (ANARE) survey (Budd *et al.*, 1982) and some previously assembled surface mass input data (Giovinetto & Bentley, 1985), Bentley and Geiovinetto (1990) estimated a negative imbalance of the LAS of -5 Gt yr^{-1} , using the previous snow accumulation rates (Allison, 1979; McIntyre, 1985) which were reinterpreted based on AVHRR satellite imagery.

In the past decade, both input and output mass balance distributions have been improved considerably using remote sensing and dynamic spatial models of the AIS (Rignot & Thomas, 2002). Others focused their studies on individual drainage system and outlet streams (Joughin & Tulaczyk, 2002). With the accurate delineation of grounding lines by D-InSAR techniques (Rignot *et al.*, 2011a), the grounding-line flux approach is likely to estimate mass balance more accurately than the previous mass-budget approach. Using the grounding-line flux approach, the mass balance is mainly determined by the difference between the ice discharges across the flux gates situated at the grounding zone and the accumulation distribution. A negative difference indicates mass loss while a positive difference indicates mass gain. The grounding-line flux approach can benefit greatly from accurate estimations of ice thickness and grounding lines.

Several researchers have made the observations of the mass balance for the LAS. Rignot (2002) suggested that the mass balance of the LAS is close to being in balance with outflow exceeding accumulation by $4 \pm 9\%$. Furthermore, Zwally *et al.* (2005) reported a similar small mass balance loss of $-5.75 \pm 0.63 \text{ Gt yr}^{-1}$. The grounded portion

of the LAS was estimated to have a positive mass imbalance of $+22.9 \pm 4.4 \text{ Gt yr}^{-1}$. Rignot *et al.* (2008) estimated a negative mass balance of the entire LAS at $-4 \pm 12 \text{ Gt yr}^{-1}$ using InSAR observations from 1992 to 2006. This result indicated that the grounded portion of the LAS gain ice mass, while the floating ice (Amery Ice Shelf) is the major source of mass loss of the LAS. Currently, differences exist among the mass balance estimates of the LAS from different methods and little work has investigated how the mass imbalance may vary over time. The entire grounded ice in the LAS is found approximately in balance, with a negative mass budget of -4.2 ± 9.8 (Wen *et al.*, 2008) and -4.1 ± 2.6 (Yu *et al.*, 2010) using remote sensing and *in situ* measurements to evaluate the mass budget for several individual sub-basins.

There are several reasons for the uncertainties of mass balance estimations. First, the important input components (e.g. accumulation distribution) of the LAS are usually estimated as portion of Antarctica (Zwally *et al.*, 2005; Rignot *et al.*, 2008). Large footprint and low spatial resolution inputs result in the uncertainty existing in the mass balance estimations. Second, the mass balance is determined simply from the differences between ice discharge and snowfall accumulation of the interior of the Antarctic continent (Rignot & Thomas, 2002b; Shepherd & Wingham, 2007). Third, the sparsity of surface velocity and ice thickness measurements, snowfall accumulation observations as well as precise grounding line data both in spatial and temporal resolution has limited the accurate estimates of mass balance in the LAS.

Some mass balance estimation methods require high quality and high spatial resolution elevation data (Nuth *et al.*, 2012). The ASTER Global DEM extends further

enough to cover the LAS. However, its accuracy degrades in the polar region, such as Antarctica (Rees, 2012). As the result, the outflow fluxes of the LAS region have been estimated by multiplying surface velocity fields and ice thickness. The details of the surface velocity field derivation have been discussed in Chapter II. A comparison of the computed balance velocities by this study and the previous observations is accomplished to update the assessment of the mass balance state of the LAS.

Table 4.1 Summary of previous estimation of net mass balance of the LAS.

Authors	Area	Observations (Gt yr⁻¹)
Allison (1979)	LAS	+12
Fricker <i>et al.</i> (2000)	LGDB	-3.25±12.05
Rignot (2002)	LAS	-2.3±6
Ren <i>et al.</i> (2002)	Upstream of the LGB	+5.7
Zwally <i>et al.</i> (2005)	Amery Ice Shelf	-5.75±0.63
Yu (2005)	LGDB	-7.63±2.65
Rignot <i>et al.</i> (2008)	LAS	-4±12
Wen <i>et al.</i> (2008)	Grounded LAS	-4.2±9.8
Yu <i>et al.</i> (2010)	LAS	-4.1±2.6

4.2 Concept of Balance Velocity

The concept of balance velocity was first discussed by Budd *et al.* in 1971. It represents the hypothetical depth-averaged velocity of an ice sheet that is under a ‘steady state’ condition, wherever its ice thickness and spatial extent are fixed over time. As illustrated in Figure 4.2, if the accumulation on the surface ($\int_0^x b_n(x) dx$) is equal to the discharging mass ($\bar{u}h(x)$) result in the control volume (V) remaining unchanged, then the depth-averaged velocity (\bar{u}) is called the balance velocity.

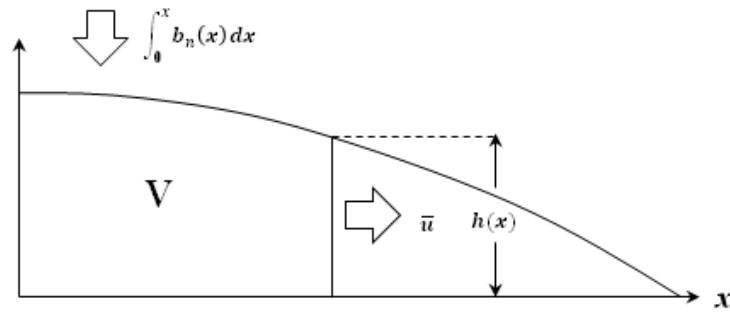


Figure 4.2 A schematic diagram illustrating dependence of \bar{u} on b_n on an ice sheet (modified based on Figure 5.1, Roger Hooke, 2005).

According to the principle of mass conservation in an incompressible medium, the depth-averaged velocity (so called mean horizontal velocity averaged over depth) at some distance, x can be represented as Equation 4.1, where $h(x)$ is the ice thickness and $\int_0^x b_n(x) dx$ is the accumulation on the surface.

$$\bar{u} = \frac{1}{h(x)} \int_0^x b_n(x) dx \quad (4.1)$$

To apply Equation 4.1 three sets of data projected on the same spatial grid are required, (1) snow accumulation distribution, (2) basal melting distribution, and (3) ice thickness. For lacking accurate accumulation and ice thickness data in some regions of Antarctica, a two-dimensional finite difference scheme is developed to calculate the mass balance velocity as illustrated in Equation 4.2 (Budd & Warner, 1996).

$$A(x, y) - M(x, y) = \nabla \cdot (\bar{V}(x, y)Z(x, y)) = \nabla \cdot (\phi(x, y)) \quad (4.2)$$

where $A(x, y)$ is the net surface accumulation distribution per unit time (the accumulation rate), $M(x, y)$ is the net basal melting distribution per unit time (the basal melting rate), $\bar{V}(x, y)$ is the depth-averaged horizontal velocity which indicates the fact that velocity decreases with depth, and $Z(x, y)$ is the ice thickness distribution. $\phi(x, y)$ represents the balance flux distribution, which provides vector spatial distribution information of horizontal flux per unit width with a given accumulation distribution. Hence the corresponding balance velocity is given by:

$$\bar{V}(x, y) = \frac{\phi(x, y)}{Z(x, y)} \quad (4.3)$$

Assuming the ice thickness remains unchanged over time, the balance velocity is roughly estimated as linearly proportional to the surface velocity (Paterson, 1994). The surface velocity factor (Equation 4.3) is considered dependent upon ice rheology, ice temperature profiles, and the possible presence of basal sliding (Fricker *et al.*, 2000). Considering the variation in horizontal direction with depth, a correction factor of 0.8-0.9 is usually applied to convert the depth-averaged ice velocity from the surface velocity measurements. One advantage of this method is that it is exclusive of the uncertainties originating from the DEM and the geoid model (Wen *et al.*, 2007).

4.3 Methods

To estimate continental-scale mass balance mainly through the following three approaches: (1) the mass-budget approach (Paterson, 1994; Mohr & Reeh, 2002), (2) measurements of elevation change over time (Wingham *et al.*, 1998), and (3) weighing of the ice sheets (Bentley & Wahr, 1998). Following Paterson (1994), the mass-budget approach is simple summation of four components as:

$$\Delta V / \Delta t = Q_a - Q_m - Q_c \pm Q_B \quad (4.4)$$

where V is the ice volume, Δt is time interval, Q_a is surface accumulation, Q_m is surface meltwater runoff, Q_c is loss by iceberg calving, and Q_B is basal balance. The mass budget approach works well where there is limited knowledge of floating ice distribution.

Ice-sheet mass balance can also be estimated by taking the differences between ice input and output fluxes or by monitoring changes in ice-sheet elevation as a proxy for volume changes. Due to lack of accurate measurements over time for the LAS region, uncertainties still exist in the estimation of mass balance of the LAS using the above methods.

For smaller spatial scales such as glaciers and ice shelves, the grounding-line flux approach (Yu, 2005; Wen *et al.*, 2008) and the mass-budget approach are often used to investigate its mass balance. The ice discharged from the interior of AIS is drained primarily along fast flowing ice streams and the three outlet glaciers that feed the Amery Ice Shelf through their individual grounding lines. The flux through the grounding line can be estimated for the imaginary flux gates. Unlike melting beneath the floating ice shelf, processes under the grounded ice are governed by the Antarctic continental melting (Rignot & Jacobs, 2002). The imaginary flux gates are placed along the grounding line wherever basal melting is ignorable and the ice surface velocity approximately represents the ice motion velocity at depth. For each individual flux gate the surface velocity fields are measured at evenly spaced locations using feature tracking. Ice discharge flux for each location is typically calculated using ice surface velocity, ice thickness, and the distance between those locations (Figure 4.3a, Equation 4.5 and Equation 4.6). The ice discharge flux for each imaginary flux gate is computed by summing all the ice discharge fluxes of each measured location (Figure 4.3b, Equation 4.1).

$$\varphi = v * h * l * f * \rho \quad (4.5)$$

$$\Phi = \sum_{i=0}^n \varphi_i \quad (4.6)$$

where φ is the ice discharge flux of an individual location, v is the surface velocity, h is the ice thickness, l is the distance between measured locations, f is surface velocity factor, ρ is the volume-averaged ice density (910 kg m^{-3} , Fricker *et al.*, 2001), and Φ is the ice discharge flux of an individual flux gate. Φ is calculated by summing all the fluxes within this gate together.

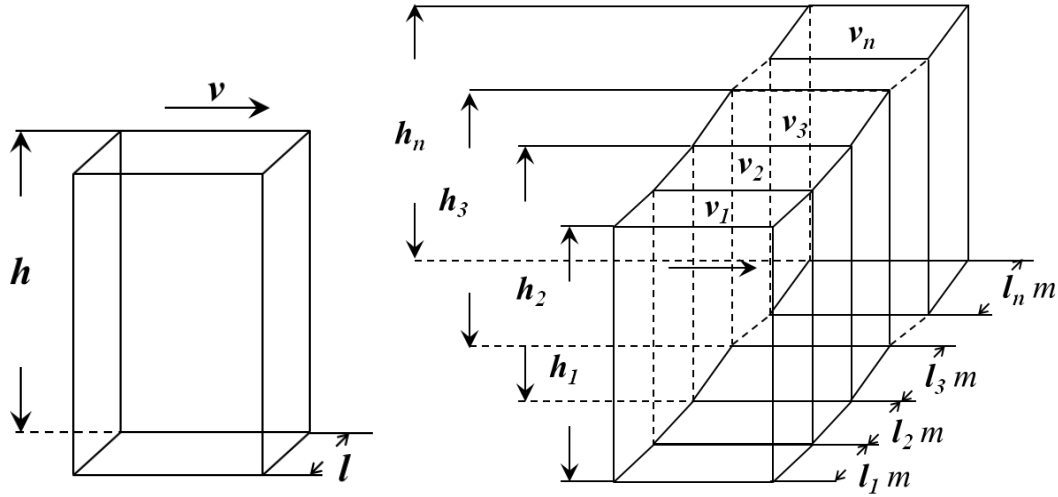


Figure 4.3 (a) Schematic diagram of flux mass for an individual location along a flux gate; (b) schematic diagram of flux mass for an imaginary flux gate.

The ice flux per unit width is the ice thickness multiplied by the depth-averaged velocity and is calculated by equations (1) (Fricker *et al.*, 2000) & (2) (Yu, 2005). In this study, the mass balance computation is conducted within a Geographic Information System (GIS) environment on a 1x1 km grid.

$$\underline{\Phi}_M(x, y) = \bar{V}(x, y)Z(x, y) \quad (4.7)$$

$$\bar{V}(x, y) = \bar{V}_s(x, y) * f \quad (4.8)$$

where $\underline{\Phi}_M(x, y)$ is referred to as the mass balance flux distribution. $\bar{V}(x, y)$ is the depth-averaged velocity vector (the balance velocity), $\bar{V}_s(x, y)$ is the surface velocity, and $Z(x, y)$ is the ice thickness. f is the surface velocity factor and referred to as a constant factor ranging from 0.7 to 1.0 (Budd & Warner, 1996). This study uses an $f = 1.0$. Therefore, the mass balance can be calculated as:

$$\Phi_V = \iint \underline{\Phi}_M(x, y) + \iint \underline{\Phi}_A(x, y) - \iint \underline{\Phi}_B(x, y) \quad (4.9)$$

where Φ_V is the mass budget, $\underline{\Phi}_A(x, y)$ is the accumulation distribution, and $\underline{\Phi}_B(x, y)$ is the basal melting distribution. In this sense, this study can compute the mass balance changes for the LAS with independent knowledge of accumulation distribution, basal melting distribution, and mass balance flux distribution.

The accumulation of each sub-basin is calculated by simply summing the accumulation rate of each pixel with GIS. ArcGIS10.0 has been used to compute the

differences between the ice discharge flux through all imaginary flux gates and the accumulation of the entire LAS. These accumulations are compared with the ice discharge fluxes to assess the mass balance of the LAS. Following that, an assessment of the state of balance in time series is discussed.

4.4 Data Acquisition

The mass balance variations discharging outward from the imagery flux gates are estimated using the flux gate method discussed above. The surface velocity fields nearby the flux gates are derived for three time periods of 1988-1990, 1999-2004, and 2007-2011. Further GIS-based computational analysis details refer to Chapter III.

Besides, the ice thickness and snowfall accumulation compilation of the LAS region is extracted from Antarctic-scale measurements. A 5 km grid of the Antarctic ice thickness (Figure 4.3) has been compiled by the Scientific Committee on Antarctic Research's (SCAR) BEDMAP project (Lythe *et al.*, 2001). This ice thickness data is a seamless suite of digital topographic models compiled from various data sources collected over the past 50 years. Most of the LAS is covered by high density ice thickness measurement points (> 1000 points per 100 km grid cell), which typically originate from aircraft radio-echo sounding campaigns. This ice thickness dataset is available on the BEDMAP website at http://www.antarctica.ac.uk/bas_research/data/access/bedmap/. To enhance the spatial resolution of this ice thickness dataset, the original 5 km grid (Figure 4.4a) is converted to point measurements, which were later interpolated into 0.4 km grid using ordinary

Kriging (Figure 4.4b). The reprocessing removes some of the high frequency noise resulting in smoother variations in ice thickness along the grounding line.

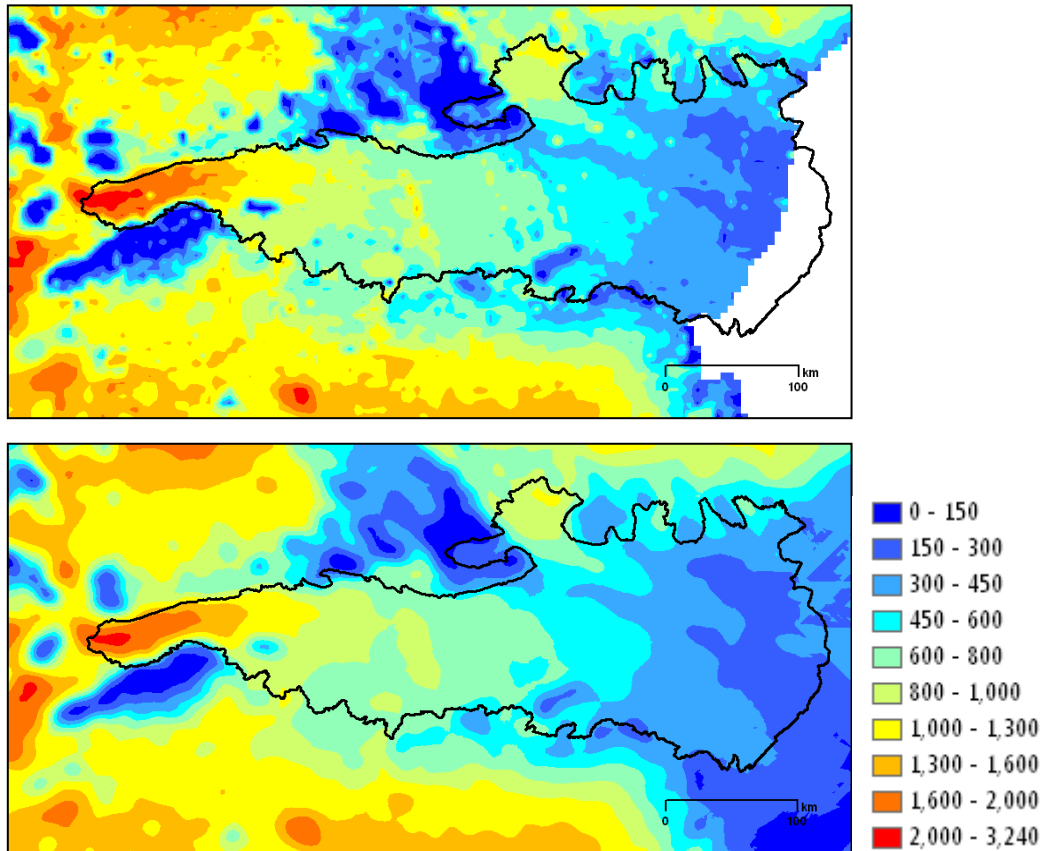


Figure 4.4 (a) Original ice thickness of the LAS region received from the SCAR BEDMAP project; (b) preprocessed ice thickness data by this study.

Snowfall accumulation over the Antarctic continent has shown no statistically significant change since 1950s (Monaghan *et al.*, 2006). However, a primary uncertainty

source in estimates of ice mass balance results from current error in ice-sheet-wide snowfall accumulation rates (Abdalati *et al.*, 2004). Accurate knowledge of snowfall accumulation patterns across the ice surface is essential for the understanding of mass balance dynamics (Van de Wal, 2004). Unfortunately, the *in situ* observations are sparse and it is difficult to capture the spatial pattern of snowfall accumulation. Monaghan *et al.* (2006) show substantial spatial variability across the Antarctic ice sheet by combining model simulations and observations primarily from ice cores. A 50-year average annual snowfall accumulation of the Lambert Glacier Basin during 1985-2004 is illustrated in Figure 4.5a. Arthern *et al.* (2006) produced a new accumulation map combining AMSR-E (Advanced Microwave Scanning Radiometer – Earth Observing System) satellite microwave observations that are sensitive to snow-cover and *in situ* measurements, which is shown in Figure 4.5b. Both of these two accumulation datasets are used for this research to assess the mass balance of the LAS.

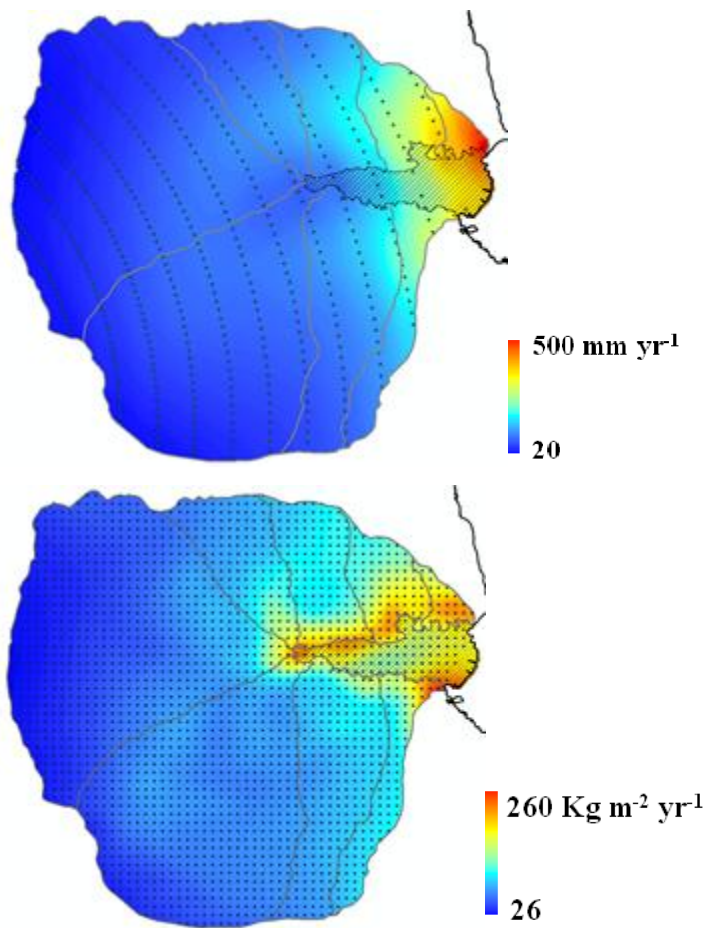


Figure 4.5 (a) Average annual snowfall accumulation map during 1955-2004 (Monaghan *et al.*, 2006); (b) annual snowfall accumulation map (Arthern *et al.*, 2006). The black dots represent the accumulation measurements.

Often referred as net accumulation, the net surface mass balance includes all processes which cause the mass balance changes, i.e. precipitation, evaporation, melting, run-off, and wind redistribution (Fricker *et al.*, 2000). Traditional methods for compile maps of the distribution of annual accumulation for Antarctica include interpolation of the limited observational data and can employ a variety of climate model results (Gallee

et al., 2005). However, Schlosser *et al.* (2002) found significant differences between the model results and the observational data. It is difficult to determine whether the significant differences are due to model underestimation in the accumulation or whether the observational data is not representative enough. Yu and his associates (2010) reorganized the accumulation distribution data given by Vaughan *et al.* (1999) and the uncertainty of this improved accumulation data is determined around $\pm 5\%$ (Table 4.2).

Table 4.2 Summary of snowfall accumulation data.

	Yu <i>et al.</i> (2010) Based on		Arthern <i>et al.</i>	Monaghan <i>et al.</i>
Sub-basins	Vaughan <i>et al.</i> (1999)	(2006)	(2006)	(2006)
<i>Lambert</i>	22.7 \pm 2.3	25 \pm 4.3		22.6 \pm 1.4
<i>Mellor</i>	23 \pm 2.3	23.9 \pm 4.9		22.3 \pm 1.3
<i>Fisher</i>	5.9 \pm 0.6	8.3 \pm 0.9		7.9 \pm 0.5
<i>West Tributary</i>	7.5 \pm 0.8	9.9 \pm 0.8		10.8 \pm 0.6
<i>Charybdis</i>	8.4 \pm 0.8	8.7 \pm 0.5		13.1 \pm 0.8
<i>West</i>				
<i>Downstream</i>	4.7 \pm 0.5	3 \pm 0.2		5.9 \pm 0.4
<i>East Tributary</i>	9.7 \pm 1.0	13.8 \pm 0.6		15.7 \pm 0.9
<i>East Downtown</i>	5.4 \pm 0.5	7.1 \pm 0.7		9.6 \pm 0.6
Total	87.2 \pm 2.9	99.8 \pm 13.9		107.9 \pm 6.5
Note: Measurement Unit Gt yr⁻¹				

Delineating the transition from where the bottom of the ice sheet transitions from a grounded to a floating regime, the grounding line is a highly sensitive indicator of the dynamic state of the ice stream (Fricker *et al.*, 2002a). A benchmark map (Fricker *et al.*, 2009) of the grounding line of the LAS has been developed recently from a combination of several satellite techniques, e.g. InSAR, visible-band imagery, and repeat-track laser altimetry and is archived by the National Snow and Ice Data Center (NSIDC) (http://nsidc.org/data/docs/agdc/nsidc0489_bindschadler/index.html). Another most recent grounding line product is conducted by Bindschadler *et al.* (2011) using combined Landsat-7 imagery and ICESat (Ice, Cloud, and land Elevation Satellite) laser altimetry data primarily collected between 1999 and 2003. These two grounding line products overlay with each other except occasionally small offsets. Covering one time interval which is of interest by this study, the latter grounding line product is used for further mass balance estimation.

Fifty-five imagery flux gates are deployed at the outlets of tributary basins along the grounding line as illustrated in Figure 4.6 following the approach of Wen *et al.* (2008). Since the ice surface motion is too slow to be detected by feature tracking, the surface velocity measurements perpendicularly across three flux gates within the West Down Stream Glacial Basin are missing. For this case, alternative flux gates 56-58 are placed on the nearby ice shelf surface approximately 20 km seaward from the grounding line.

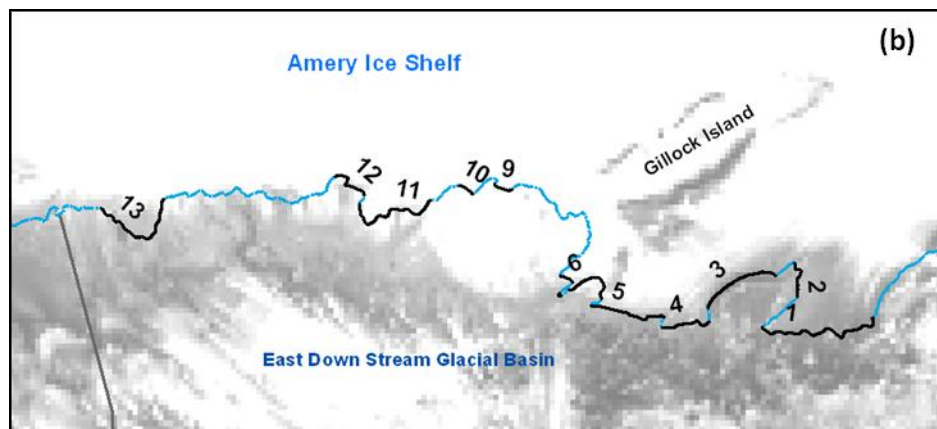
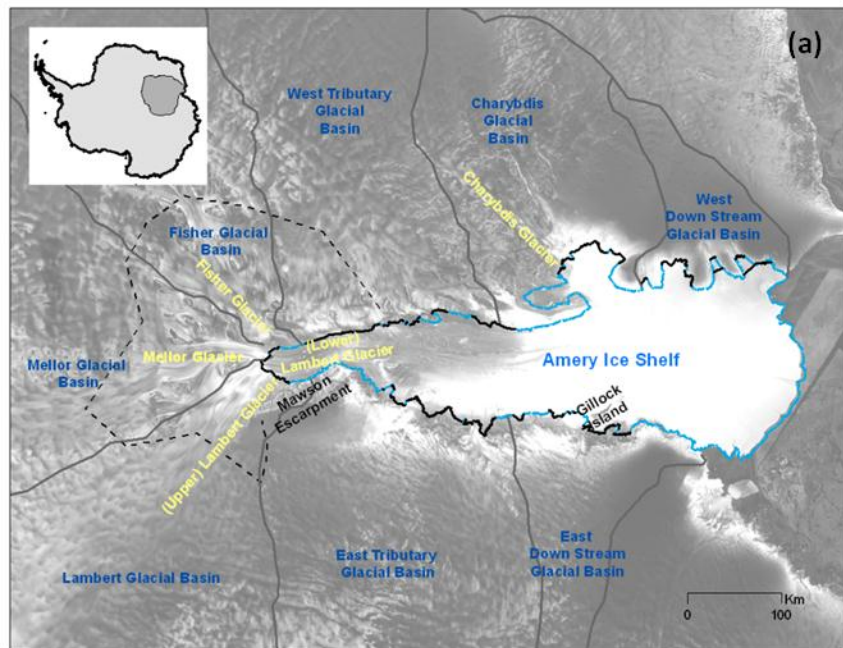


Figure 4.6 (a) Locations of imaginary flux gate (black solid lines) overlaid on a Radarsat-1 mosaic of Antarctica; (b) zoom to flux gates 1-13; (c) zoom to flux gates 14-40; (d) zoom to flux gates 41-55. The light blue represents the most recently derived grounding line of the Amery Ice Shelf (based on Bindschadler *et al.*, 2011).

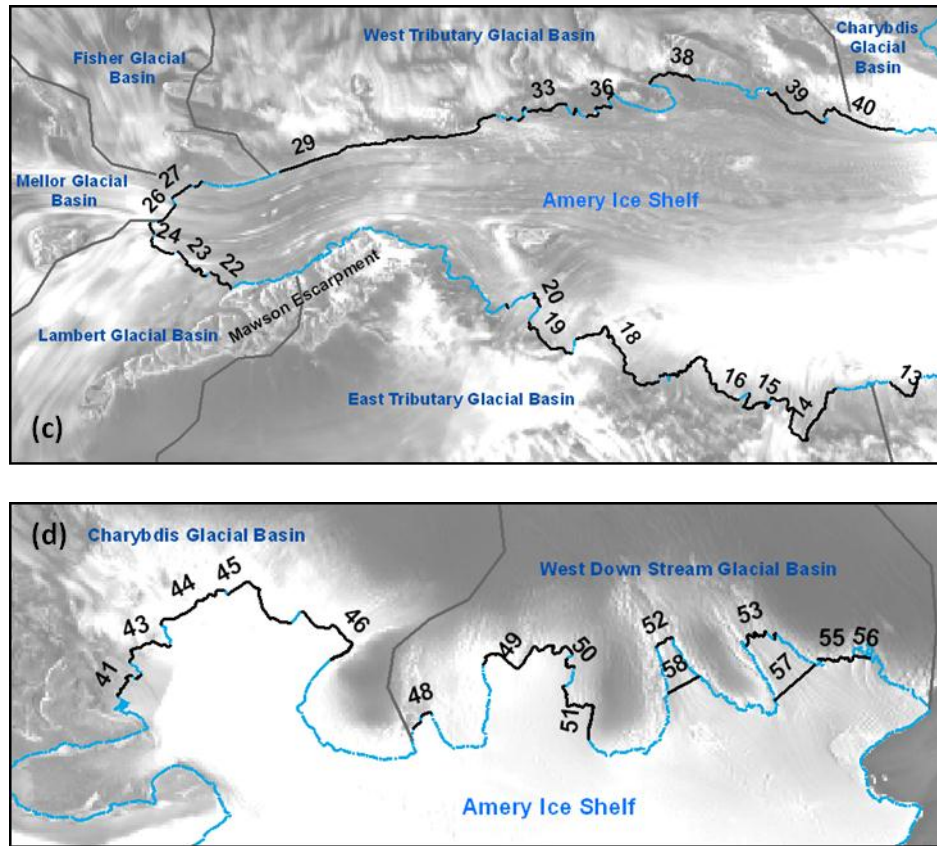


Figure 4.6 continued.

4.5 Computation Outcomes

4.5.1 Estimates of Ice Discharge through Flux Gates

Ice discharge flux is computed for each of the individual sub-basins listed in Table 4.3 for three time periods of 1988-1990, 1999-2004, and 2007-2011. A decreasing trend in ice flux is observed for the total ice discharge fluxes of the LAS from late 1980s to 2000s due to decreasing velocities. For each individual sub-basin, the trend of the ice discharge is inconsistent with each other. A decreasing trend has been observed in the

Mellor Glacial Sub-basin, the Fisher Glacial Sub-basin, and the West Tributary Glacial Sub-basin. A slight increasing is found in the East Down Stream Glacial Sub-basin. An obvious increasing and following with a decreasing of ice discharge is found in the Charybdis Glacial Sub-basin and the West Down Stream Glacial Sub-basin. The Lambert Glacial Sub-basin shows an opposite trend, a decreasing following with an increasing ice discharges going through the relevant flux gates. There is no significant change observed in the ice discharge of the East Tributary Glacial Sub-basin.

Table 4.3 Summary of ice discharge fluxes for the sub-basins during three time periods of 1988-1990, 1999-2004, and 2007-2011 in Gt yr⁻¹.

Sub-basins	1988-1990	1999-2004	2007-2011
<i>East Down Stream Glacial Sub-basin</i>	2.84	3.12	4.75
<i>East Tributary Glacial Sub-basin</i>	13.12	12.73	13.89
<i>Lambert Glacial Sub-basin</i>	25.78	20.16	22.19
<i>Mellor Glacial Sub-basin</i>	16.91	15.77	15.75
<i>Fisher Glacial Sub-basin</i>	0.89	0.79	0.67
<i>West Tributary Glacial Sub-basin</i>	13.71	12.21	10.98
<i>Charybdis Glacial Sub-basin</i>	7.93	10.42	7.53
<i>West Down Stream Glacial Sub-basin</i>	3.36	6.38	3.44
Total	84.6	81.6	79.2

4.5.2 Mass Balance and Its Variation Computation

Monaghan *et al.* (2006) demonstrated that the accumulation rate of the entire Antarctic continent has no significant variations since 1950s including the LAS region. Hence, it is reasonable to assume that changes in snow accumulation over the 50 years of study do not drive mass balance variations computed here, instead we assume the mass balance variation computed at the grounding line are mainly driven by the differences of ice discharge fluxes captured in variations in surface velocity. Similarly, changes in surface elevation are ignored due to lack of adequate knowledge of topographic change over the study period.

By considering only the grounded ice surface of the LAS, the basal melting effect does not have to be considered. Using the grounding-line flux approach (Equation 4.9), the mass balance of the LAS is estimated by subtracting the total ice discharge (Table 4.3) from the total accumulation of the grounded LAS ice surface (Table 4.2). The mass balance estimates are significantly influenced by using different accumulation data. Since the improved Vaughan *et al.* (1999)'s snow accumulation dataset has been most recently used for the mass balance studies of the LAS region by other researchers (Yu *et al.*, 2010), this improved accumulation data is used by this study for the further analysis of the mass balance variations.

The mass gain of the LAS grounded ice region has been increasing since late 1980s (Table 4.4). Considerable differences existing among the estimated accumulation datasets, consequently the mass balance estimates of the LAS grounded ice region appear different when different accumulation datasets are considered. Overall, the mass

gain of the LAS grounded ice region has been increased from $23.4 \pm 6.5 \text{ Gt yr}^{-1}$ for late 1980s, to $26.3 \pm 6.5 \text{ Gt yr}^{-1}$ for late 1990s, and to $28.7 \pm 6.5 \text{ Gt yr}^{-1}$ for late 2000s using the Monaghan *et al.*'s accumulation dataset. An increasing trend of the mass gain is also observed using Arthern *et al.*'s accumulation dataset and the mass balance estimates are $15.3 \pm 13.9 \text{ Gt yr}^{-1}$ for late 1980s, to $18.2 \pm 13.9 \text{ Gt yr}^{-1}$ for late 1990s, and to $20.6 \pm 13.9 \text{ Gt yr}^{-1}$ for late 2000s. Using the accumulation rate from Vaughan *et al.* (1999), the mass gain of the LAS grounded ice region has been increased from $2.7 \pm 2.9 \text{ Gt yr}^{-1}$ for late 1980s, to $5.6 \pm 2.9 \text{ Gt yr}^{-1}$ for late 1990s, and to $8.0 \pm 2.9 \text{ Gt yr}^{-1}$ for late 2000s.

Table 4.4 Summary of mass balance of the LAS grounded ice surface during the three time intervals of 1988-1990, 1999-2004, and 2007-2011.

Time Intervals	Yu <i>et al.</i> (2010) Based on	Monaghan <i>et al.</i>	Arthern <i>et</i>
	Vaughan <i>et al.</i> (1999)	(2006)	<i>al.</i> (2006)
	(Gt yr ⁻¹)		
1988-1990	2.7 ± 2.9	23.4 ± 6.5	15.3 ± 13.9
1999-2004	5.6 ± 2.9	26.3 ± 6.5	18.2 ± 13.9
2007-2011	8.0 ± 2.9	28.7 ± 6.5	20.6 ± 13.9

4.6 Discussions

In this chapter, the ice fluxes across the grounding lines of imaginary flux gates are calculated for three time intervals, using which the mass balance variations are estimated for the entire LAS region.

Among the previous remote sensing based mass balance estimates listed in Table 4.1, Wen *et al.* (2008) and Yu *et al.* (2010) used the grounding-line flux approach for the grounded ice surface as was done in this study. Comparing the mass flux estimates in this dissertation work with these two previous studies reveals some similarities, but also some differences, Wen *et al.* (2008) estimated a mass loss of $-4.2 \pm 9.8 \text{ Gt yr}^{-1}$ but both this study and Yu *et al.* estimated a higher mass gain using the same accumulation input dataset. Yu *et al.* (2010) computed a mass gain of $22.9 \pm 4.4 \text{ Gt yr}^{-1}$ for the grounded region of the LAS, while this study computes a mass gain of $5.6 \pm 2.9 \text{ Gt yr}^{-1}$. The smaller uncertainty of the mass balance estimates of this study is the result of using the improved accumulation data over the LAS. A detailed discussion and further analysis about the causes of different estimates is a possible future study direction, since the estimated mass balance differences between Yu *et al.* (2010)'s and this study's would appear to result from either different input components for the grounding-line flux approach or differences in the positions of the flux gates. It is interesting to note, that the major differences in flux between this study and the Yu *et al.* (2010) study is fluxes through the smaller eastern and western tributary basins, while fluxes through the Lambert, Mellor and Fisher tributary glaciers are much similar.

The ice discharge flux of individual sub-basins appears differently among three time intervals, the combined ice discharge fluxes are analyzed for the eastern, central, and western sides of the LAS. The eastern side of the LAS grounded ice region appear no change from late 1980s to 1990s and increase to 18.64 Gt yr^{-1} of late 2000s. The central part of the LAS grounded ice region is the major channel to transport the ice from the interior LAS to the Amery Ice Shelf. The ice discharge fluxes of the central part are nearly the sum of the eastern and western sides. Fluctuating around 40 Gt yr^{-1} , the ice discharge fluxes of the central part decrease from 43.58 Gt yr^{-1} for late 1980s to 36.72 Gt yr^{-1} for late 1990s and increase to 38.61 Gt yr^{-1} for late 2000s. The ice discharge fluxes of the western side increase from 25.00 Gt yr^{-1} for late 1980s to 29.01 Gt yr^{-1} for late 1990s and decrease to 21.95 Gt yr^{-1} for late 2000s.

As the previous research focus on the LAS mass balance during an individual time interval, this study has illustrated the mass balance variations of the LAS among multiple time intervals. Using RAMP InSAR velocities, the ice fluxes across the flux gates of the LAS are $88.9 \pm 8.9 \text{ Gt yr}^{-1}$ (Wen *et al.*, 2008) for the time interval of 1997-2000. This study provides a similar estimate (81.6 Gt yr^{-1}) of the ice fluxes across the flux gates for the time interval of 1999-2004. The ice fluxes across the flux gates for the other two time intervals are 84.6 Gt yr^{-1} and 79.2 Gt yr^{-1} for 1988-1990 and 2007-2011 respectively.

Using the grounding-line flux approach, the mass gain of the LAS grounded ice is $2.7 \pm 2.9 \text{ Gt yr}^{-1}$ for late 1980s, to $5.6 \pm 2.9 \text{ Gt yr}^{-1}$ for late 1990s, and to $8.0 \pm 2.9 \text{ Gt yr}^{-1}$ for late 2000s. Since the snow accumulation rate and ice thickness are assumed to be

constant over the study period, decrease of surface velocities will result in the increasing mass gain of the LAS among different time intervals.

CHAPTER V

CONCLUSIONS

5.1 Conclusions

The major contribution of this dissertation is the first attempt to examine long-term ice flow variability at the fine spatial scale over the entire LAS. The spatial detailed surface velocity measurements from previous research are confined to the time interval of 1997-2000. This research uses feature tracking to extend the timeline of previous ice flow studies forward and backward a decade. Therefore, this research provides the foundation for the spatially detailed analysis of surface velocity variations over the past decades.

One major advantage of the feature tracking derived velocity measurements is that the results are not limited by the acquisition of high spatial resolution DEM products. Surface velocities are derived for three time intervals using high spatial resolution sequential satellite images for the LAS. Glacial dynamic variations are able to be investigated by using remote sensing derived surface velocities with consistent data processing.

However, even though the updated surface velocity fields and ice thickness measurements (Lythe *et al.*, 2001) are used for this study, the grounding-line flux approach significantly depends upon high quality snow accumulation inputs and the accurate geographic location of the grounding line over time.

5.2 Summary of Findings

The mass balance estimation of the Antarctic Ice Sheet is an important current research topic among the scientists. A substantial body of previous research has been conducted to illustrate the mass balance variations of the West Antarctic Ice Sheet. This dissertation investigates the largest glacier-ice shelf system in East Antarctica, the LAS which has received less study.

Surface velocities were derived using several methods. Feature tracking was demonstrated to be a good method to derive surface velocities using multi-temporal optical images. The feature tracking derived surface velocities of the LAS are analyzed in three aspects of spatial distribution, temporal variations, and ice front motion. The surface velocities of the entire LAS region are mapped for three time intervals of 1988-1990, 1999-2004, and 2007-2011. An important research finding is that the ice flow of the Amery Ice Shelf front has exhibited slowdowns from late 1980s to 2000s. The ice flows of the Lambert Glacier, Mellor Glacier, and Fisher Glacier have experienced velocity decrease from late 1980s to 1990s as well. Good agreement is observed between the feature tracking derived surface velocities and the *in situ* GPS velocity measurements collected for the same time interval. In addition, this study demonstrates the Amery Ice Shelf front has continued its seaward which began in 1972 through 2012. The central part of the Amery Ice Shelf front is found moving at approximately 1000 m yr^{-1} . Both eastern and western portions have been advancing as well, but the eastern portion moves slower than the western portion over the last decade.

Finally, mass balance estimates of the LAS grounded ice region are constructed for the above three time intervals using grounding-line flux approach. The total ice discharge fluxes of the LAS grounded ice region are found to be 84.55 Gt yr^{-1} for 1988-1990, 81.60 Gt yr^{-1} for 1999-2004, and 79.20 Gt yr^{-1} for 2007-2011 using the snow accumulation dataset of Monaghan *et al.* 2006. The estimate for the 1999-2004 time period is in good agreement with similar measurements constructed using InSAR derived surface velocities. A fundamental assumption of the research is that the accumulation distribution is assumed not changed over time (Monaghan *et al.*, 2006), therefore, the mass gain of the LAS grounded ice region is increasing due to the decreased ice discharge fluxes. Using the grounding-line flux approach, the mass gain of the LAS grounded ice surface are $2.7 \pm 2.9 \text{ Gt yr}^{-1}$ for late 1980s, to $5.6 \pm 2.9 \text{ Gt yr}^{-1}$ for late 1990s, and to $8.0 \pm 2.9 \text{ Gt yr}^{-1}$ for late 2000s. This approach is sensitive to the accumulation dataset used. While employing different accumulation datasets as input does produce consistent mass gains over time, the mass balance estimates do vary significantly in magnitude. Therefore, the mass balance estimates using grounding-line flux approach heavily depend upon the accumulation distribution of the entire LAS.

5.3 Future Work

The primary concerns of this study consist of the completion of surface velocity mapping and the accuracy of the surface velocity measurements and mass balance estimates.

Although this study is not affected by the areas where feature tracking does not work well to derive surface velocities, it would be one of further interests to derive surface velocities using remote sensing data and complete the surface velocity map of the LAS. Alternative datasets and methods might be sought to supplement missing surface velocity measurements.

Improving the accuracy of feature tracking applied in the LAS is another possible avenue of research. Depending upon the data acquisition, using high spatial resolution remotely sensed images could prove an efficient way to improve the feature tracking derived surface velocity measurements.

Several of the inputs to the grounding-line flux approach are in need of being updated in next decade. Currently the newer accumulation distributions (Monaghan *et al.*, 2006; Arthern *et al.*, 2006) are different from the Vaughan *et al.*'s (1999) accumulation dataset. The geographic locations of the grounding line have been changing over time (Herzfeld *et al.*, 1994) due to the effect of beneath basal-melting distribution (Walker *et al.*, 2008). The changes of groundling line, particularly impact where flux gates used in the remote sensing approached are located, and improved, and changing positions, need be considered when the grounding line flux approach is used for future mass flux estimates.

REFERENCES

- Alley, R.B., Clark, P.U., Huybrechts, P. & Joughin, I. (2005). Ice-sheet and sea-level changes. *Science*, 310(5747), 456-460.
- Alley, R.B., Spencer, M.K. & Anandakrishnan, S. (2007). Ice-sheet mass balance: assessment, attribution and prognosis. *Annals of Glaciology*, 46, 1-7.
- Allison, I. (1979). The mass budget of the Lambert Glacier drainage basin, Antarctica. *Journal of Glaciology*, 22(87), 223-235.
- Ahn, Y. & Howat, I. (2011). Efficient automated glacier surface velocity measurement from repeat images using multi-image/multichip and null exclusion feature tracking. *IEEE Transactions on Geoscience and Remote Sensing*, 49(8), 2838-2846.
- Arthern, R., Winebrenner, D. & Vaughan, D. (2006). Antarctic snow accumulation mapped using polarization of 4.3-cm wavelength microwave emission. *Journal of Geophysical Research*, 111(D6).
- Attema, EPW., Duchossois, G. & Kohlhammer, G. (1998). ERS-1/2 SAR land applications: overview and main results. Geoscience and Remote Sensing Symposium Proceedings, 1998. *IGARSS '98. 1998 IEEE International*, 4, 1796-1798.
- Ayoub, F., Leprince, S. & Avouac, J.P. (2009). Co-registration and Correlation of Aerial Photographs for Ground Deformation Measurements. *ISPRS Journal of Photogrammetry and Remote Sensing*, 64, 551-560.
- Bamber, J.L., Vaughan, D.G. & Joughin, I. (2000). Widespread complex flow in the interior of the Antarctic Ice Sheet. *Science*, 287(5456), 1248-1250.

Bamler, R. & Hartl, P. (1998). Synthetic aperture radar interferometry. *Inverse Problems*, 14(4), R1-R54.

Bassis J., Fricker, H., Coleman, R. & Minster, J. (2008). An investigation into the forces that drive ice-shelf rift propagation on the Amery Ice Shelf, East Antarctica. *Journal of Glaciology*, 54(184), 17-27.

Bentley, C.R. & Giovinetto, M.B. (1990). Mass balance of Antarctica and sea level change. *International Conference on the Role of Polar Regions in Global Change*, 11-15 June 1990, 481-488.

Bentley, C.R. & Wahr, J.M. (1998). Satellite gravity and the mass balance of the Antarctic ice sheet. *Journal of Glaciology*, 44(147), 207-213.

Bernstein, R. (1983). Image geometry and rectification. In: R.N. Colwell (ed.), *Manual of Remote Sensing*. American Society of Photogrammetry, Falls Church, VA, pp. 881-884.

Berthier, E., Raup, B. & Scambos, T. (2003). New velocity map and mass-balance estimate of Mertz Glacier, East Antarctica, derived from Landsat sequential imagery. *Journal of Glaciology*, 49(167), 503-511.

Bindschadler, R. (1993) Siple Coast project research of Crary Ice Rise and the mouths of Ice Stream-B and Ice Stream-C, West Antarctica: Review and new perspectives. *Journal of Glaciology*, 39(133), 538-552.

Bindschadler, R. (1998). Monitoring ice sheet behavior from space. *Review of Geophysics*, 36(1), 79-104.

Bindschadler, R., Choi, H., Wichlacz, A., Bingham, R., Bohlander, J., Brunt, K., Corr, H., Drews, R., Fricker, H., Hall, M., Hindmarsh, R., Kohler, J., Padman, L., Rack, Rotschky, G., Urbini, S., Vornberger, P. & Young, N. (2011). Getting around Antarctica: New High-Resolution Mappings of the Grounded and Freely-Floating Boundaries of the Antarctic Ice Sheet Created for the International Polar Year. *The Cryosphere Discussions*, 5, 183-227.

Bindschadler, R., & Scambos, T.A. (1991). Satellite-image-derived velocity-field of an Antarctic ice stream. *Science*, 252, 242-246.

Bindschadler, R., Vornberger, P., Blankenship, D., Scambos, T. & Jacobel, R. (1996). Surface velocity and mass balance of Ice Streams D and E, West Antarctica. *Journal of Glaciology*, 42, 461-475.

Bindschadler, R., Vornberger, P.L. & Shabtaie, S. (1993). The detailed net mass balance of the ice plain on Ice Stream B, Antarctica: a GIS approach. *Journal of Glaciology*, 133, 471-482.

Bloemendal, J., Ehrmann, W., Hambrey, M.J., McKelvey, B.C., Matthews, R. & Whitehead, J.M. (2003). Geochemical and rock magnetic records from sediments of the Cenozoic Pagodroma Group, Prince Charles Mountains, East Antarctica: implications for provenance and weathering. *Antarctic Science*, 15(3), 365-378.

Braithwaite, R.J. (1995). Positive degree-day factors for ablation on the Greenland ice-sheet studies by energy-balance modeling. *Journal of Glaciology*, 41(137), 153-160.

Brunt, K. M., H. A. Fricker, L. Padman, and S. O'Neel. (2010). ICESat-Derived Grounding Zone for Antarctic Ice Shelves. Boulder, Colorado USA: National Snow and Ice Data Center. Digital media.

Budd, W. (1966). The dynamics of the Amery Ice Shelf. *Journal of Glaciology*, 6(45), 335-357.

Budd, W.F., Corry, M.J. & Jacka, T.H. (1982). Results from the Amery Ice Shelf Project. *Annals of Glaciology*, 3, 36-41.

Budd, W.F., Jenssen, D. & Radok, U. (1971). Derived physical characteristics of Antarctic ice sheet. *ANARE Interim Report*, 124, Kingston, Tasmania, Australia.

Budd, W.F. & McInnes, B.J. (1979). Periodic surging of the Antarctic ice sheet - an assessment by modeling. *Hydrological Sciences*, 24(1), 95-104.

Budd, W.F. & Warner, R.C. (1996). A computer scheme for rapid calculations of balance-flux distributions. *Annals of Glaciology*, 23, 21-27.

Burgess, E.W., Forster, R.R., Larsen, C.F. & Braun, M. (2012). Surge dynamics on Bering Glacier, Alaska, in 2008-2011. *The Cryosphere*, 6, 1181-1204.

Chen, C.H. (1999). Information processing for remote sensing. Singapore, World Scientific, pp570.

Cheng, X. & Xu, G. (2006). The integration of JER-1 and ERS SAR in differential interferometry for measurement of complex glacier motion. *Journal of Glaciology*, 52(176), 80-88.

Derauw, D. (1999). DInSAR and coherence tracking applied to glaciology: the example of Shirase Glacier. Advancing ERS SAR interferometry from applications

towards operations. Noordwijk, European Space Agency, CD-ROM. (ESA Publication SP-478).

Dietrich, R., Maas, H.-G., Baessler, M., Rußke, A., Richter, A., Schwalbe, E. & Westfeld, P. (2007). Jakobshavn Isbræ, west Greenland: Flow velocities and tidal interaction of the front area from 2004 field observations. *Journal of Geophysical Research*, 112(F3), p. F03 S21.

Drewry, D.J. (1983). Antarctica: geological and geophysical folio. Scott Polar Research Institute, Cambridge, U.K.

Fahnestock, M., Bindschadler, R., Kwok, R. & Jezek, K. (1993). Greenland ice sheet surface properties and ice dynamics from ERS-1 SAR imagery. *Science*, 262(5139), 1530-1534.

Fink, D., McKelvey, B., Hambrey, M.J., Fabel, D. & Brown, R. (2006). Pleistocene deglaciation chronology of the Amery Oasis and Radok Lake, northern Prince Charles Mountains, Antarctica. *Earth and Planetary Science Letters*, 243(1-2), 229.

Fricker, H.A., Allison, I., Craven, M., Hyland, G., Ruddell, A., Young, N. & Popov, S. (2002a). Redefinition of the Amery Ice Shelf, East Antarctica, grounding zone. *Journal of Geophysical Research*, 107(B5), 1-9.

Fricker, H.A., Coleman, R., Padman, L., Scambos, T.A., Bohlander, J. & Brunt, K.M. (2009). Mapping the grounding zone of the Amery Ice Shelf, East Antarctica using InSAR, MODIS and ICESat. *Antarctic Science*, 21(5), 515-532.

Fricker, H.A., Popov, S., Allison, I. & Young, N. (2001). Distribution of marine ice beneath the Amery Ice Shelf. *Geophysical Research Letters*, 28(11), 2241-2244.

Fricker, H.A., Warner, R.C. & Allison, I. (2000). Mass balance of the Lambert Glacier-Amery Ice Shelf system, East Antarctica: a comparison of computed balance fluxes and measured fluxes. *Journal of Glaciology*, 46 (155), 561-570.

Fricker, H.A., Young, N.W., Allison, I. & Coleman, R. (2002b). Iceberg calving from the Amery Ice Shelf, East Antarctica. *Annual of Glaciology*, 34, 241-246.

Fricker, H.A., Young, N.W., Coleman, R., Bassis, J.N. & Minster, J.B. (2005). Multi-year monitoring of rift propagation on the Amery Ice Shelf, East Antarctica. *Geophysical Research Letters*, 32(2), 1-5.

Gallee, H., Peyaud, V. & Goodwin, I. (2005). Simulation of the net snow accumulation along the Wiles Land transect, Antarctica, with a regional climate model. *Annals of Glaciology*, 41, 17-22.

Giovinetto, M. B. (1964), The drainage systems of Antarctica: Accumulation. In M. Mellor (Ed.), *Antarctic Snow and Ice Studies. Antarctic Research Series 2*, 127-155, AGU, Washington, D.C.

Giovinetto, M.B. & Bentley, C.R. (1985). Surface balance in ice drainage systems of Antarctica. *Antarctic Journal of the U.S.*, 20(4), 6-13.

Giovinetto, M.B. & Zwally, H.J. (2000). Spatial distribution of net surface accumulation on the Antarctic ice sheet. *Annals of Glaciology*, 31, 171-178.

Goldberg, D., Holland, D. & Schoof, C. (2009). Grounding line movement and ice shelf buttressing in marine ice sheets. *Journal of Geophysical Research-Earth Surface*, 114, 1-23.

Goldstein, R.M., Engelhard, H., Kamb, B. & Frolich, R.M. (1993). Satellite radar interferometry for monitoring ice sheet motion: application to an Antarctic ice stream. *Science*, 262, 1525-1530.

Goldstein, R.M., Zebker, H.A. & Werner, C.L. (1988). Satellite radar interferometry: two-dimensional phase unwrapping. *Radio Science*, 23(4), 713-720.

Gray, A.L., Mattar, K.E., Vachon, P.W., Bindshadler, R., Jezek, K.C., Forster, R. & Crawford, J.P. (1998). InSAR results from the RADARSAT Antarctic Mapping Mission data: Estimation of glacier motion using a simple registration procedure. *IGARSS '98 International Geoscience and Remote Sensing Symposium Proceedings*, 1638-1640.

Hambrey, M.J. (1991). Structure and dynamics of the Lambert Glacier-Amery Ice Shelf System: implications for the origin of Prydz Bay sediments. *Proceedings of the Ocean Drilling Program, Scientific Results*, 119, 61-75.

Hambrey, M.J. & Dowdeswell, J.A. (1994). Flow regime of the Lambert Glacier-Amery Ice Shelf system, Antarctica: structural evidence from Landsat imagery. *Annals of Glaciology*, 20, 401-406.

Heid, T. & Kaab, A. (2012). Evaluation of existing image matching methods for deriving glacier surface displacements globally from optical satellite imagery. *Remote Sensing of Environment*, 118, 339-355.

Hellmer, H.H. & Jacobs, S.S. (1992). Ocean interactions with the base of Amery Ice Shelf, Antarctica. *Journal of Geophysical Research*, 97(C12), 20305-20317.

Hellmer, H.H. (2004). Impact of Antarctic ice shelf basal melting on sea ice and deep ocean properties. *Geophysical Research Letters*, 31(10), L10307.

Herzfeld, U.C., Lingle, C.S. & Lee, L.H. (1994). Recent advance of the grounding line of Lambert Glacier, Antarctica, deduced from satellite-Radar altimetry. *Annals of Glaciology*, 20, 43-47.

Higham, M., Craven, M., Ruddell, A. & Allison, I. (1997). Snow accumulation distribution in the interior of the Lambert Glacier basin, Antarctica. *Annals of Glaciology*, 25, 412-417.

Hock, R. (2003). Temperature index melt modeling in mountain areas. *Journal of Hydrology*, 282, 104-115.

Houghton, J.T., Ding, Y., Griggs, D.J., Noguer, M., Van der Linden, P., Dai, X. & Johnson, C.I. (eds.). (2001). In *Climate change 2001: The Scientific Basis* (contribution of Working Group 1 to the Third Assessment Report of the Intergovernmental Panel on Climate Change), pp. 639-694. Cambridge University Press, Cambridge, U.K.

Huintjes, E., Li, H., Sauter, T., Li, Z. & Schneider, C. (2010). Degree-day modeling of the surface mass balance of Urumqi Glacier No. 1, Tian Shan, China. *The Cryosphere Discussion*, 4, 207-232.

Howat, I.M., Joughin, I. & Scambos, T.A. (2007). Rapid changes in ice discharge from Greenland outlet glaciers. *Science*, 315(5818), 1559-1561.

IPCC. (2007). Climate change 2007: Mitigation. Contribution of Working group III to the Fourth Assessment Report of the Intergovernmental Panel on Climate Change (eds), Cambridge University Press, Cambridge, United Kingdom and New York, NY, USA.

Jacobs, S., Hellmer, H., Doake, M., Jenkins, A. & Frolich, M. (1992). Melting of ice shelves and the mass balance of Antarctica. *Journal of Glaciology*, 38(130), 375-387.

Janssen, V. & Hurd, R. (2008). Spatial Sciences on Ice: 50 years of Australian activities on the Amery Ice Shelf, *East Antarctica. Australian Geographer*, 39(4), 389-408.

Jezek, K. (2002). RADARSAT-1 Antarctic Mapping Project: change-detection and surface velocity campaign. *Annals of Glaciology*, 34(1), 263-268.

Joughin, I. (2002). Ice-sheet velocity mapping: a combined interferometric and speckle-tracking approach. *Annals of Glaciology*, 34, 195-201.

Joughin, I.R., Fahnestock, M.A. & Bamber, J.L. (2000). Ice flow in the northeast Greenland ice stream. *Annals of Glaciology*, 31, 141-146.

Joughin, I., Fahnestock, M., Ekholm, S. & Kwok, R. (1997). Balance velocities of the Greenland ice sheet. *Geophysical Research Letters*, 24(23), 3045-3048.

Joughin, I. & Tulaczyk, S. (2002). Positive mass balance of the Ross Ice Streams, West Antarctica. *Science*, 295(5554), 476-480.

Joughin, I., Tulaczyk, S., Fahnestock, M. & Kwok, R. (1996). A mini-surge on the Ryder Glacier, Greenland, observed by satellite radar interferometry. *Science*, 274(5285), 228-230.

Kiernan, Rob. (2001). Ice Sheet Surface Velocities Along the Lambert Glacier Basin Traverse Route. Antarctic Cooperative Research Centre and Australian Antarctic Division, Research Report No. 23, May 2001.

King, M. (2002). The dynamics of the Amery Ice Shelf from a combination of terrestrial and space geodetic data. (PhD thesis, University of Tasmania, Hobart, Australia).

King, M.A., Coleman, R., Freemantle, A., Fricker, H.A., Hurd, R.S., Legresy, B. & Warner, R. (2009). A four-decade record of elevation change of the Amery Ice Shelf, East Antarctica. *Journal of Geophysical Research*, 114, 1-13.

King, M.A., Coleman, R., Morgan, P.J. & Hurd, R.S. (2007). Velocity change of the Amery Ice Shelf, East Antarctica, during the period 1968-1999. *Journal of Geophysical Research*, 112(F1), 1-16.

King, M., Nguyen, L., Coleman, R. & Morgan, P. (2000). Strategies for high precision processing of GPS measurements with application to the Amery Ice Shelf, East Antarctica. *GPS Solutions*, 4(1), 2-12.

Kumar, V., Venkataraman, G. & Rao, Y.S. (2009). SAR Interferometry and speckle tracking approach for glacier velocity estimation using ERS-1/2 and TERRASAR-X spotlight high resolution data. *IEEE International Symposium on Geoscience and Remote Sensing IGARSS*, 3757-3760.

Kwok, R. & Fahnestock, M.A. (1996). Ice sheet motion and topography from radar interferometry. *IEEE Transactions on Geoscience and Remote Sensing*, 34(1), 189-200.

Leprince, S., Barbot, S., Ayoub, F. & Avouac, J.P. (2007). Automatic and Precise Ortho-rectification, Coregistration, and Subpixel Correlation of Satellite Images, Application to Ground Deformation Measurements. *IEEE Transactions on Geoscience and Remote Sensing*, 45(6), 1529-1558.

Leprince, S., Berthier, E., Ayoub, F., Delacourt, C., & Avouac, J. (2008). Monitoring earth surface dynamics with optical imagery. *EOS Transactions*, 89(1), 1-2.

Levesque, R. (2007). SPSS programming and data management: A guide for SPSS and SAS users, fourth edition. SPSS Inc., Chicago III.

Liu, H. (1999). Development of an Antarctic digital elevation model by integrating cartographic and remotely sensed data: A geographic information system based approach. *Journal of Geophysical Research*, 104(B10), 23199-23213.

Liu, H., Wang, L. & Jezek, K.C. (2006). Spatiotemporal variations of snowmelt in Antarctica derived from satellite scanning multichannel microwave radiometer and Special Sensor Microwave Imager data (1978-2004). *Journal of Geophysical Research*, 111(F1).

Liu, H., Zhao, Z. & Jezek, K.C. (2007). Synergistic fusion of interferometric and speckle-tracking methods for deriving surface velocity from interferometric SAR data. *IEEE Geoscience and Remote Sensing Letters*, 4(1), 102-106.

Liu, H., Wang, L., Tang, S. & Jezek, K.C. (2012). Robust multi-scale image matching for deriving ice surface velocity field from sequential satellite images. *International Journal of Remote Sensing*, 33(6), 1799-1822.

Lucchitta, B.K., Rosanova, C.E. & Mullins, K.F. (1995). Velocities of Pine Island glacier, West Antarctica, from ERS-A SAR images. *Annual of Glaciology*, 21, 277-283.

Luckman, A., Murray, T., Jiskoot, H., Pritchard, H. & Strozzi, T. (2003). ERS SAR feature-tracking measurements of outlet glacier velocities on a regional scale in East Greenland. *Journal of Glaciology*, 36, 129-134.

Lythe, M.B., Vaughan, D.G. & the BEDMAP Consortium. (2001). BEDMAP: A new ice thickness and subglacial topographic model of Antarctica. *Journal of Geophysical Research*, 106(86), 11335-11351.

Massom, R. (2003). Recent iceberg calving events in the Ninnis Glacier region, East Antarctica. *Antarctic Science*, 15(2), 303-313.

Maxwell, S.K., Schmidt, G.L. & Storey, J.C. (2007). A multi-scale segmentation approach to filling gaps in Landsat ETM+ SLC-off images. *International Journal of Remote Sensing*, 28(23), 5339-5356.

Meier, M.F. (1993). Ice, climate and sea level: Do we know what is happening? *Ice in the Climate System*, 141-160.

Mohr, J.J. & Reeh, N. (2002). Glacier surface velocity measurements from radar interferometry and the principle of mass conservation. *Proceedings of IGARSS 2002, June 2-28, Toronto*.

Monaghan, A., Bromwich, D., Fogt, R., Wang, S., Mayewski, P., Dixon, D., Ekaykin, A., Frezzotti, M., Goodwin, I., Isaksson, E., Kaspari, S., Morgan, V., Oerter,

H., Ommen, T., Van der Veen, C. & Wen, J. (2006). Insignificant change in Antarctic snowfall since the International Geophysical Year. *Science*, 313(5788), 827-831.

Morgan, V.I. & Budd, W.F. (1975). Radio-echo sounding of the Lambert Glacier Basin. *Journal of Glaciology*, 15(73), 103-111.

Nguyen, A.T. & Herring, T.A. (2005). Analysis of ICESat data using Kalman filter and kriging to study height changes in East Antarctica. *Geophysical Research Letters*, 32, 1-4.

Nuth, C., Schuler, T.V., Kohler, J., Altena, B. & Hagen, J.O. (2012). Estimating the long-term calving flux of Kronebreen, Svalbard, from geodetic elevation changes and mass-balance modeling. *Journal of Glaciology*, 58(207), 119-133.

Paterson, W.S.B. (1994). The physics of glaciers (3rd edn.). Butterworth-Heinemann, Oxford, UK, 480pp.

Payne, A.J. & Bamber, J.L. (2004). Mass balance of the cryosphere. Observations and Modelling of Contemporary and Future Changes. Cambridge, New York, Melbourne: Cambridge University Press, pp. 644.

Philips, H.A. (1999). Applications of ERS satellite radar altimetry in the Lambert Glacier-Amery Ice Shelf system, East Antarctica. (PhD. Thesis, University of Tasmania).

Price, S.F., Conway, H., Waddington, E.D. & Bindshadler, R.A. (2008). Model investigations of inland migration of fast-flowing outlet glaciers and ice streams. *Journal of Glaciology*, 54(184), 49-60.

Pritchard, H.D., Arthern, R.J., Vaughan, D.G. & Edwards, L.A. (2009). Extensive dynamic thinning on the margins of the Greenland and Antarctic ice sheets. *Nature*, 461(7266), 971-975.

Rack, W., Rott, H., Siegel, A. & Skvarca, P. (1999). The motion field of northern Larsen Ice Shelf, Antarctic Peninsula, derived from satellite imagery. *Annual of Glaciology*, 29, 261-266.

Rees, W.G. (2012). Assessment of ASTER global digital elevation model data for Arctic research. *Polar Record*, 48(244), 31-39.

Remy, J., Becquevort, S., Haskell, T. & Tison, J. (2008). Impact of the B-15 iceberg “stranding event” on the physical and biological properties of sea ice in McMurdo Sound, Ross Sea, Antarctica. *Antarctic Science*, 20(6), 593-604.

Rignot, E. (2002). Mass balance of East Antarctic glaciers and ice shelves from satellite data. *Annals of Glaciology*, 34, 217-227.

Rignot, E., Bamber, J.L., Van Den Broeke, M.R., Davis, C., Li, Y., Jan Van De Berg, W. & Meijgaard, E. (2008). Recent Antarctic ice mass loss from radar interferometry and regional climate modeling. *Nature Geoscience*, 1(2), 106-110.

Rignot, E., Casassa, G., Gogineni, P., Krabill, W., Rivera, A. & Thomas, R. (2004). Accelerated ice discharge from the Antarctic Peninsula following the collapse of Larsen B ice shelf. *Geophysical Research Letters*, 31(18), 1-4.

Rignot, E. & Jacobs, S.S. (2002). Rapid bottom melting widespread near Antarctic ice sheet grounding lines. *Science*, 296, 2020-2023.

Rignot, E. & Kanagaratnam, P. (2006). Changes in the velocity structure of the Greenland Ice Sheet. *Science*, 311(5763), 986-990.

Rignot, E., Mouginot, J. & Scheuchl, B. (2011a). Antarctic grounding line mapping from differential satellite radar interferometry. *Geophysical Research Letters*, 38, L10504.

Rignot, E., Mouginot, J. & Scheuchl, B. (2011b). Ice flow of the Antarctic ice sheet. *Science*, 333(6048), 1427-1430.

Rignot, E., Mouginot, J. & Scheuchl, B. (2011c). MEaSUREs Antarctic Grounding Line from Differential Satellite Radar Interferometry, [list dates of data used]. Boulder, Colorado USA: NASA EOSDIS DAAC at NSIDC. <http://nsidc.org/data/nsidc-0498.htm>.

Rignot, E., Rivera, A. & Casassa, G. (2003). Contribution of the Patagonia Icefields of South America to sea level rise. *Science*, 302, 434-437.

Rignot, E. & Thomas, R.H. (2002). Mass balance of polar ice sheets. *Science*, 297(5586), 1502-1506.

Robertson, B. (1992). Mass balance of the Amery Ice Shelf front. Hon. Thesis. University of Tasmania. Institute of Antarctic and Southern Ocean Studies.

Rosen, P.A., Hensley, S., Joughin, I.R., Li, F.K., Madsen, S.N., Rodriguez, E., & Goldstein, R.M. (2000). Synthetic aperture radar interferometry. *Proceedings of the IEEE*, 88(3), 333-382.

Scambos, T.A. & Bindshadler, R. (1993). Complex ice-stream flow revealed by sequential satellite imagery. *Annals of Glaciology*, 17, 177-182.

Scambos, T.A., Bohlander, J., Raup, B. & Haran, T. (2004). Glaciological characteristics of Institute Ice Stream using remote sensing. *Antarctic Science*, 16(2), 205-213.

Scambos, T.A., Dutkiewicz, M.J., Wilson, J.C. & Bindshadler, R.A. (1992). Application of image cross-correlation to the measurement of glacier velocity using satellite image data. *Remote Sensing of Environment*, 42(3), 177-186.

Scambos, T.A., Hulbe, C., Fahnestock, M. & Bohlander, J. (2000). The link between climate warming and break-up of ice shelves in the Antarctic Peninsula. *Journal of Glaciology*, 46(154), 516-530.

Schlosser, E., Lipzig, N.V. & Oerter, H. (2002). Temporal variability of accumulation at Neumayer station, Antarctica, from stake array measurements and a regional atmospheric model. *Journal of Glaciology*, 48(160), 87-94.

Shepherd, A. & Wingham, D. (2007). Recent sea-level contributions of the Antarctic and Greenland Ice Sheets. *Science*, 315(5818), 1529-1532.

Shepherd, A., Wingham, D. & Rignot, E. (2004). Warm ocean is eroding West Antarctic Ice Sheet. *Geophysical Research Letters*, 31(23), L23404.

Short, N.H. & Gray, A.L. (2005). Glacier dynamics in the Canadian High Arctic from Radarsat-1 speckle tracking. *Canadian Journal of Remote Sensing*, 31(3), 225-239.

Skvarca, P., Rapp, B. & De Angelis, H. (2003). Recent behaviour of Glaciar Upsala, a fast-flowing calving glacier in Lago Argentino, southern Patagonia. *Annual of Glaciology*, 36(1), 184-188.

Solomon, S. and 7 others, eds. (2007). Climate change 2007: the physical science basis. *Contribution of Working Group I to the Fourth Assessment Report of the Intergovernmental Panel on Climate Change*. Cambridge, etc., Cambridge University Press.

Strozzi, T., Luckman, A., Murray, T., Wegmuller, U. & Werner, C. (2002). Glacier motion estimation using SAR offset-tracking procedures. *IEEE Transactions on Geosciences and Remote Sensing*, 40(11), 2384-2391.

Swithinbank, C.W.M. (1988). Satellite Image Atlas of the World: Antarctica. USGS Professional Paper, 1386-B.

Tang, S. (2007). Investigation of coastal dynamics of the Antarctic ice sheet using sequential Radarsat SAR images. (MS thesis, Texas A&M University)

Testut, L., Hurd, r., Coleman, R., Remy, F. & Legresy, B. (2003). Comparison between computed balance velocities and GPS measurements in the Lambert Glacier basin, East Antarctica. *Annals of Glaciology*, 37, 337-343.

Thomas, R.H. (1979). Ice shelves: A review. *Journal of Glaciology*, 24(90), 273-286.

Thomas, R.H. and 17 others. (2004). Accelerated sea-level rise from West Antarctica. *Science*, 306(5694), 255-258.

Thomas, R., Frederick, E., Krabill, W., Manizade, S. & Martin, C. (2009). Recent changes on Greenland outlet glaciers. *Journal of Glaciology*, 55(189), 147-162.

Van de Wal, R.S.W. (2004). Greenland: Modeling. In: J.L.Bamer and A.J.Payne(eds.), *Mass Balance of the Cryosphere*. Cambridge University Press, Cambridge, UK, pp. 437-458.

Vaughan, D.G., Bamber, J.L., Giovinetto, M., Russell, J. & Cooper, A.P. (1999). Reassessment of net surface mass balance in Antarctica. *Journal of Climate*, 12, 933-946.

Walker, R.T., Dupont, T.K., Parizek, B.R. & Alley, R.B. (2008). Effects of basal-melting distribution on the retreat of ice-shelf grounding lines. *Geophysical Research Letters*, 35(17), 1-5.

Wen, J., Wang, Wang, Y., W., Jezek, K.C., Liu, H. & Allison, I. (2010). Basal melting and freezing under the Amery Ice Shelf, East Antarctica. *Journal of Glaciology*, 56(195), 81-90.

Wen, J., Wang, Y., Liu, J., Jezek, K.C., Huybrechts, P., Csatho, B.M., Farness, K.L. & Sun, Bo. (2008). Mass budget of the grounded ice in the Lambert Glacier-Amery Ice Shelf system. *Annals of Glaciology*, 48, 193-197.

Wen, J., Jezek, K.C., Csatho, B., Herzfeld, U.C., Farness, K.L. & Huybrechts, P. (2007). Mass budgets of the Lambert, Mellor and Fisher Glaciers and basal fluxes beneath their flowbands on Amery Ice Shelf. *Science China Earth Sciences*, 50(11), 1693-1706.

Werner, C., Wegmuller, U., Strozzi, T. & Wiesmann, A. (2005). Precision estimation of local offsets between pairs of SAR SLCs and detected SAR images. *IEEE*

International Symposium on Geoscience and Remote Sensing (IGARSS), 1-12, 4803-4805.

Wingham, D.J., Ridout, A.J., Scharroo, R., Arthern, R.J. & Shum, C.K. (1998). Antarctic elevation change from 1992 to 1996. *Science*, 282(5388), 456-458.

Wong, A.P.S., Bindoff, N.L. & Forbes, A. (1998). Ocean–ice shelf interaction and possible bottom water formation in Prydz Bay, Antarctica. Ocean, ice, and atmosphere: interactions at the Antarctic continental margin, Washington, DC, American Geophysical Union, 173-187.

Wu, X. & Jezek, K. (2004). Antarctic ice-sheet balance velocities from merged point and vector data. *Journal of Glaciology*, 50(169), 219-230.

Young, N.W. & Hyland, G. (2002). Velocity and strain rates derived from InSAR analysis over the Amery Ice Shelf, East Antarctica. *Annals of Glaciology*, 34, 228-234.

Yu, J. (2005). Investigation of glacial dynamics in Lambert Glacial Basin using satellite remote sensing techniques. (PhD dissertation, Texas A&M University).

Yu, J., Liu, H., Jezek, K.C., Warner, R.C. & Wen, J. (2010). Analysis of velocity field, mass balance, and basal melt of the Lambert Glacier-Amery Ice Shelf system by incorporating Radarsat SAR interferometry and ICESat laser altimetry measurements. *Journal of Geophysical Research*, 115, 1-16.

Zebker, H. & Villasenor, J. (1992). Decorrelation in interferometric radar echoes. *IEEE Transactions on Geoscience and Remote Sensing*, 30(5), 950-959.

Zhang, S., E, D. & Wang, Z. (2006). Ice velocities on the front of Amery Ice Shelf, East Antarctica, from static GPS observations. *Geoinformatics 2006: GNSS and Integrated Geospatial Applications*, 6418, Q4180.

Zhang, X. & Andersen, O.B. (2006). Surface ice flow velocity and tide retrieval of the Amery Ice Shelf using precise point positioning. *Journal of Geodesy*, 80, 171-176.

Zwally, H.J., Abdalati, W., Herring, T., Larson, K., Saba, J. & Steffen, K. (2002a). Surface melt-induced acceleration of Greenland ice-sheet flow. *Science*, 297(5579), 218-222.

Zwally, H.J., Beckley, M.A., Brenner, A.C. & Giovinetto, M.B. (2002b). Motion of major ice-shelf fronts in Antarctica from slant-range analysis of radar altimeter data, 1978-98. *Annals of Glaciology*, 34, 255-262.

Zwally, H.J., Giovinetto, M.B., Li, J., Cornejo, H.G., Beckley, M.A., Brenner, A.C. & Yi, D. (2005). Mass changes of the Greenland and Antarctic ice sheets and shelves and contributions to sea-level rise: 1992-2002. *Journal of Glaciology*, 51(175), 509-527.